Theses and Dissertations

Theses, Dissertations, and Senior Projects

January 2018

3-D Stress Redistribution During Hydraulic Fracturing Stimulation And Its Interaction With Natural Fractures In Shale Reservoirs

Jun Ge

Follow this and additional works at: https://commons.und.edu/theses

Recommended Citation

Ge, Jun, "3-D Stress Redistribution During Hydraulic Fracturing Stimulation And Its Interaction With Natural Fractures In Shale Reservoirs" (2018). *Theses and Dissertations*. 2218.
https://commons.und.edu/theses/2218

3-D STRESS REDISTRIBUTION DURING HYDRAULIC FRACTURING
STIMULATION AND ITS INTERACTION WITH NATURAL FRACTURES IN
SHALE RESERVOIRS

by

Jun Ge

Bachelor of Science, China University of Geosciences (Wuhan), 2000
Master of Science, Peking University, 2003
Master of Science, Texas A&M University, 2009

A Dissertation

Submitted to the Graduate Faculty

of the

University of North Dakota

In partial fulfillment of the requirements

for the degree of

Doctor of Philosophy

Grand Forks, North Dakota
May
2018

II

This dissertation, submitted by Jun Ge in partial fulfillment of the requirements for the Degree of Doctor of Philosophy from the University of North Dakota, has been read by the Faculty Advisory Committee under whom the work has been done and is hereby approved.

_____
Sukhvarsh Jerath,   Chairperson   Date

_____
Ahmad Ghassemi   Date

_____
Kegang Ling   Date

_____
Dongmei Wang   Date

_____
Yun Ji   Date

This dissertation is being submitted by the appointed advisory committee as having met all of the requirements of the School of Graduate Studies at the University of North Dakota and is hereby approved.

_____
Dr. Grant McGimpsey,
Dean of the School of Graduate Studies

_____
Date

III

PERMISSION

Title	3-D Stress Redistribution during Hydraulic Fracturing Stimulation and Its Interaction with Natural Fractures in Shale Reservoirs
Department	Civil Engineering
Degree	Doctor of Philosophy

In presenting this dissertation in partial fulfillment of the requirements for a graduate degree from the University of North Dakota, I agree that the library of this University shall make it freely available for inspection. I further agree that permission for extensive copying for scholarly purposes may be granted by the professor who supervised my dissertation work or, in his absence, by the Chairperson of the department or the dean of the Graduate School. It is understood that any copying or publication or other use of this dissertation or part thereof for financial gain shall not be allowed without my written permission. It is also understood that due recognition shall be given to me and to the University of North Dakota in any scholarly use which may be made of any material in my dissertation.

Jun Ge

May 1, 2018

TABLE OF CONTENTS

APPENDICES

LIST OF FIGURES

LIST OF TABLES

ACKNOWLEDGMENTS

It has been a long and tough time for me to finish this dissertation in the past several years at University of North Dakota (UND), especially with my success in my full-time job at Energy & Environmental Research Center. During these years, I have received tons of helps from my advisors, committees, and colleagues in the process of pursuing my Ph.D. degree. I want to acknowledge them for their generosity and kindness.

Firstly, I would like to express my deep and sincere gratitude to my advisor, Dr. Sukhvarsh Jerath for his continuous support of my Ph.D. study. His patience, guidance, and encouragement throughout the completion of this research and thesis. Dr. Jerath is the most kind and knowledgeable professor I have ever met. He can always point out the most important problems in my research work and has saved lots of time for my study. Without his help, I cannot imagine my completion of my Ph.D. Study.

I also would like to say thanks to my co-advisor, Dr. Ghassemi, who has introduced me into the field of Rock Mechanics and provided me with the opportunity to learn and research on Petroleum related geomechanics, as well as the technologies hydraulic fracture from him. I specially thank him for his patiently and carefully review on the manuscript of this thesis.

Besides my advisors, I would like to thank the rest of the members of my committee: Dr. Kegang Ling, Dr. Dongmei Wang, and Dr. Yun Ji for their insightful comments and

ABSTRACT

The hydraulic fracturing (also called fracturing, or fracking) technique has been widely applied in many fields, such as the enhanced geothermal systems (EGS), the improvement of injection rates for geologic sequestration of CO_2, and for the stimulations of oil and gas reservoirs, especially for unconventional reservoirs with extremely low permeability. The key point for the success of hydraulic fracturing operations in unconventional resources is to connect and reactivate natural fractures and create the effective fracture network for fluid flow from pores into the production wells. To understand hydraulic fracturing technology, we must to understand some other affecting factors, e.g. in-situ stress conditions, reservoir mechanical properties, natural fracture distribution, and redistribution of the stress regime around the hydraulic fracture. Therefore, an accurate estimation of the redistribution of pore pressure and stresses around the hydraulic fracture is necessary, and it is very important to find out the reactivations of pre-existing natural fractures during the hydraulic fracturing process.

Generally, fracture extension as well as its surround pore pressure and stress regime are affected by: poro- and thermoelastic phenomena as well as by fracture opening under the combined action of applied pressure and in-situ stresses. In this thesis, the previous studies on the hydraulic fracturing modeling and simulations were reviewed; a comprehensive semi-analytical model was constructed to estimate the pore pressure and stress distribution around an injection induced fracture from a single well in an infinite reservoir. With Mohr-

Coulomb failure criterion, the natural fracture reactivation potential around the hydraulic fracture were studied. Then, a few case studies were presented, especially with the application in unconventional natural fractured shale reservoirs.

This work is of interest in interpretation of micro-seismicity in hydraulic fracturing and in assessing permeability variation around a stimulation zone, as well as in estimation of the fracture spacing during hydraulic fracturing operations. In addition, the results from this study can be very helpful for selection of stimulated wells and further design of the re-fracturing operations.

CHAPTER I

INTRODUCTION

1.1. Motivations

Hydraulic fracturing is a widely used in recent decades as the most efficient stimulation technique to initiate a high permeability conduit of fluid in a low permeability reservoir. During the hydraulic fracturing operation, a fluid is injected into a well at a pressure high enough to fracture the reservoir formation. The process also can also cause opening up of natural fractures already present in the formation to improve the productivity of the reservoir, as illustrated in the Fig.1.1.
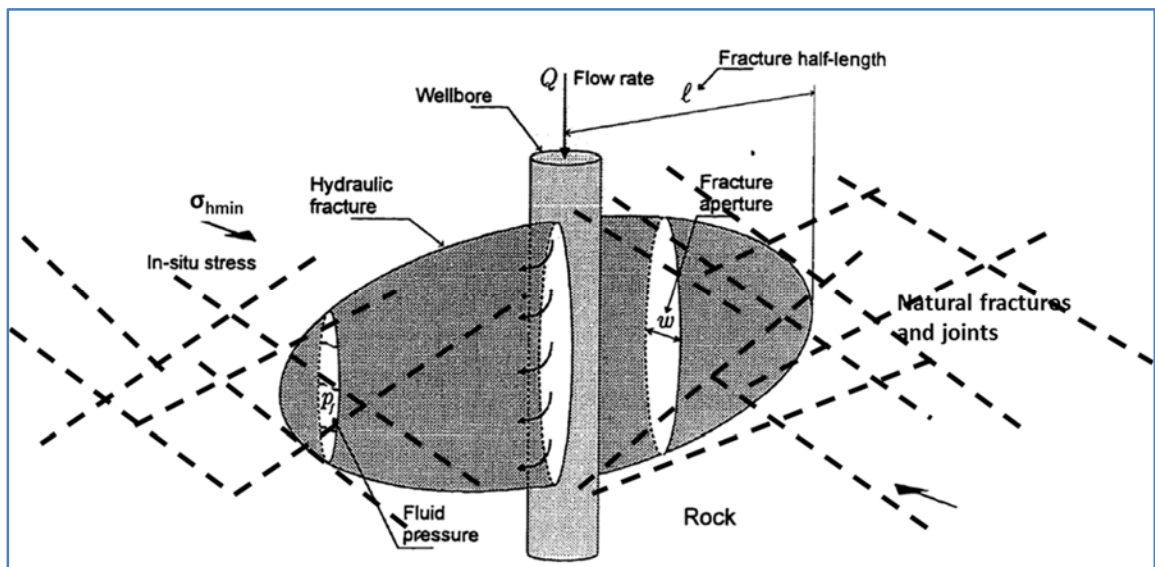
Fig.1.1 Illustration of Hydraulic Fracturing (modified from Carbonell, 1996).

It is just like the highway between cities and states, interacting with as many as possible county roads, connecting little towns and rural areas, and providing the most convenient

efficient way for the traffic (Natzke, et al., 2012). Hydraulic fractures are interacting and reactivating with natural fractures to form the fracture system as illustrated in an ideal fracture system as shown in Fig. 1.2. In fact, at the real reservoir environment, the hydraulic fracture could be very complicated by the natural joint system as shown in Fig. 1.3. Hydraulic fracturing is also connecting with pore spaces filled with energy fluid and providing the higher effective permeability for the low permeable matrix, so that the reservoir fluids can flow to the producing wells.
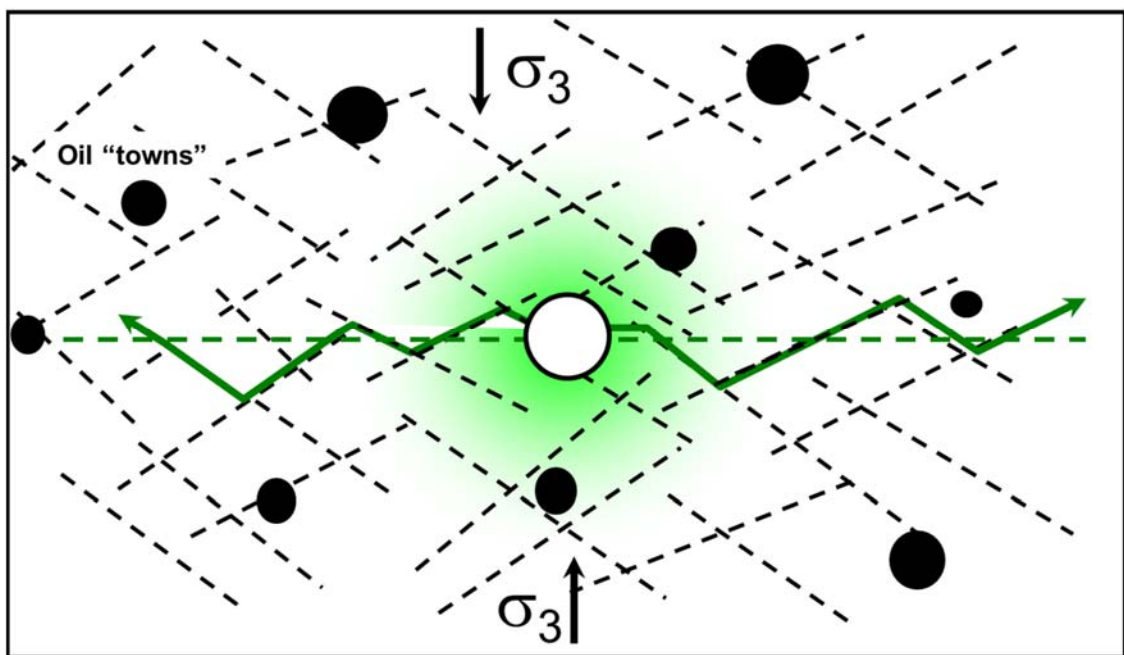
Fig. 1.2 Ideal Fracture "Highway" System.

For the past over 70 years since the first hydraulic fracturing treatment was done in 1947 in Hugoton field (Gidley, 1989), the technique of hydraulic fracturing has been widely used in energy industry. Nowadays, hydraulic fracturing has become one of the most important technique in the stimulation of hydrocarbon wells for increasing oil and gas recovery (e.g.,

Veatch et al., 1983a, 1983b; Yew, 1997; Economides and Nolte, 2000). More than 70% of

the gas wells and 50% of the oil wells in North America are stimulated using hydraulic

fracturing (e.g., Valko and Economides 1995). Moreover, hydraulic fracturing can also be

applied in the in-situ stress measurement (e.g., Haimson, 1978; Shin et al., 2001), and

geothermal reservoir stimulations (e.g., Murphy, 1983; Legarth, Huenges, and

Zimmermann 2005; Nygren and Ghassemi 2005).
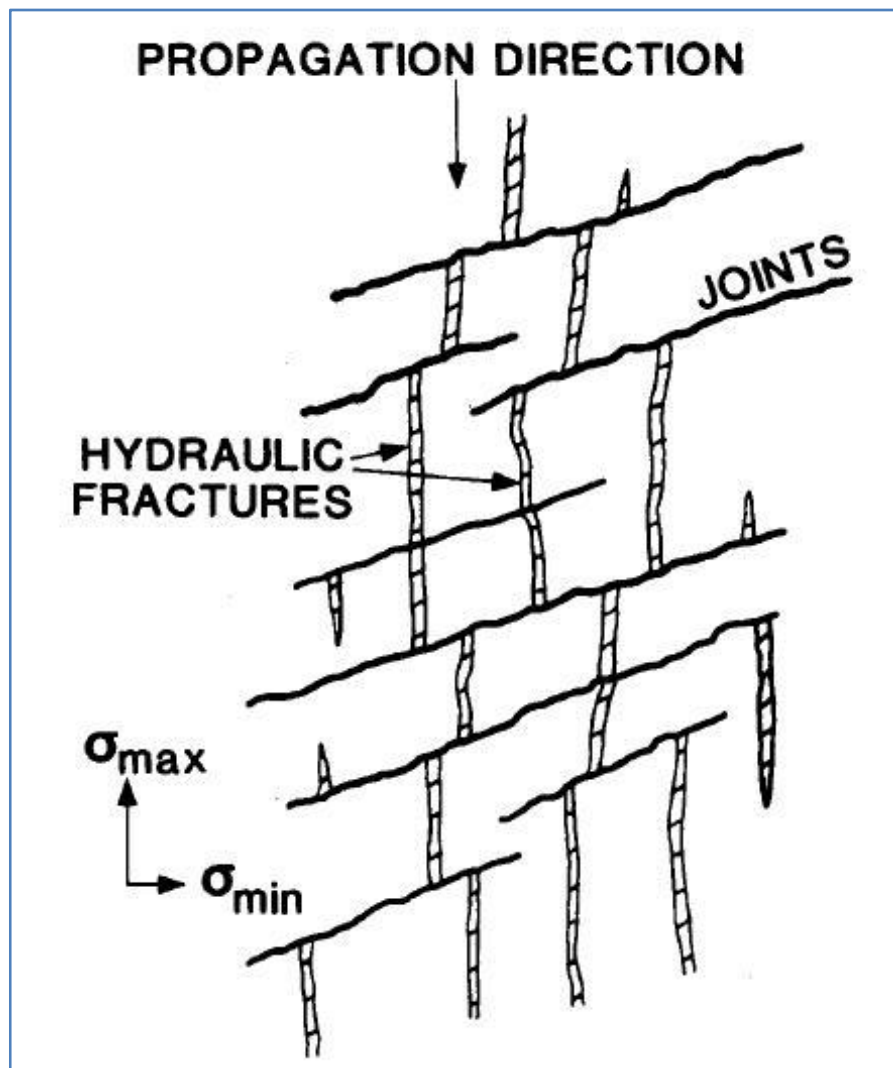
Fig.1.3 Geometry of Fracture Network (Modified from Warpinski, 1987).

In the unconventional resources, including tight gas sandstones (TG), gas shale (GS), coal-bed methane (CBM), and oil shale, the hydraulic fracture itself cannot increase too much of the production by the limitation of its size. Fortunately, all most all oil and gas reservoirs are natural fractured. The fracture network system, after stimulated by the hydraulic fracturing operations, can give orders of magnitude increase in effective permeability in the reservoirs.

Therefore, the key point for the success of hydraulic fracturing operations in unconventional resources is to connect and reactivate natural fractures and create the effective fracture network for fluid flow from the tight pores into the production wells. However, to efficiently hydraulic fracturing the well and reactivate as much as possible the natural fractures is not an easy operation. This requires the understanding of the in-situ stress conditions, the reservoir mechanical properties, the natural fracture distributions, and the redistribution of the stress regime around the hydraulically induced fracture. Therefore, an accurate estimation of the redistribution of pore pressure and stresses around the hydraulic fracture is necessary, and it is very important to find out the reactivations of pre-existing natural fractures during the hydraulic fracturing process.

The fracture extension as well as pore pressure and stress regime around the fracture are affected by: poroelastic and thermoelastic phenomena, as well as by fracture opening under the combined action of applied pressure and in-situ stresses. A couple of numerical studies and analytical methods have been completed for the potential of natural fracture

reactivations which resulted from pressurization of the hydraulic fracture analyzation. However, most analytical methods could not consider all the details of the reservoir conditions, while the advanced numerical methods are too complex for practical field application. Therefore, the objective of this study is to provide a model more accurate than the simple analytical models and relatively easier-to-use than the numerical software for field application.

1.2. Literature Review

There are thousands of publications each year talking about the mechanics and designs of hydraulic fracturing. Lots of numerical methods or analytical models are proposed on every aspect of the hydraulic fracturing process, from the fracture initiation, propagation, to the closure, and to the re-fracturing. The interactions between hydraulic fractures and the natural fractures are also discussed by many researchers in either conferences or journal articles especially in recent years since the shale boom in Unites States. In this thesis, some of the previous studies will be reviewed, especially those researches on the poroelastic and thermoelastic effects, stress shadow from fracture compression, and the interactions between hydraulic fracture with the natural fractures in unconventional reservoirs.

Geertsma (1966) firstly considered the potential of poroelastic effects on influencing the hydraulically driven fracture propagation. Oil bearing rock is a two-phase system which are affected by the poroelastic effects. However, Geertsma concluded that these effects

5

were to be insignificant in practical situations. A couple years later, Cleary (1980) suggested that poroelastic effects could be expressed as "back-stress". At the same year, Settari studied poroelastic effects through a similar approximation (Settari, 1980).

A poroelastic Perkins-Kern-Nordgren (PKN) fracture model based on an explicit moving mesh algorithm was studied by Detournay (Detournay, et al. 1990). The poroelastic effects, induced by leak-off of the fracturing fluid, were treated in a manner consistent with the basic assumptions of the PKN model. Their model was formulated in a moving coordinates system and solved using an explicit finite difference technique.

Perkins and Gonzalez (1985) presented a semi-analytical model of a waterflooding induced fracture emanating from a single well in an infinite reservoir. Their model has two important features. First, the leak-off distribution is two-dimensional with the pressure transient moving elliptically outward into the reservoir with respect to the growing fracture. Second, their model incorporated the effect of thermoelastic, which can change the reservoir rock stresses and therefore has influence on the fracture propagation pressure. It was shown that cooling of the reservoir rock by the injection of cold water may cause the elongation of fractures.

Koning (1985) presented an analytical model for waterflood-induced fracture growth under the influence of poroelastic and thermoelastic changes in reservoir stress. In his work, a model was presented in which the leak-off distribution in the reservoir is allowed to eolve

from 1-D perpendicular to fracture surface to 2-D radial with respect to the fracture. A three dimensional calculation of poroelastic changes in reservoir stress at the fracture face is performed analytically for a quasi-steady state pressure profile including elliptical discontinuities in fluid mobility.

The effect of fracture pressurization on the stress redistribution was studied using the solution for calculating the stresses distribution around a flat elliptic crack (Jaeger and Cook, 1979). In addition, Pollards (1987) also provided the solution for the calculation of the stress changes around an elliptic fracture by including the effect of fracture pressurization.

In recent years, Gahssemi and his peers (Ghassemi, et al, 1996, 2005, 2006, 2010, 2011, 2012, 2016, 2017) have published a series of researches on the numerical modeling and simulations of the poroealstic and/or thermoelastic effects on hydraulic fracturing process. Those work even coupled with other effects and investigated the rock failure mechanisms during hydraulic fracturing and interactions with natural fractures.

A lot of work have been done on reactivations of the natural fractures (including faults, natural fractures, etc.) in rock formations. Jaeger and Cook (1979) gave the Mohr-Coulomb failure criterion for rock joints and calculated the shear stress and the normal stress on a joint surface using the principal stresses. Furthermore, Mildren et al. (2002) and Nelson et al. (2007) introduced the structural permeability diagram technique to estimate the

additional treating effective pressure required to reactivate the existing natural fractures in rock formations.

Palmer et al. (2007) used a method to estimate the failed reservoir volume and enhanced permeability after stimulation by hydraulic fracturing operations and gave a case study on the Barnett Shale. As pointed out by Palmer et al, (2007) greater gas flow rate is correlated with a larger "failed reservoir volume" and a higher net fracturing pressure. They investigated the shear slip or failure along planes of weakness by pore pressure increases during injection of fracturing fluid. By combing the knowledge of in-situ stress, and the properties of the planes of weakness (either joints, faults, or natural fractures), they calculated the failed distance from the central fracture plane. By matching the failed reservoir volume with the volume of the microseismic cloud, they estimated the enhanced permeability by stimulation after injection.

Ge and Ghassemi (2007, 2008, 2011, 2012, 2014) have done some studies in recent years on the analytical and semi-analytical methods to analyze the poroelastic, thermoelastic, and fracture compression effects on the pore pressure and stress redistributions around a hydraulic fracture, as well as their interactions with the natural fractures in the unconventional reservoirs. In their work, the pore pressure and stress redistributions were studied both in 2-D and 3-D models, which were illustrated with some case studies and by comparing with previous research work.

Of course, there are lots of other research work on this topic. We will talk about them in the following chapters and sections when cited in this thesis.

1.3. Research Objectives

The objectives of this study are:

- Investigate the pore pressure variations around a hydraulic fracture during the fracture propagation and waterflooding processes. Research the shear slip or failure along planes of weakness by pore pressure increases during injection of fracturing fluid.

- Study the poroelasic and thermoelastic effects on fracture propagation, as well as on the pore pressure and stress redistributions around an injection induced hydraulic fracture.

- Research on the induced stress variations by fracture compression.

- Estimate the stimulated reservoir volume (SRV) and the enhanced permeability by the natural fractures reactivations by stresses redistribution from hydraulic fracturing operations.

1.4. Sign Convention

The sign convention is important for this work. As we know, in different research field the sign convention is different. For example, most accepted sign convention in the field of

civil engineering considers tensile stress as positive. However, in the field of petroleum, compressive stress is often considered as positive for the convenience of underground engineering use. In this thesis, in order to be consistent with most of the rock mechanics literature, all equations are presented using the compression positive convention. This sign convention is adopted for the remainder of this thesis unless otherwise specified. In additional, the unit system used in examples and case studies is varied based on each specific case with different available data.

1.5. Dissertation Outline

This dissertation consists of total eight chapters.

Chapter I is the introduction, including the motivations, literature review and objectives of this work, and the sign convention, as well as the organization of this dissertation.

Chapter II gives an overview of the hydraulic fracturing history, reviews the mechanics of hydraulic fracturing, describes the hydraulic fracturing process and the traditional analytical models, and summarizes the recent developments on both analytical and numerical models, as well as the poroelasticity and thermoelasticity. It also talks about the applications of hydraulic fracturing, focusing on the application in the naturally fractured shale reservoirs.

Chapter III presents the model establishment of this study, describes the methodology and

governing equations, and explains the pore pressure distribution around a hydraulic fracture.

Chapter IV describes the induced stresses by the poroelastic and thermoelastic effects as well as by fracture compression around a hydraulic fracture.

Chapter V discusses the failure criteria, especially the Mohr-Coulomb failure criterion used for the reactivation of natural fractures. It also describes the construction of the structural permeability diagram. In addition, the calculations of failure potentials and stimulated reservoir volume are presented.

Chapter VI verifies the model with the examples from shale reservoirs, including the case study on Barnett Shale and one case on the Bakken Shale.

Chapter VII presents the conclusions and discusses some of the future research directions in this field.

In the end, the Appendices include the deduction of the 3-D induced stresses by fracture compression, the slip map of natural fractures in a given stress regime, the 2-D induced by poroelasticity, thermoelasticity and fracture compression, the fracture propagation dimensions, and case study on the stimulated reservoir volume and enhanced permeability by hydraulic fracturing.

CHAPTER II

HYDARULIC FRACTURING OVERVIEW

2.1. Hydraulic Fracturing History

Since the first treatment in 1947, hydraulic fracturing has become a widely used and the

most effective stimulation technique to stimulate the productivity of oil and gas wells

(Gidley,1989). The process of a hydraulic fracturing operation is shown in Fig.2.1 (Veatch

1983). It consists of blending special fluid/chemicals to make the appropriate fracturing

fluid and then pumping the blended fluid into the pay zone at high enough rates and

pressures to wedge and extend a fracture hydraulically (Gidley, 1989).
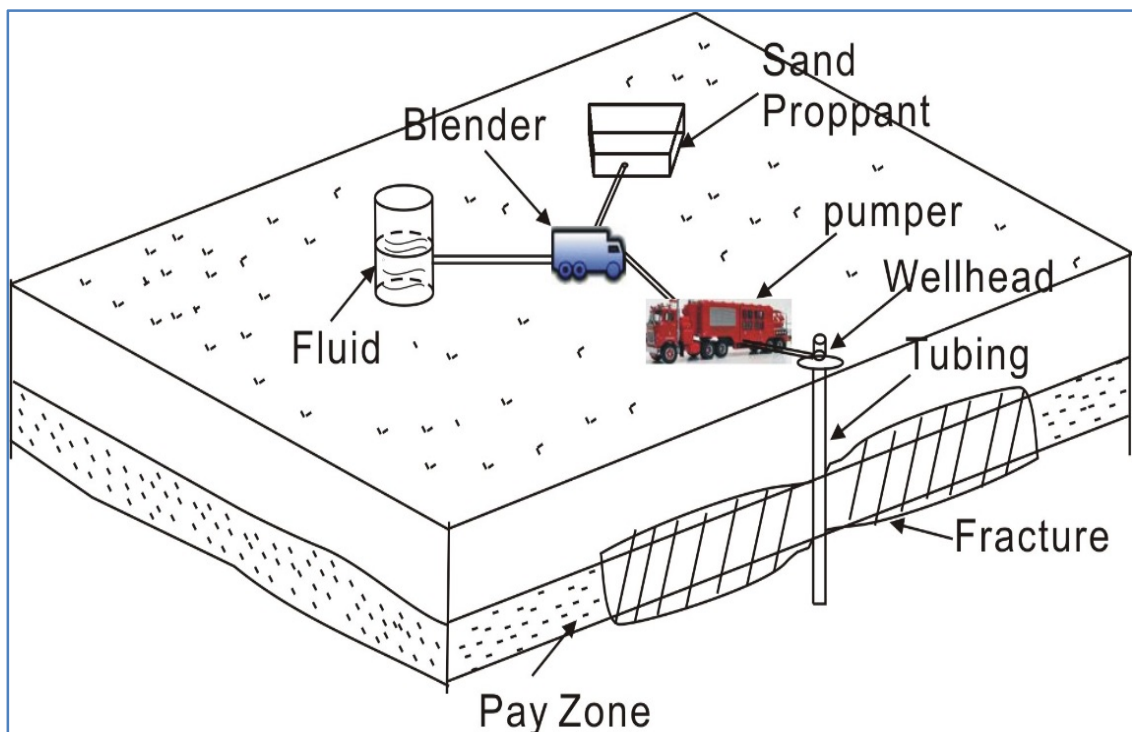
Fig.2.1 Hydraulic Fracturing Process (Modified from Veatch 1983).

Currently, the horizontal drilling and multiple stages hydraulic fracturing make it happen the boom of the shale oil and gas in United States (Fig. 2.2).
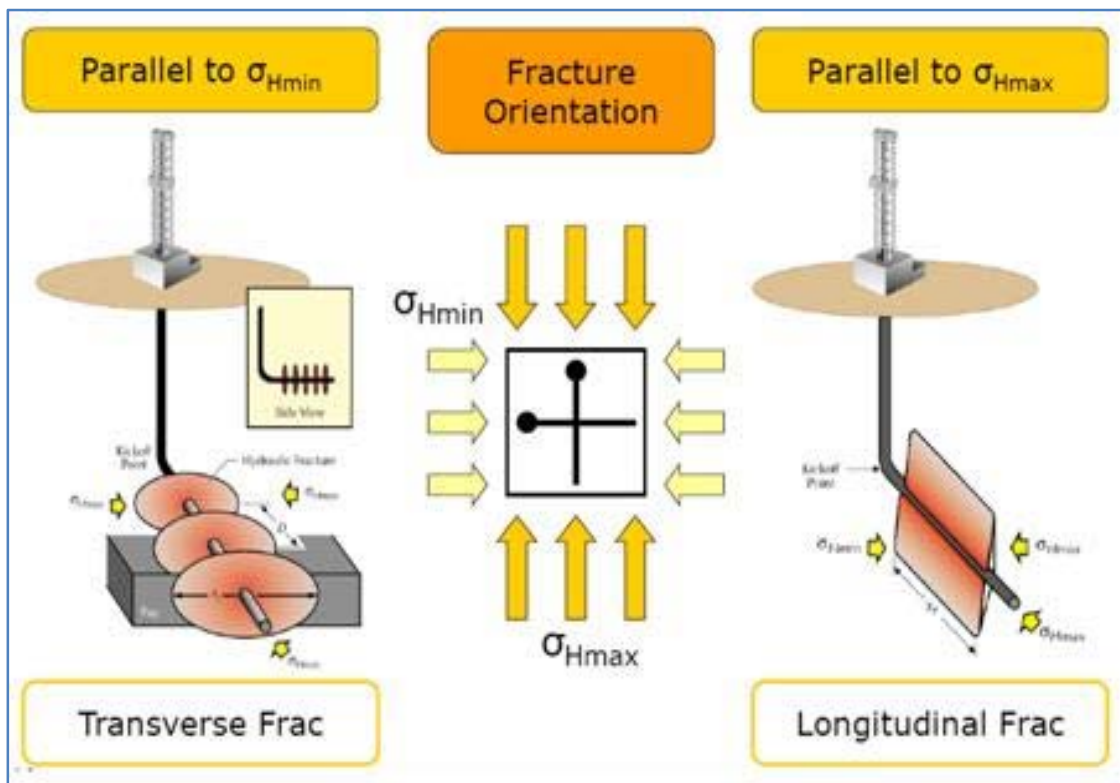
Fig.2.2 Fracture Orientation in Horizontal Wells (Francesco, 2009).

Another application of hydraulic fracturing is to stimulate geothermal production. The production of geothermal energy from dry and low permeability reservoirs is achieved by water circulation in natural and/or man-made fractures, and is often referred to as enhanced or engineered geothermal systems (EGS) (Fig. 2.3, Ghassemi, 2012).
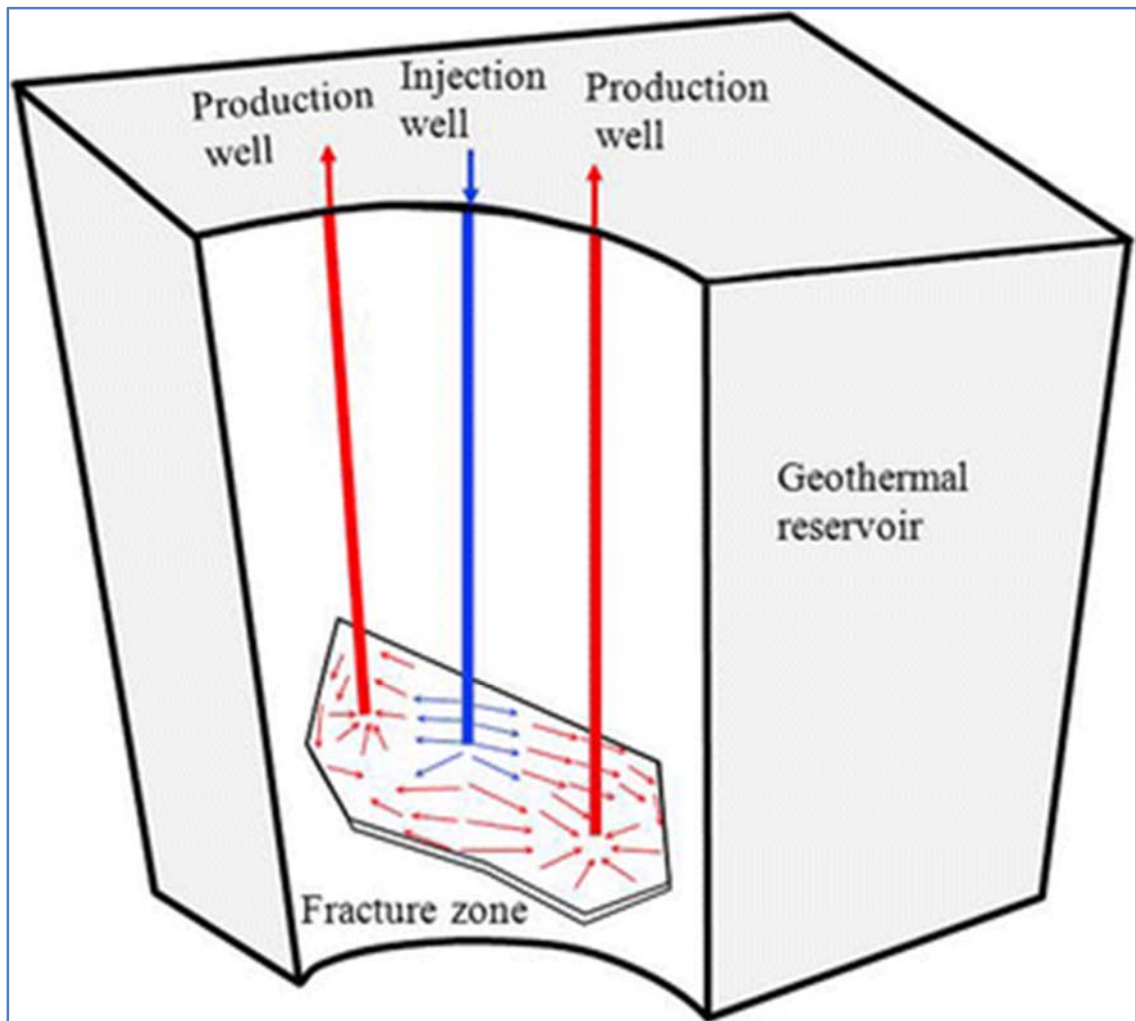
Fig. 2.3 An illustration of Engineered or Enhanced Geothermal System (Ghassemi, 2012).

There are still some other applications of hydraulic fracturing, including the stress measurement, such as step rate tests, minifracing test, leakoff test, and extended leakoff test etc. (Soliman, et al., 1990; Kunze, et al., 1991; Detournay, et al, 1997). Fig. 2.4 shows a typical pressure profile during the minifracing tests.
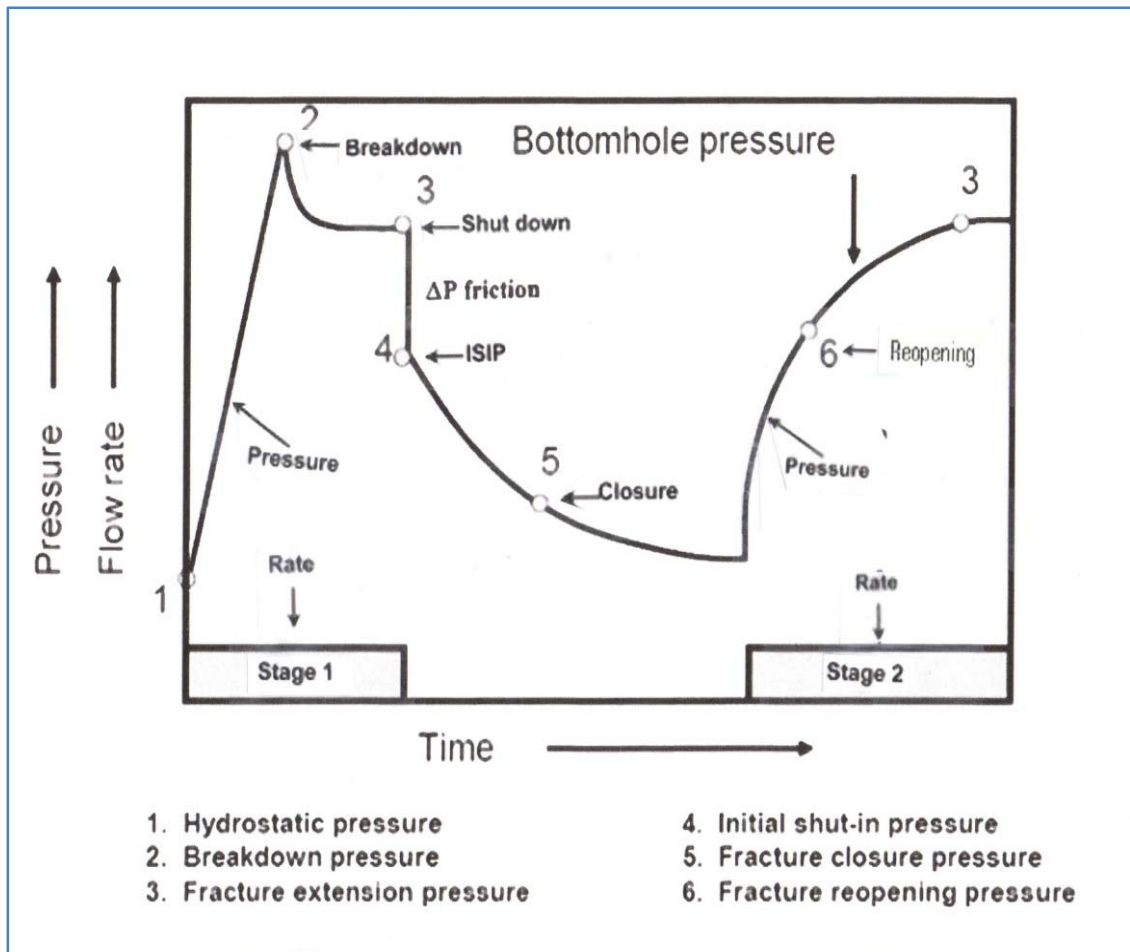
Fig. 2.4 Minifrac Test Pressure Curve (Modified from Gidley, 1989).

In hydraulic fracturing operations, the fracture fluid which is injected into the well can be oil-based, water-based, or acid-based (Veatch et al., 1983a, 1983b). However, water based hydraulic fracturing are the most common used and the least expensive. Slick-water fracturing combines water with a friction-reducing chemical additive which allows the water to be pumped at higher injection rates into the formation (Palisch, 2008). Nowadays, there are many researches on the different fracturing fluids and proppants. These technologies are not covered here and will not be discussed in details in this work.

15

2.2   Fracture Mechanics

During the process of hydraulic fracturing process, rock mechanics plays an important role by controlling the geometry of propagating fractures (Gidley, 1989). It is important to understand the mechanisms of fluid-rock interaction in the hydraulic fracturing. In real field work, fractures are more complicated in geometry and can have complex fractures (Fig.1.3). In the complex fracture network, the long axis or "fairway" is referred as the hydraulic fracture fairway length while the short axis is referred to as fairway width (Fisher, et al. 2004). The volume of this fracture system or the stimulated volume can be estimated using the modeling and simulation methods for the hydraulic fractures. To do this, it is critical to know the pore pressure and stress distribution around the hydraulic fracture or stimulated fairway which varies with the geometry of hydraulic fractures, and is affected by mechanical, thermal, and chemical conditions of the surrounding host rock, especially the mechanical properties (Ge, 2009).

Based on the previous studies (Gidley, 1989), the fracture propagation and geometry can be affected by some important factors, including:

- In-situ stresses existing in the rock formation: the local stress fields and variations in stresses are often thought to be the most important factor to dominate fracture orientation and fracture growth. At the common condition, a hydraulic fracture will propagate in the direction of the maximum principal stress.

16

- Relative pay zone thickness of formation controls the growth of the fracture in its height.

- Mechanical rock properties such as elastic modulus, Poisson's ratio, and rock toughness will affect the fracture initiation and propagation.

- Fluid treating pressure in the fracture.

- The original reservoir pore pressure in the formation.

2.3 Traditional 2-D Hydraulic Fracturing Models

Over the past 60 years, many analytical and numerical models have been proposed to study fracture propagation. Those models include both two-dimensional (Perkins and Kern 1961; Geertsma and Klerk 1969; Nordgren 1972; Daneshy 1973) and three-dimensional models (Clifton in Gidley, 1989). In this work, the traditional 2-D models of hydraulic fracturing process are reviewed.

2.3.1 PKN Model

Perkins and Kern (1961) started the famous PKN model, in which equations were developed to compute fracture length and width for a fracture with fixed height. Later Nordgren (1972) improved this model by considering the leakoff effects to the solution. The PKN model assumes that the hydraulic fracture has a constant height and an elliptical cross section (Fig.2.5) both in the horizontal plane and in the vertical plane.

Based on solid mechanics, the fracture half height, H_f, is independent of the hydraulic fracture propagating distance away from the operating well. With the fixed height assumption, the hydraulic fracturing problem is reduced to 2-D by using the plane strain assumption. In the PKN model, the plane strain is assumed in the vertical direction, and the rock deformation in each vertical plane along the its propagation direction is assumed to be independent of other neighboring vertical planes. Plane strain condition implies that the elastic deformations to open or close, or shear the hydraulic fracture are fully concentrated in the vertical planes perpendicular to the direction of hydraulic fracture propagation.
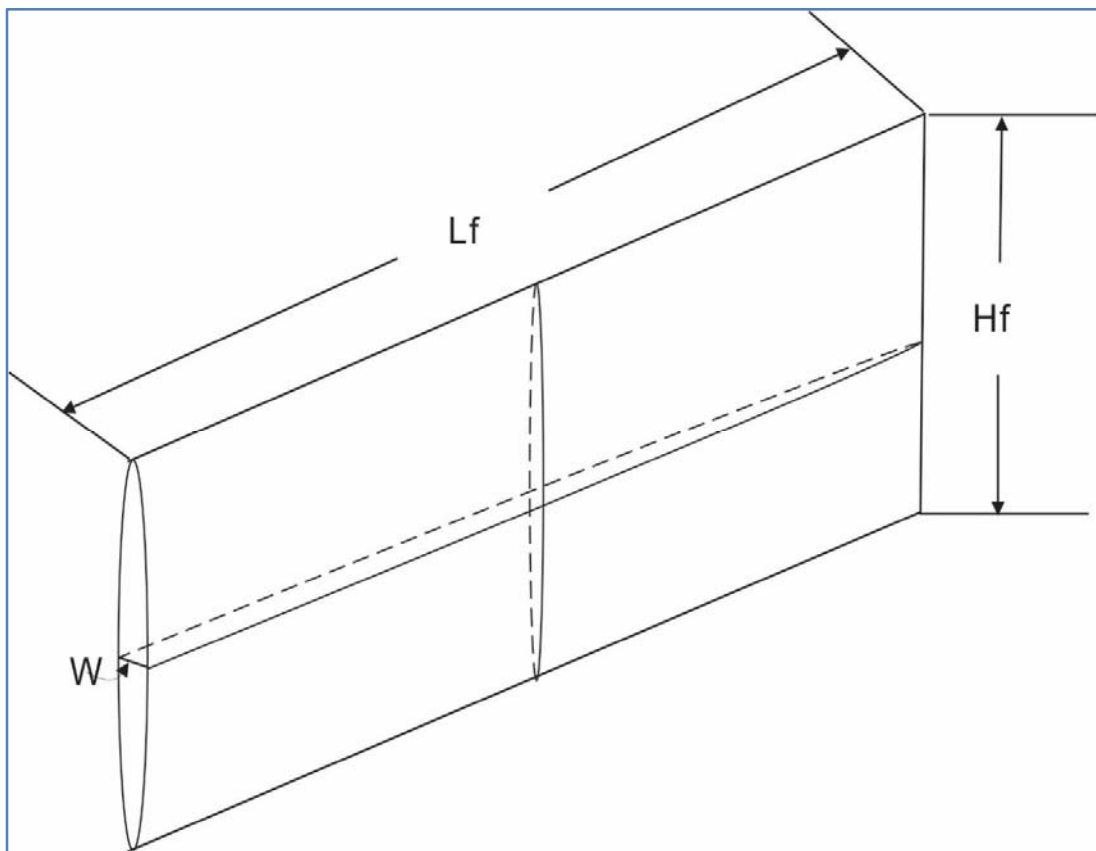
Fig.2.5 Geometry of PKN Model (Modified from Perkins and Kern, 1961).

The fluid flow problem in the PKN model is one-dimensional in an elliptical channel. The fluid fracturing pressure is assumed constant in any of the vertical cross sections perpendicular to the direction of fracture propagation.

2.3.2 KGD Model

The KGD model was first introduced by Khristianovic and Zheltov in 1955, and then improved by Geertsma and de Klerk in 1969. In this model, the fracture deformation and propagation are also assumed to be in a situation of plane strain. The model considers that the fluid flow in the fracture and the fracture propagation are one-dimension. The geometry of a traditional KGD hydraulic fracture propagation model is illustrated in Fig.2.6.
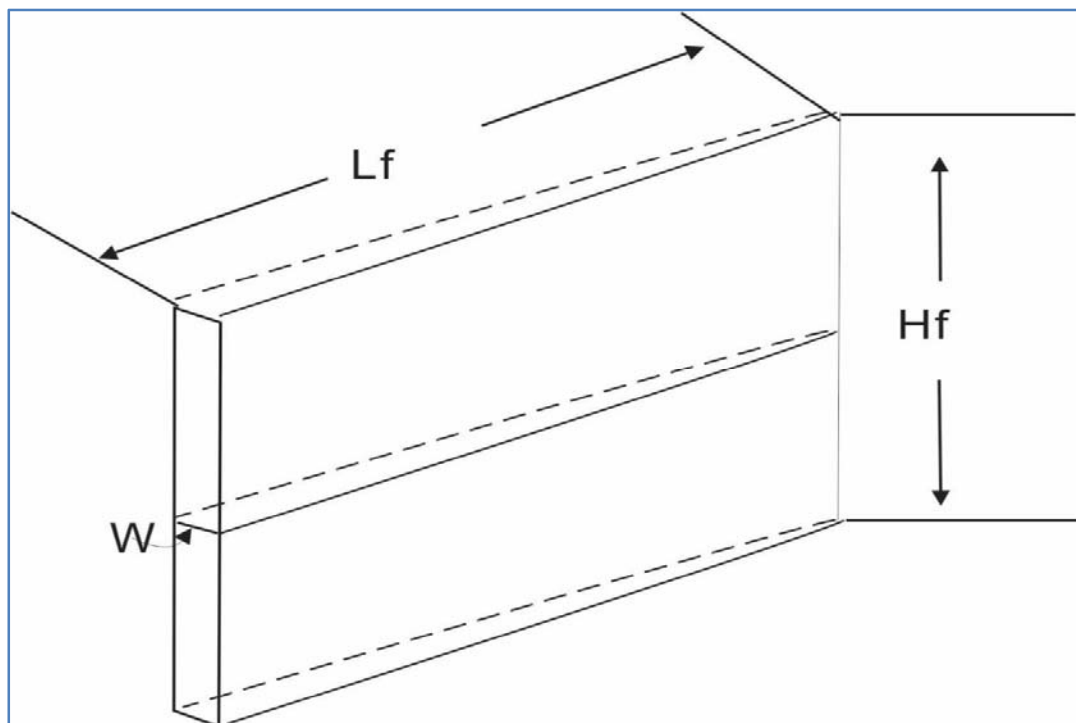
Fig.2.6 Geometry of KGD Model (Modified from Geertsma and de Klerk 1969).

There are several main assumptions in the KGD model:

- The fracture assumes elliptical cross sections in the horizontal plane;

- Each horizontal plane deforms independently;

- Fracturing fluid pressure in the propagation direction is controlled by the flow resistance;

- The rectangular cross section in the vertical plane;

- The fluid does not affect in the entire fracture length;

- The cross section in the vertical plane is rectangular.

2.3.3 Penny-Shape or Radial Model

The radial model assumes that the fracture is propagating within a given plane and the geometry of the hydraulic fracture is symmetrical with respect to the central point of the well at which the fluid is injected. The study of this fracture model in a dry rock mass can be found in Abé et al. (1976). They assumed a uniform distribution of fluid treating pressure and constant fluid injection rate in the well. Sneddon (1946) solved the problem for uniform pressure on the crack surface. In addition, Green and Sneddon (1950) solved the widely used elliptical penny shaped crack in an infinite solid with uniform applied pressure at the crack surface.

The main difference among the traditional 2-D hydraulic fracturing models, including PKN, KGD, and the Radial Model, are compared as shown in Table.2.1 (Ge, 2009).
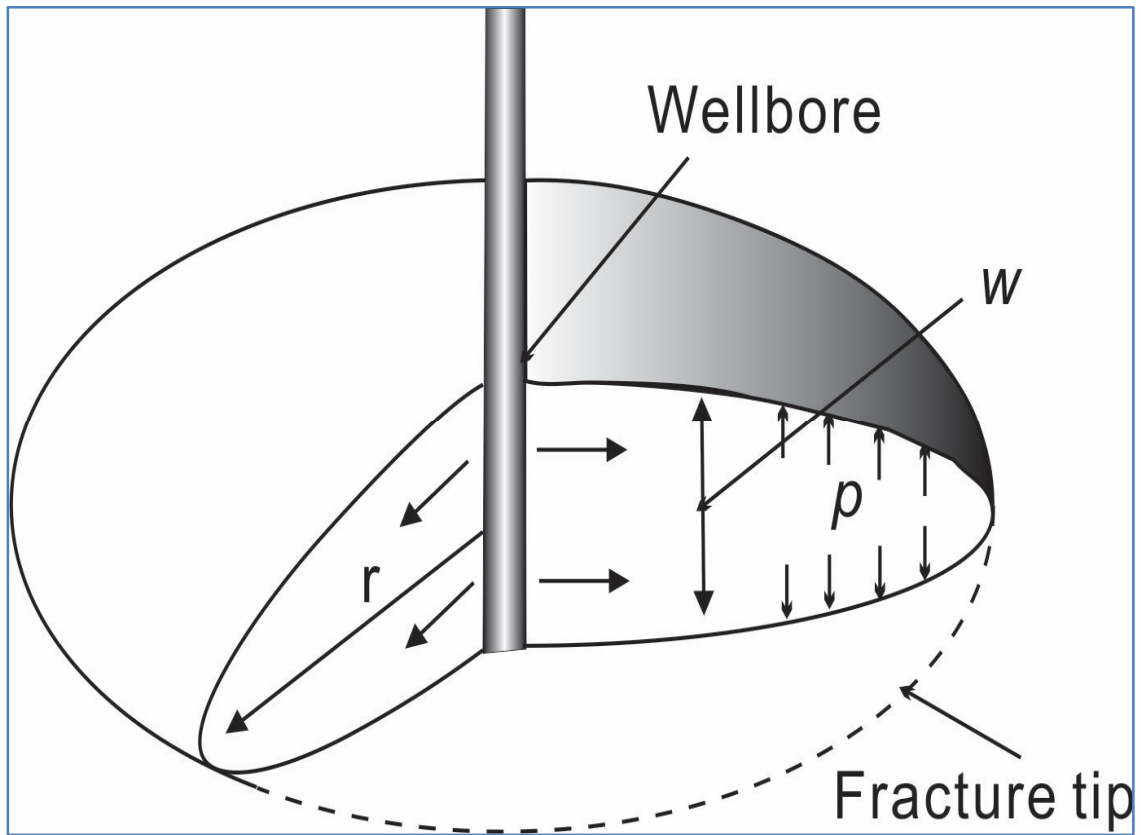
Fig.2.7 Geometry of Penny-Shape or Radial Model (Modified from Abé et al., 1976).

Table 2.1 Comparisons among 2-D Models

Model	Assumptions	Shape	Bottom Hole Pressure	Application
PKN	Fixed Height Plain Strain	Elliptical Cross Section	Increasing with Time	Length»Height
KGD	Fixed Height Plain Strain	Rectangle Cross Section	Decreasing with Time	Length<=Height
Radial	Uniform Distribution of Fluid Pressure	Circular Cross Section	Decreasing with Time	More Appropriate When It is Radial

2.4 Poroelasticity and Thermoelasticity

In the proposed models of this study in next chapters, the effects of pressure and temperature changes on the pore pressure and stress redistributions around a hydraulic fracture will be discussed. For geothermal reservoirs with high formation temperatures, these effects from poroelasticity and thermoelasticity are both significant, while for oil and gas reservoirs, the temperature difference between the reservoir formation and the injected fluid is not too high and the effects of thermoelasticity are insignificant (with few exceptions on some deep reservoirs with high formation temperature). In the following of this section, the basic theories of poroelasticity and thermoelasticity are discussed.

Fluid loss into the permeable formation can cause the pore pressure increase in the reservoir during the propagation of a hydraulic fracture. The increase of pore pressure will cause dilation of the formation rock around the hydraulic fracture, and then in turn reduce the width of the fracture. On the contrary, the rock deformation will also cause pore pressure increase. This process was firstly introduced by Biot in 1941 as the theory of poroelasticity. Rice and Cleary (1976) further improve the theory through using material parameters with physical interpretations.

Vandemme et.al, 1989 summarized the poroelastic effect as: a volumetric expansion of the porous formation rock is induced by an increase of the reservoir pore pressure, and then if the fluid is prevented from escaping (undrained condition), an increase of the pore pressure

results from the application of a confining pressure.

Timoshenko (1951) pointed out that if the geometry of a body structure is large compared to the scale at which inhomogeneities are apparent, the theory of poroelasticity can be a reasonable approximation. Therefore, it assumes the body to be large relative to a representative element of volume. It also assumes that the rock is composed of a porous, elastic, and solid skeleton that is saturated with fluids. Both the pore fluid and the solid grains in the skeleton can be assumed incompressible. Finally, Darcy's law is assumed for the fluid flow through the skeleton, so that the fluid flow rate is proportional to the gradient of the reservoir pore pressure.

Rice and Cleary (1976) stated that the pore pressure, p, can be defined as "the equilibrium pressure that must be exerted on a homogeneous reservoir of pore fluid brought into contact with a material element so as to prevent any exchange of fluid between it and the element". They also proposed that the term undrained deformation applies to "stress alterations, $\Delta\sigma_{ij}$, over a time scale that is too short to allow loss or gain of pore fluid in an element by diffusive transport to or from neighboring elements". Conversely, the term drained deformation applies to stress alterations, $\Delta\sigma_{ij}$, over a time scale that allow diffusive transport of pore fluid between elements to reach a steady state condition (Fig.2.8).
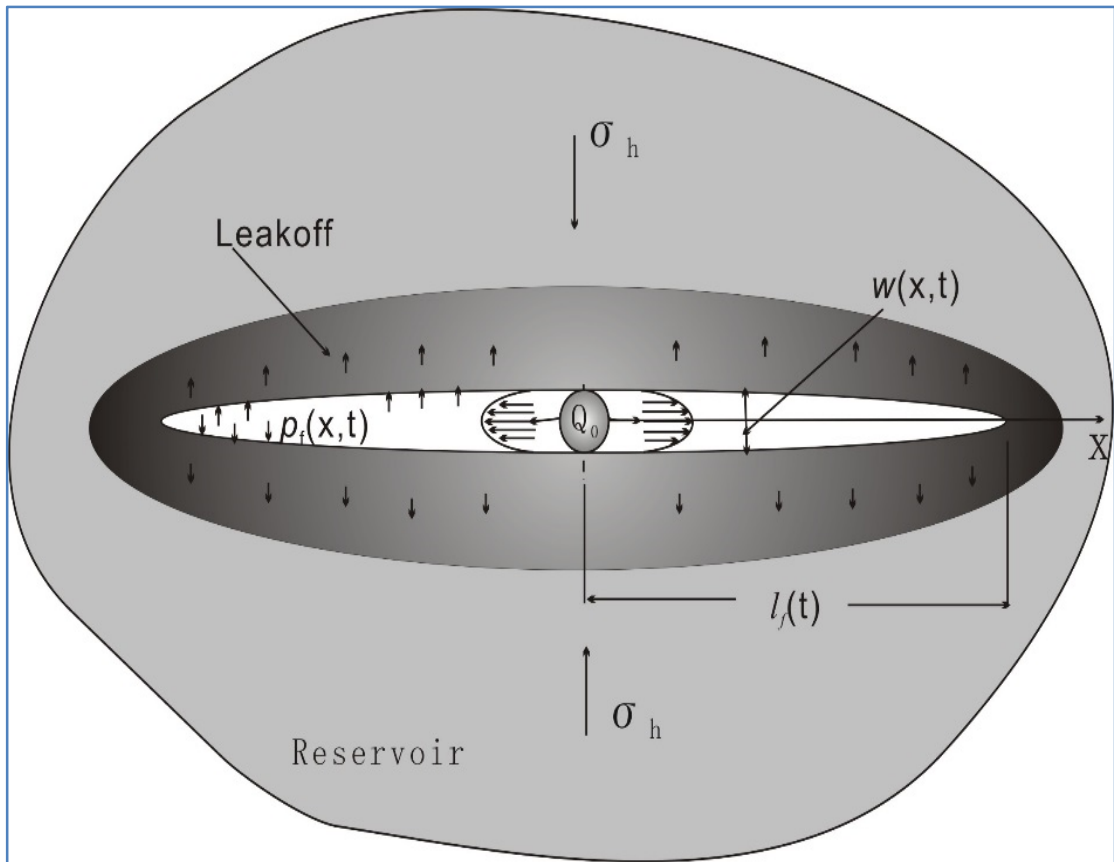
Fig.2.8 Mechanics of Poroelasicity (Modified from Rice and Cleary, 1976).

There are several parameters that are commonly used when studying with poroelastic materials. The first parameter is poroelastic constant, α, which is independent of the fluid properties and is defined as (Rice and Cleary, 1976):

$$\alpha = \frac{3(v_u - v)}{B(1 - 2v)(1 + v_u)} = 1 - \frac{K}{K_s} \tag{2.1}$$

In the above equation, the parameter B is Skempton pore pressure coefficient, v_u is defined by undrained Poisson ratio, v is drained Poisson ratio, K is bulk modulus of elasticity, and Ks bulk modulus of solid phase. The range of this poroelastic constant is 0 to 1, with most

24

rocks fall into the range of 0.5 to 1 (Rice and Cleary, 1976).

The other important parameter is the poroelastic stress coefficient, usually expressed with symbol η (the symbols used in this thesis are listed in the nomenclature, otherwise will be described in the context), and defined as (Detournay and Cheng, 1993):

$$\eta = \alpha \frac{(1-2\nu)}{2(1-\nu)} \tag{2.2}$$

The range of η is 0 to 0.5, and it is also independent of the fluid properties.

Similar with the poroelasticity, the theory of thermoelasticity describes the effect of temperature changes on the stresses variations and displacements in a reservoir rock (Jaeger, Cook and Zimmerman, 2007). The theory of thermoelasticity can be analogous to the theory of poroelasticity, with the temperature playing a role similar to that of the pore pressure (Ge, 2009).

In oil and gas industry, hydraulic fracturing by fluid injection is often used in both tight and permeable reservoirs. In tight reservoirs, fractures are usually induced intentionally to increase the fluid injectivity. In a permeable reservoir, hydraulic fracturing may occur unintentionally when cold water is injected into a relatively hot reservoir. During waterflooding, the secondary or tertiary oil recovery processes, injected fluids are usually at temperatures cooler (70 - 80 ºF) than the original in-situ reservoir temperatures (200 ± ºF). A region of cooled rocks forms around an injection well, and the area of this region

grows as additional fluids are injected. The rock within the cooled region contracts and this could result in a decrease in stress concentration around the injection well until the injection pressure minus the hoop stress exceeds the tensile strength of the rock at a critical point on the well boundary and a fracture begins to propagate to orient itself in the direction of maximum in-situ stress. Although the increase in injectivity is favorable, the fracture may or may not have an adverse effect on the sweep efficiency of the water drive in the case of petroleum, or inefficient heat extraction in geothermal reservoirs, depending on the length, height and orientation of the fracture. These fracture parameters can also be of critical importance for a successful application of a tertiary recovery process, and development of geothermal reservoirs (Ge, 2009).

A coupled model with thermo-poroelasticity was first introducd by Palciauskas and Domenico (1982), and later it was studied by Zhang (2004). Chun (2013) talked more details about the linear theories of poroelasticity and thermoelasticity. In a fluid-saturated porous rock formation, temperature change can significantly affect the surrounding stress field, as well as the pore pressure field. Thermal loading causes rock volumetric deformation by the thermal expansion/contraction of both the fluid and the rock solid. If the reservoir rock is heated, expansion of the reservoir and injected fluid can lead to a significant increase in pore pressure at the confined space. The tendency is reversed at the condition of cooling. Therefore, the time dependent poro-thermo-mechanical processes should be all considered in the transient temperature field.

2.5 Hydraulic Fracturing in Shale Reservoirs

In recent decades, the production of gas and oil from shale plays in United States has rapidly increased. The success of the US shale boom relies mostly on the applications of horizontal drilling and hydraulic fracturing. Fig. 2.9 shows the locations of the lower 48 states shale plays in US. Among those shale plays, Barnett shale gas and Bakken shale oil are typical fields for the applications of hydraulic fracturing techniques.
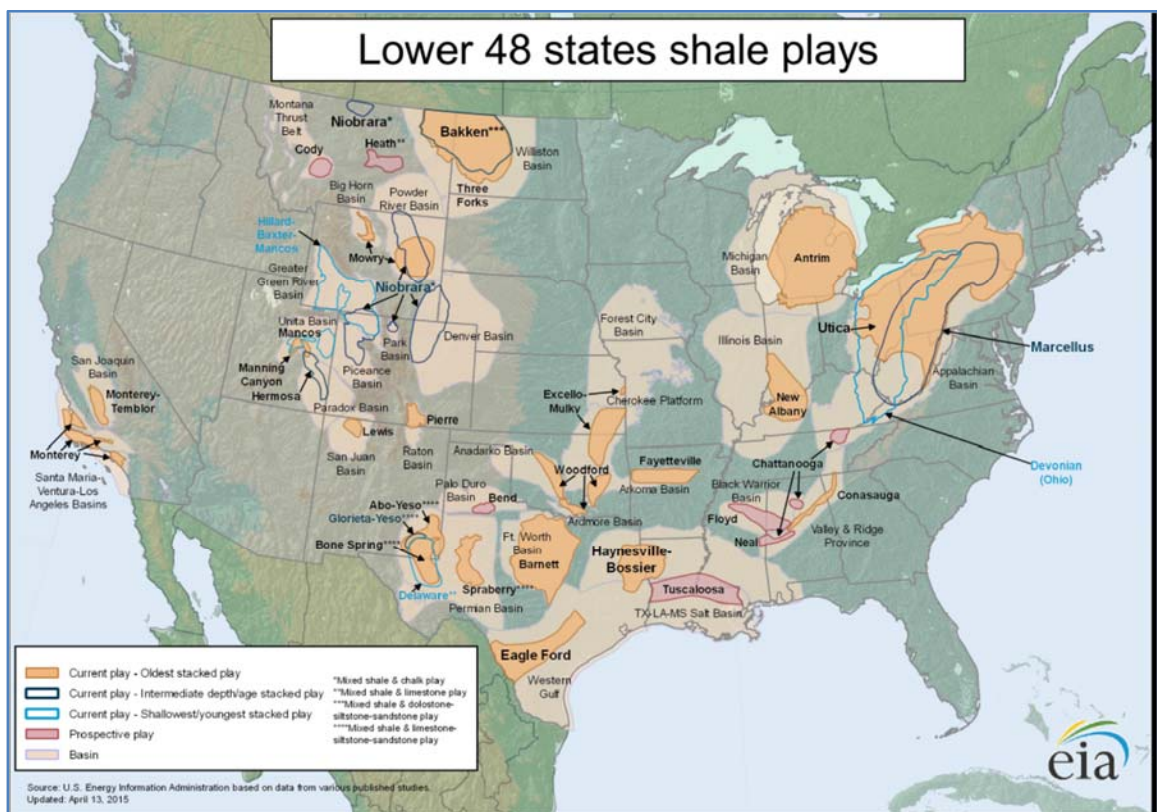
Fig. 2.9 Lower 48 States Shale Plays (EIA, 2015).

Gas shales, such as the Barnett, Marcellus, Fayettville, and Woodford, and oil shale play

Bakken, contain a relatively high total organic content (e.g., the Barnett has a total organic content of 4-5%) and are performing as the source rock as well as the reservoir. The gas and/or oil are stored in the limited pore space of these formation rocks. Matrix permeability of these shales are very difficult to measure because they are so low. Previous studies show that the permeability of shale is on the order of nanodarcies (Warpinskin, et al., 2008). Obviously, economic production cannot be achieved if the well stimulation operations are not operated in the field.

Fortunately, there are existing natural fractures in the shale reservoirs. In most papers, the use of the terms, such as joints, faults, natural fractures, fissure, etc., are very confusing. In this study, we use natural fractures (the most commonly used structure) to represent the main geologic heterogeneities in the unconventional reservoirs for simplification.

The development of a fracture "network" by horizontal drilling and hydraulic fracturing plays the key point for the economic production. As pointed by Cipolla et al. (2008), in many unconventional shale reservoirs fracture growth is complex. The interaction of the hydraulic fracture with natural fractures could be vital for the success of well stimulation. In their work, the fracture network could be ideally divided by different fracture complexity such as simple plannar fractures, complex plannar fractures, and network fracture behavior.

As shown in Fig.2.10, the growth of hydraulic fracture can be divided into four main ideal categories:

- Planar-coupled growth

- Planar-decoupled growth or fissure opening

- Complex growth, including non-communicating and communicating sub-categories

- Network growth
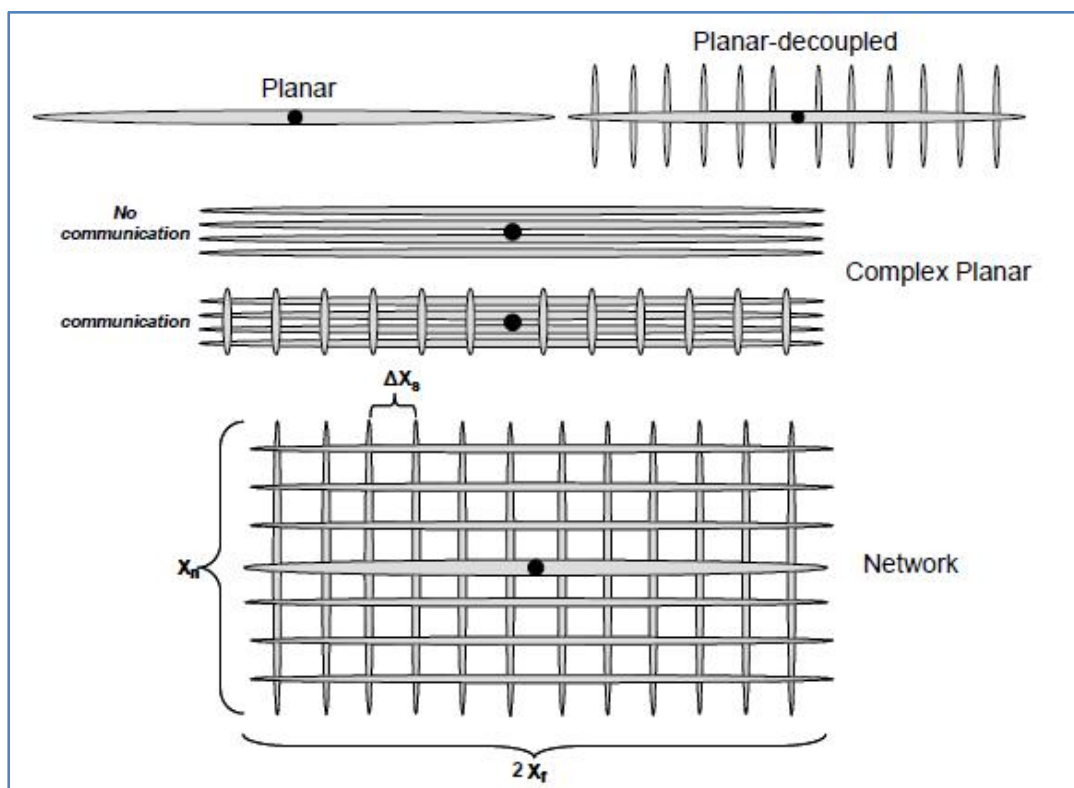
Fig.2.10 Fracture Growth and Complexity Scenarios (Cipolla et al., 2008).

The fracture network growth in Fig.2.10 is an ideal condition. In fact, the interaction between the hydraulic fracture and the natural fracture are much more complicated (as shown in Fig.2.11, Warpinski et al, 2008). There are many factors that can affect the reactivations of the natural fractures before they can really make contributions to the

fracture network. In this work, we mainly focused on the pore pressure and stress redistribution around a hydraulic fracture and the interactions with natural fractures in the shale reservoirs.
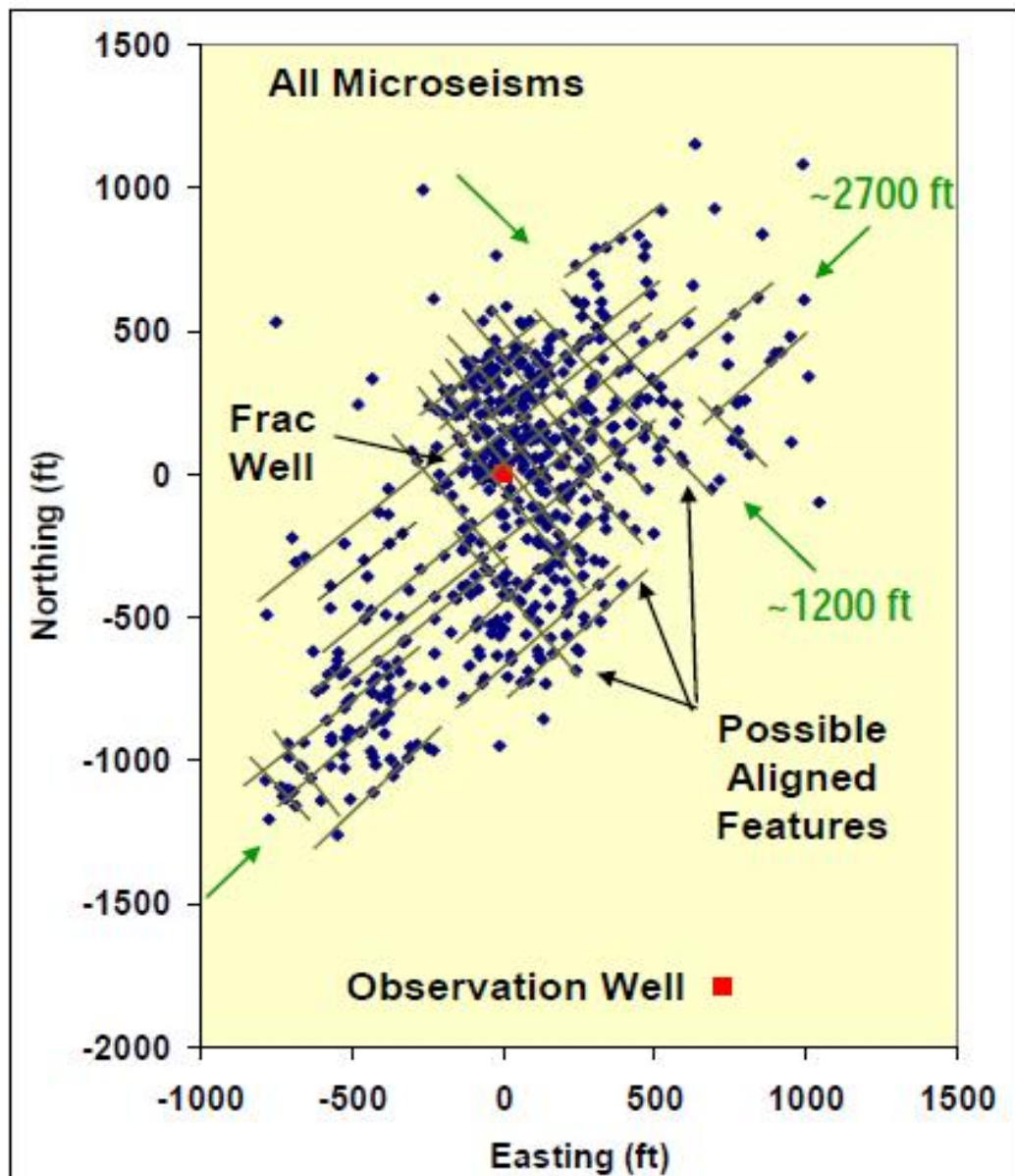
Fig.2.11 Microseismic Fracture Mapping Shows Complex Network Growth and The Potential Area Of Stimulated Reservoir Volume In Shale (Warpinski, et al, 2008).

CHAPTER III

HYDARULIC FRACTURING MODEL SETUP

3.1 Hydraulic Fracturing Propagation Model

In the field operations of oil and gas reservoirs, injection is at a bottomhole pressure (BHP) that is controlled high enough to initiate and extend a hydraulic fracture. The injected fluid then leaks off radially through the large fracture face area. Due to the decreasing in horizontal in-situ rock stresses that result from mostly cold fluid injection, hydraulic fracturing pressures can be lower than would be expected for an ordinary low leak-off hydraulic fracturing treatment. At this condition, the flow system will evolve from an essentially circular geometry in the plan view to one characterized more nearly as elliptical as shown in Fig.3.1.
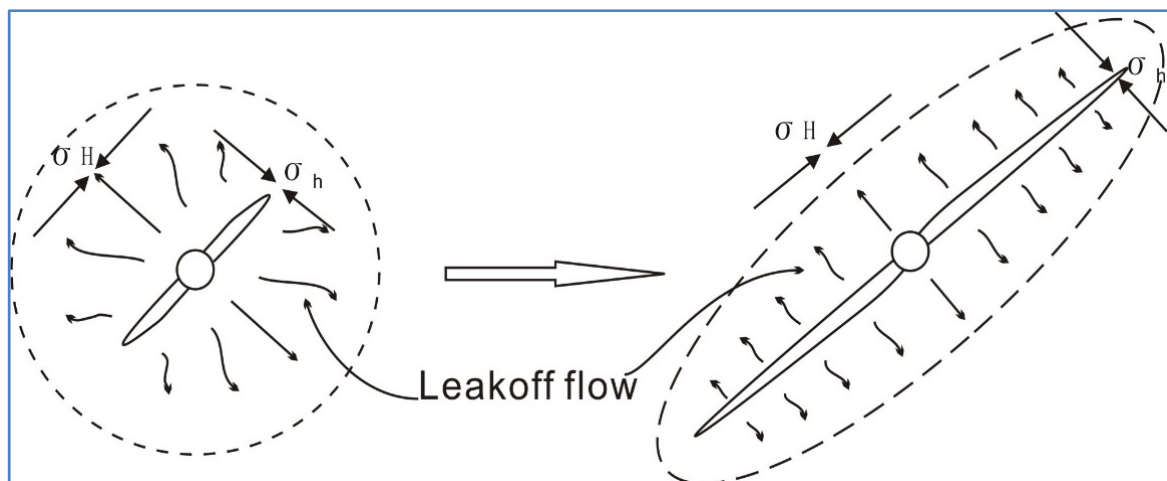
Fig.3.1 Evolution of Flow System.

Perkins and Gonzalez (1985) presented a semi-analytical model of a waterflood-induced fracture initiating from a single well in an infinite reservoir. Their model has two main features. First, the leak-off distribution near the fracture is two-dimensional with the

pressure transient moving elliptically outward into the reservoir with respect to the growing fracture. Second, the effect of temperature change on reservoir rock stress and therefore on the fracture propagation process was incorporated. It was demonstrated that cooling of the reservoir rock by injection of cold water might cause fractures to become very long and narrow compared to the hydraulic fractures without cooling.

Koning (1985) presented an analytical model to simulate the waterflood-induced fracture growth under the combined influence of poroelastic and thermoelastic effects in reservoir stress. His model assumed the fracture geometry based on the traditional PKN fracture propagation model. The pore pressure and temperature effects were considered on the stresses changes around the hydraulic fracture and on fracture propagation. In addition, the analytical model also included an estimation of the 3-D poroelastic and thermoelastic stress change near the fracture surface.

In this work, a hydraulic fracturing propagation model was setup based on the proposed model of Koning and the work by Perking and Gonzales. For the pore pressure distributions during hydraulic fracturing process, the workflow from the Koning's work was employed.

Considering any a 2-D point (x, y) around the hydraulic fracture, the relations between the elliptical coordinates and the Cartesian coordinates could be expressed as shown in the following equations:

$$x = L_f \cosh \xi \cos \eta \tag{3.1}$$

$$y = L_f \sinh \xi \sin \eta \tag{3.2}$$

The pore pressure distribution at any place around the hydraulic fracture in the horizontal plane is a function of time and can be given by (Koning, 1985):

$$P(\xi, \eta, t) = P_i + \Delta p(\xi) \tag{3.3}$$

In which:

$$\Delta p_1(\xi) = \frac{q}{2\pi k h \lambda_1} \ln\left(\frac{3.0\sqrt{\kappa t}}{L\cosh\xi + L\sinh\xi}\right); \ \xi_1 \leq \xi < \xi_2 \tag{3.4}$$

$$\Delta p_2(\xi) = \frac{q}{2\pi k h \lambda_2} \ln\left(\frac{a_1 + b_1}{L\cosh\xi + L\sinh\xi}\right) + \Delta P_1; \ \xi_0 \leq \xi < \xi_1 \tag{3.5}$$

$$\Delta p_3(\xi) = \frac{q}{2\pi k h \lambda_3} \ln\left(\frac{a_0 + b_0}{L\cosh\xi + L\sinh\xi}\right) + \Delta P_1 + \Delta P_2; \ 0 \leq \xi < \xi_0 \tag{3.6}$$

In which, q is injection rate, k is the permeability, h is the fracture half height, and L is the fracture half length. The details of the parameters in the equations could be found in the Nomenclature. Among the above equations:

$$\begin{aligned}
\lambda_1 &= kk_{rw}/\mu_o \\
\lambda_2 &= kk_{rw}/\mu_{hot} \\
\lambda_3 &= kk_{rw}/\mu_{cold}
\end{aligned} \tag{3.7}$$

$$\kappa = \frac{k}{\phi\mu_o c_f} \tag{3.8}$$

Where c_f is the formation compressibility. And

$$\Delta P_1 = i_w \mu_o \ln(\frac{3\sqrt{\kappa t}}{a_1 + b_1}) / (2\pi k k_{rw} h) \qquad (3.9)$$

$$\Delta P_2 = i_w \mu_w^{hot} \ln(\frac{a_1 + b_1}{a_0 + b_0}) / (2\pi k k_{rw} h) \qquad (3.10)$$

The above equations are the pressure distributions in different elliptical zones surrounding the fracture. At a certain time, t, the pore pressure distribution can be estimated. Therefore, at every time step, we can get a plot of the distribution for the pore pressure around the fracture. A case example on the pressure distribution is illustrated in Fig.3.2.

At the condition of continuing water injection after hydraulic fracturing, Warpinski and Teufel (1987) proposed the pressure transient profile for the pore pressure distribution at a certain injection time. This pressure profile in an infinite joint is approximately given by:

$$p(y,t) = p_f - (p_f - p_r)(y / y_f) \qquad (3.14)$$

Where p_f is the average treating pressure in hydraulic fracture over the entire treatment time and p_r is the original reservoir in-situ pore pressure. y_f is the location of the fluid front which is approximated given as (Modified from Koning, 1985):

$$y_f = 1.5\sqrt{\frac{kt}{\phi \mu c_t}} \qquad (3.15)$$

The details of the estimation of the fracture length, as well as the dimensions of the cooled and flooded regions, are given in the Appendix D (Ge, 2009).

An example was given with the parameters from Perkins and Gonzales (see Table3.1) to

estimate the 2-D dimensions of hydraulic fracture, as well as the cooled and flooded regions, and pressure distribution around a hydraulic fracture. As illustrated in the Fig. 3.2, the pore pressure distribution is near co-focal ellipses around the fracture, and its value reaches highest at the fracture surface and decays to the original reservoir pore pressure in the far field. Fig.3.2 shows the pore pressure distribution around the fracture at injection time t=100 days. The pattern of pore pressure distribution is elliptical as expected.

Based on the method from Perkins and Gonzales (1985) as described in Appendix D, this model gives that the half-fracture length is about 137 feet (41 m) at t=100 days. The extents of the various invaded zones are a_0=148 ft and b_0=57 ft for the cooled region, a_1=222 ft and b_1=175 ft and for the waterflooded region (Fig.3.3).
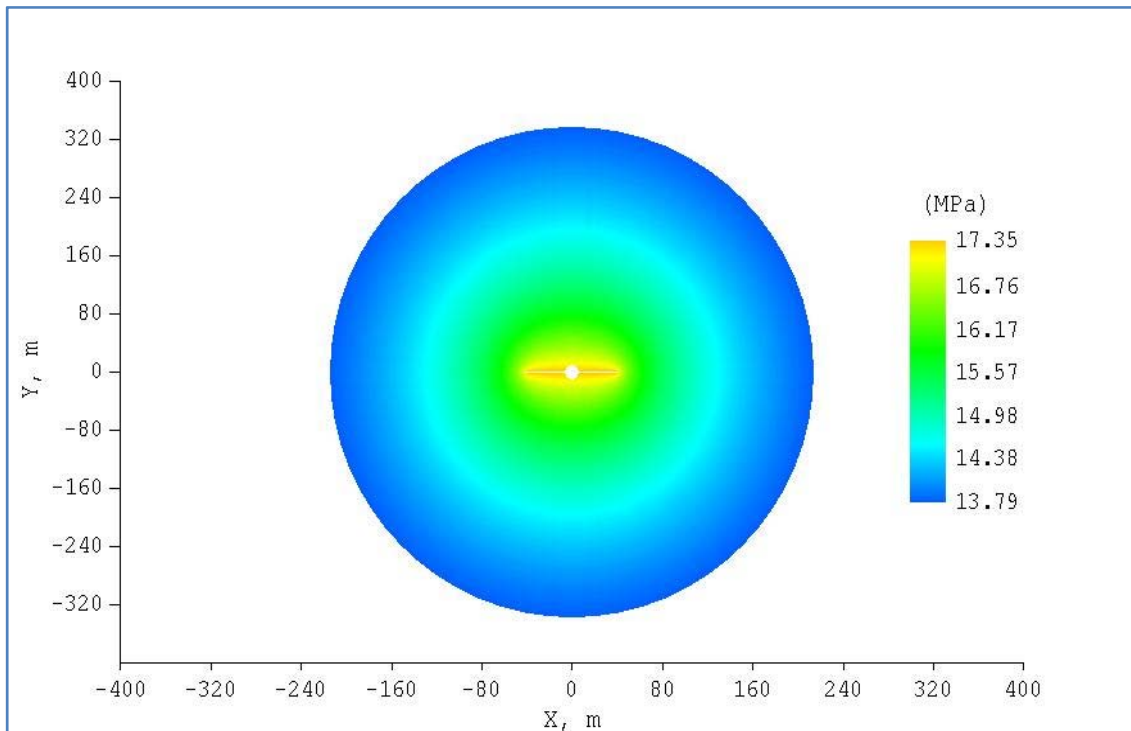
Fig.3.2 Hydraulic Fracturing Propagation at t=100 Days.

Table 3.1 Input Parameters for Simulations (Perkin and Gonzalez, 1985)

Parameter	Value	Unit
Depth (D):	1524	m
Reservoir Thickness (h):	30.5	m
Water injection rate (Iw):	477	m^3/d
Time (t):	5	year
Initial Reservoir temperature (TR):	65.6	°C
Bottomhole temp. of the injection water (Tw):	21.1	°C
Undisturbed reservoir fluid pressure (Pr):	13.78	MPa
Compressibility of mineral grains (cgr):	2.20E-05	1/Mpa
Compressibility of fracture (cf):	4.08E-04	1/Mpa
Young's modulus (E):	1.38E+04	MPa
Relative perm. to water at residual oil saturation (krw) :	0.29	
Residual oil saturation (Sor):	0.25	
Initial water saturation (Swi):	0.2	
Rock surface energy (U):	5.00E-02	kJ/m^2
Linear coefficient of thermal expansion (β):	5.60E-06	1/K
Poisson's ratio (v):	0.15	
Density * Specific heat of mineral grains (ρgr*Cgr):	2347	kJ/ (m^3*K)
Minimum horizontal stress (Sh):	24.1	MPa
Porosity (Φ):	0.25	
SH/Sh:	1.35	
Reservoir permeability (k):	4.94E-14	m^2
Compressibility of oil (co):	1.50E-03	1/Mpa
Compressibility of water (cw):	5.20E-04	1/Mpa
Specific heat of oil (Co):	2.1	kJ/(kg*K)
Specific heat of water (Cw):	4.2	kJ/(kg*K)
Viscosity of oil at 65.6 °C (μo):	1.47E-09	MPa*s
Viscos ity of water at 65.6 °C (μw):	4.30E-10	MPa*s
Viscosity of water at 21.1°C (μw):	9.95E-10	MPa*s
Density of oil (ρo):	881	kg/m^3
Density of water (ρw):	1000	kg/m^3

Fig.3.3 shows the fracture length and the major and minor axis of cooled and flooded zone

as a function of time. The major axis of cooled region is almost the same as fracture length

with time.
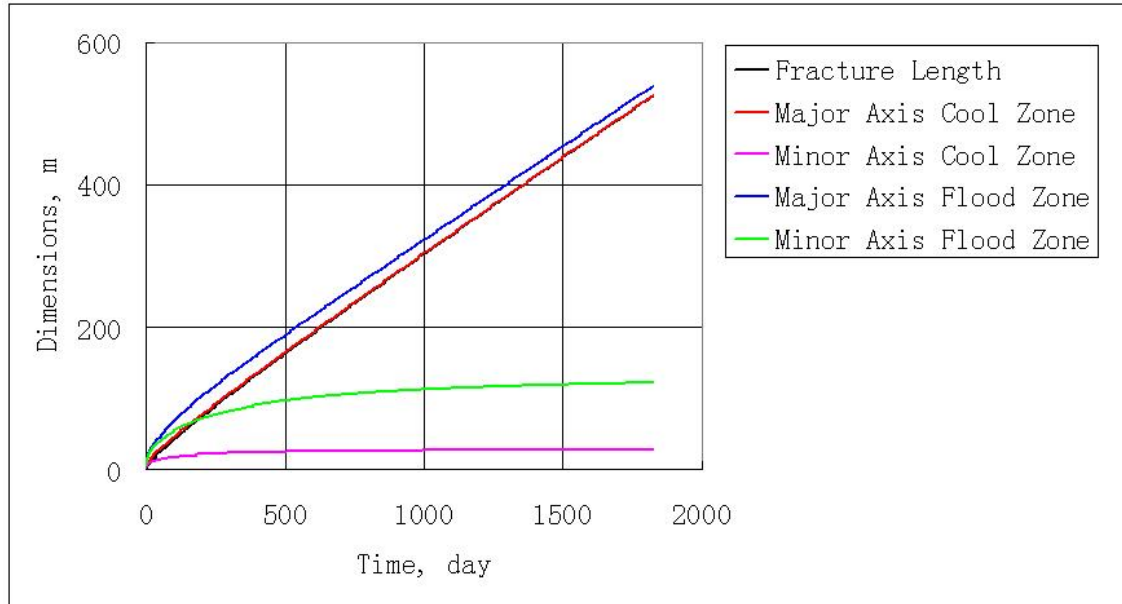
Fig. 3.3 Fracture Length and Major and Minor Axis of Cooled and Waterflooded Zones as a Function of Time.

3.2 Waterflooded Hydraulic Fracturing Model

To further investigate the pore pressure and stress distributions around a hydraulic fracture, a second model was constructed on the waterflooding process. As discussed previously, most hydraulic fractures are induced intentionally in low permeability reservoirs to increase the injectivity, especially in the low permeability reservoirs. As fluids at temperatures cooler than the reservoir temperatures are injected into a well, a region of cooled rock forms around an injection well and grows as additional fluid is injected. The rock within the cooled region contracts and this leads to a decrease in stress concentration around the injection well until the injection pressure minus the hoop stress exceeds the tensile strength of the rock at a critical point on the well boundary and a fracture begins to

37

propagate to orient itself in the direction of maximum in-situ stress.

The hydraulic fracture model in this study is modified and updated from previous studies by Ge and Ghassemi (2007, 2008, 2011, 2012, 2014). When cold water is injected into a line crack (representing a section of a two-wing, vertical hydraulic fracture), the flooding front will progress outward, and its outer boundary at any time can be described approximately as an ellipsoid that is confocal with the line crack on the horizontal plane (Muskat, 1946; Koning, 1985; Perkins and Gonzalez, 1985). Due to temperature difference between the injected fluid and the formation, a cooled region will progress outward from the injection well but lag behind the flood front. In the plan view of the fracture, if an ideal homogeneous condition is assumed, the outer boundary of the waterflooded and cooled region will be elliptical and confocal with the line crack (Fig. 3.4 and 3.5 with exaggeration on dimensions).

A vertical hydraulic fracture is assumed to form against the minimum horizontal stress direction. As shown in Fig.3.4 and 3.5, a 3-D penny shaped vertical hydraulic fracture is assumed with the waterflooded region, temperature affected (cooled) region, and the pressure affected region. At any injection time, the fracture dimensions (including fracture length, height, and aperture) and the zone boundaries are also estimated in this model with the same method as in previously published literatures (Ge and Ghassemi 2007, 2008, 2011, 2012, 2014; Perkins and Gonzalez, 1985).

With this waterflooded hydraulic fracturing model, the pore pressure and stress redistributions could be estimated around the hydraulic fracture, and further the reactivations of natural fractures could be predicted.

38
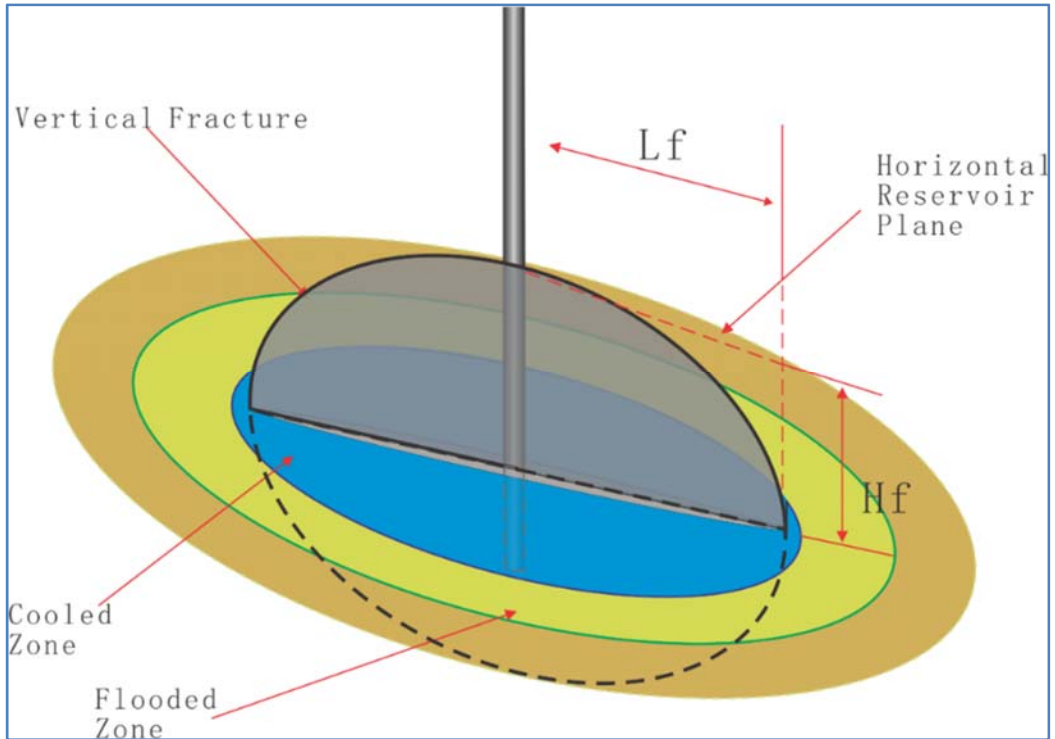
Fig.3.4 Plan View of Two-winged Hydraulic Fracture from a Vertical Well (Ge, 2014).
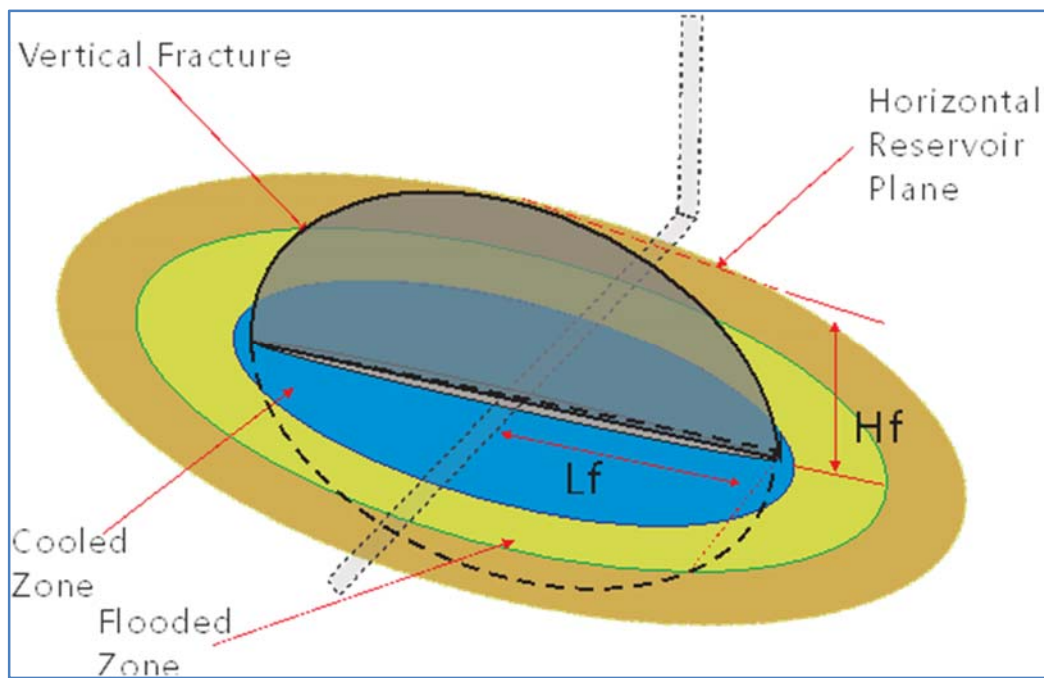
Fig.3.5 Plan View of Two-winged Hydraulic Fracture from a Horizontal Well.

3.3 3-D Pore Pressure Distribution Model

With the fracture propagation, the pore pressure is increasing in the reservoir formation around the fracture. The pore pressure variation due to the water flooding is one of the most important factors that can affect the stress variations and the reactivations of natural fractures. The fracture is assumed to be a 3-D flat elliptic crack at any specific time. Therefore, at a moment after hydraulic fracturing, pore pressure distribution due to the fluid leakoff from the main hydraulic fracture follows the linear flow approximation and can be estimated by assuming an ellipsoidal shape in 3-D. The simplified expression for the pore pressure distribution in a liquid saturated reservoir is approximately given by (Warpinski, et al., 2004):

$$P(\lambda, \varepsilon) = P_o + (P_f - P_o)e^{-\zeta\lambda(1+\sqrt{\varepsilon+b^2})} \tag{3.16}$$

Where λ and ε are the ellipsoidal coordinates, p_f is the average pressure in hydraulic fracture over the entire treatment time and p_o is the original reservoir pore pressure. Here in this equation, the involving of coordinate ε is to consider the pressure decay near the fracture tip region. The value of the leakoff factor ζ can be expressed as:

$$\zeta = \left(\frac{g\pi}{2}\right)^2 \tag{3.17}$$

$$g = \sqrt{\frac{\varphi\mu c}{kt}} \tag{3.18}$$

In which, φ is the porosity, μ is the viscosity, c is the compressibility, k is the relative permeability, and t is waterflooding time. The coordinates are converted from ellipsoidal coordinates system to Cartesian coordinates system in the model program to keep in

40

consistence with the calculations of stresses. For most tight gas and shale reservoirs, the permeability of rock matrix is too small, so the effects from natural fractures could be very large. In this study, we updated the pore pressure calculation in our previous model by considering the both the fracture permeability and matrix permeability. This update makes the model more accurate and applicable in the low permeable and naturally fractured shale reservoirs.

Warpinski et al, 2008 pointed out that the induced pressure change by hydraulic fracturing is a complex 3-D problem and time dependent. They considered two separate types of reservoirs (liquid saturated and gas reservoirs) and two formation conditions (matrix and natural fracture leakoff). They used the above equations for liquid reservoir by assuming the natural fracture has small effects on the pressure distribution (Warpinski, et al., 2004). However, they also pointed out that the naturally fractured reservoir could also be accommodated by considering the fracture permeability. For the gas reservoirs, by assuming the natural fractures as the main contribution on the fluid leakoff, the same equations can be used for the pore pressure distribution. Details about the equations on pore pressure in gas reservoirs can be found in Warpinski's work (Warpinski, et al., 2004).

In this study, we employed the equations 3.16-3.18 for estimating the 3-D pore pressure distribution, but with effective permeability. The estimations of poroelastic stresses are also based on this 3-D pore pressure distribution, as shown in Chapter 4. An example of the pore pressure distribution around a hydraulic fracture in 3-D is shown in Fig. 3.6.
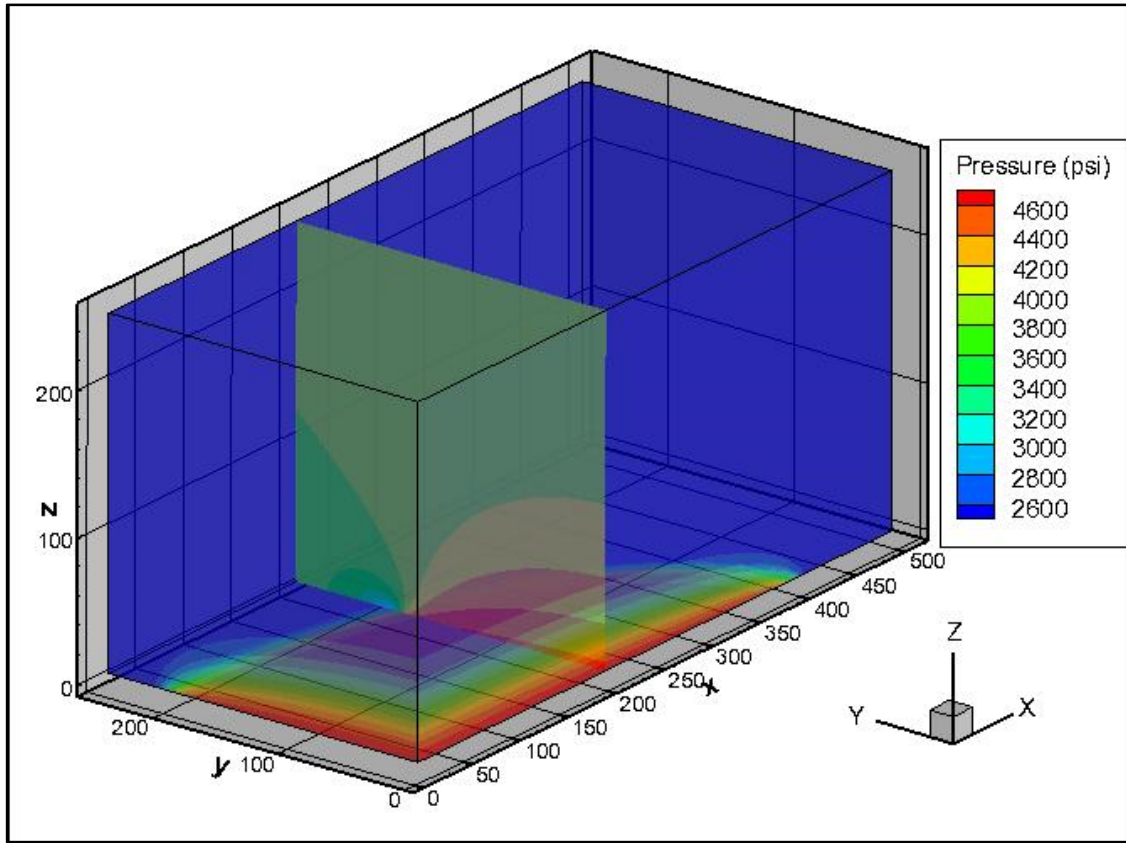
Fig. 3.6 3-D Pore Pressure Distribution around a Hydraulic Fracture (1/8 part of the whole region).

CHAPTER IV

STRESS REDISTRIBUTION AROUND THE HYDRAULIC FRACTURE

In previous chapter, the pore pressure distributions around a hydraulic fracture are discussed. In this chapter, the stresses distributions around a hydraulic fracture will be examined at any point near the fracture surface.

Fracturing of water injection wells can occur either in tight or in permeable reservoirs. In tight reservoirs fractures are usually induced intentionally to increase the injectivity. In permeable reservoirs, fracturing may occur unintentionally if cold water is injected into a relatively hot reservoir. During water-flooding or other secondary or tertiary recovery processes, fluids at temperatures cooler than the in-situ reservoir temperatures are injected into a well. A region of cooled rock forms around an injection well, and grows as additional fluid is injected. The rock within the cooled region contracts and this leads to a decrease in stress concentration around the injection well until the injection pressure minus the hoop stress exceeds the tensile strength of the rock at a critical point on the well boundary and a fracture begins to propagate to orient itself in the direction of maximum in-situ stress. Although the increase in injectivity is favorable, the fracture may have an adverse effect on the sweep efficiency of the water drive in the case of waterflooding.

Perkins and Gonzalez (1985) presented a semi-analytical model of a water-flood-induced fracture emanating from a single well in an infinite reservoir. Their model has two important features. First, the leak-off distribution is two-dimensional with the pressure transient moving elliptically outward into the reservoir with respect to the growing fracture. Second, the effect of thermoelastic changes on reservoir rock stress and therefore on

fracture propagation pressure was incorporated. It was shown that cooling of the reservoir rock following injection of cold water may cause fractures to become very long.

Koning (1985) presented an analytical model for waterflood-induced fracture growth under the influence of poro- and thermoelastic changes in reservoir stress. He assumed the fracture geometry from the traditional PKN fracture propagation model. By considering the pore pressure and temperature effects on the stress changes around a hydraulic fracturing and on fracture propagation, an analytical model was also given for the 3-D poroelastic and thermoelastic stress change at the fracture surface.

In my previous studies (Ge, 2009), a waterflooding pressure and stress distribution (WFPSD) model and natural fracture stimulation (FracJStim) model were developed separately to calculate the fracture propagation dimensions (Appendix D) and two dimensional distributions of stresses around a propagation hydraulic fracture and a stabilized fracture (Appendix C).

In this study, the 3-D stress redistributions around a hydraulic fracture mainly rely on the induced stresses by thermoelasicity, poroelasticity and fracture compression. The stress redistribution around a hydraulic fracture is very important for the multiple fracturing design, for the estimation of stimulated reservoir volume, for the permeability enhancement prediction, and for the potentials of the refracturing operations. The local stress field near to the opened hydraulic fracture can be affected greatly by the compression from the fracture surface, the intrusion of waterflooding, and the temperature change. This work is based on the previous work by Ge (2009), and improved with the 3-D redistributions of pore pressure and stresses.

4.1 Expressions for Stresses

The stresses at any point around the fracture are mainly affected by the following factors: pore pressure change, temperature change, and the presence of the fracture. In this study, the original three principal stresses are assumed to be σ_v, σ_H, and σ_h and they are in the y, x and z coordinates respectively. The stresses at any point (x, y, z) surrounding the fracture are given by:

$$\sigma_{xx} = \sigma_H + \Delta\sigma_{Px} + \Delta\sigma_{Tx} + \Delta\sigma_{Fx} \tag{4.1}$$

$$\sigma_{yy} = \sigma_v + \Delta\sigma_{Py} + \Delta\sigma_{Ty} + \Delta\sigma_{Fy} \tag{4.2}$$

$$\sigma_{zz} = \sigma_h + \Delta\sigma_{pz} + \Delta\sigma_{Tz} + \Delta\sigma_{Fz} \tag{4.3}$$

$$\sigma_{xy} = \Delta\sigma_{Pxy} + \Delta\sigma_{Txy} + \Delta\sigma_{Fxy} \tag{4.4}$$

$$\sigma_{xz} = \Delta\sigma_{pxz} + \Delta\sigma_{Txz} + \Delta\sigma_{Fxz} \tag{4.5}$$

$$\sigma_{yz} = \Delta\sigma_{pyz} + \Delta\sigma_{Tyz} + \Delta\sigma_{Fyz} \tag{4.6}$$

Where σ_H is the in-situ maximum horizontal stress, σ_h is the minimum in-situ horizontal stress; σ_v is the vertical stress; $\Delta\sigma_P$ is the change of stress due to pore pressure change; $\Delta\sigma_T$, the change of stress due to temperature change; and $\Delta\sigma_F$ is the change of stress due to the presence of the fracture (Subscript Index: H - maximum horizontal; h - minimum horizontal; p – by pore pressure change; T – by temperature change; F – by fracture compression). With the induced stresses and in-situ stresses, the

total principal stresses around the crack can be calculated by stresses transformation equations, which can be found in some reference (Warpinski et al., 2004; Jaeger and Cook, 1979) and the common stress transformation process is not discussed in this study.

4.2 Poroelastic and Thermoelastic Induced Stresses

The estimation of poroelastic and thermoelastic induced stresses were given by Koning (1985) and by Perkins and Gonzales (1985). The two-dimensional induced stresses by the compression from fracture opening were given by fracture mechanics (Jaeger and Cook, 1979; Atkinson, 1989). Ge (2009) also deduced the governing equations and programmed the 2-D induced stresses by poroelasticity, thermoelasticity, and fracture compression, and more details could be found in the Appendix C. The 3-D stress variations around a fracture were also studied by Ge and Ghassemi (2014).

In this study, the thermoelastic induced stresses are still estimated with the method originally from Perkins and Gonzales (1985):

$$\frac{(1-\nu)\Delta\sigma_{Ty}}{E\beta\Delta T} = \frac{(b_0/a_0)}{1+(b_0/a_0)} + \left[\frac{1}{1+(b_0/a_0)}\right]$$
$$\left(1/\left\{1+\frac{1}{2}\left[1.45(\frac{h}{2b_0})^{0.9}+0.35(\frac{h}{2b_0})^2\right]\left[1+(\frac{b_0}{a_0})^{0.774}\right]\right\}\right)$$

(4.7)

$$\frac{(1-\nu)\Delta\sigma_{Tx}}{E\beta\Delta T} = \frac{1}{1+(b_0/a_0)} + \left[\frac{(b_0/a_0)}{1+(b_0/a_0)}\right]$$
$$\left(1/\left\{1+\left[1.45(\frac{h}{2b_0})^{0.9}+0.35(\frac{h}{2b_0})^2\right]\left[1+(1-\frac{b_0}{a_0})^{1.36}\right]\right\}\right)$$

(4.8)

In which, ν is Poisson's ratio, E is Young's Modulus, ΔT is temperature change, h is the half fracture height, a_0 and b_0 are the semi axis of the cooled region, and β is the coefficient

of thermal expansion.

The poroelastic induced stresses were estimated similarly with equations 4.7 and 4.8 with ΔP instead of ΔT, a_1 and b_1 the dimensions of the waterflooded region instead of a_0 and b_0 the dimensions of cooled region, and poroelastic coefficient instead of coefficient of thermal expansion. The detailed calculation of the dimensions of the cooled and waterflood regions are based on the methods given in the previous studies (Ge and Ghassemi, 2007; Perkins and Gonzalez, 1985). In petroleum field, especially in shale reservoirs, due to the temperature difference between injection fluids and reservoir fluids is small, the thermoelastic effects on stress changes is less important than poroelastic stresses. Therefore, it was originally assumed that the temperature distribution around the fracture is uniform and elliptically distributed as an example shown in Fig. 4.1 (Ge, 2009).
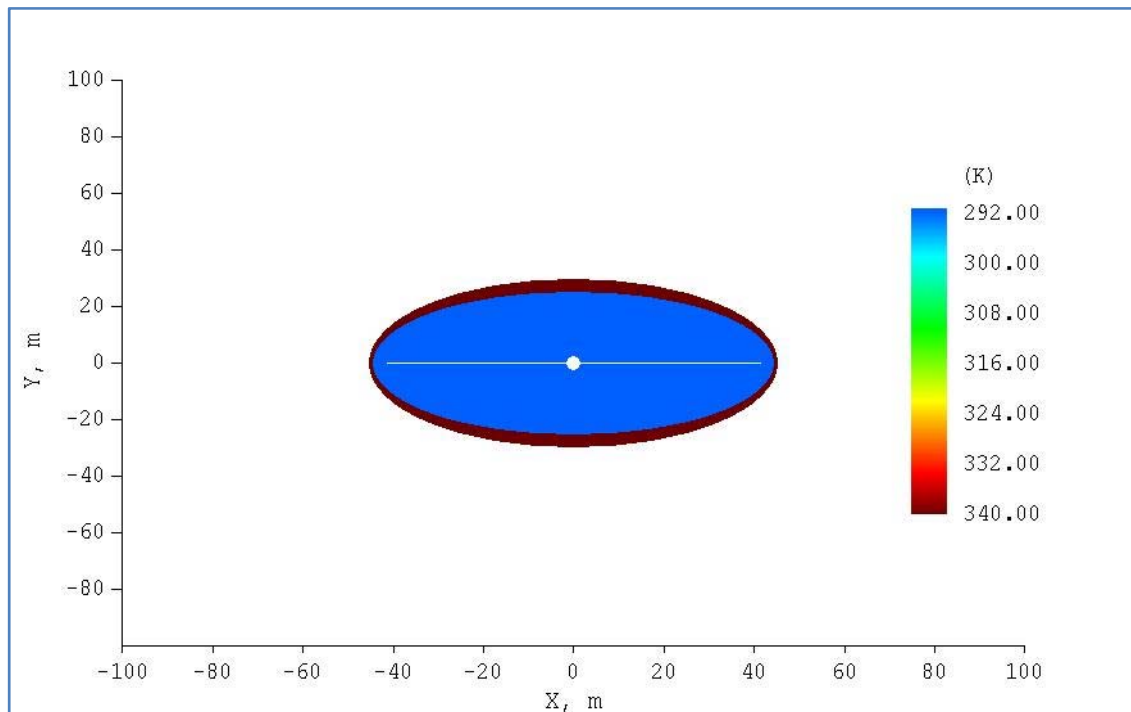
Fig.4.1 Temperature Distribution Surrounded the Fracture.

47
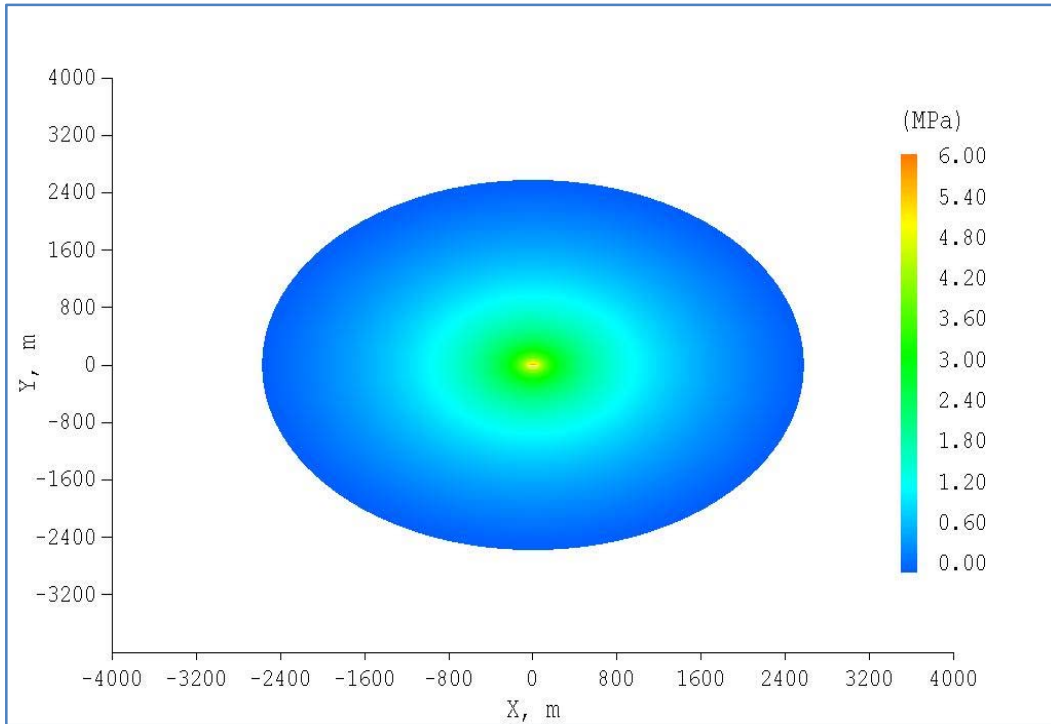
Fig.4.2 Poro-Induced Stresses Distribution Y Axis Direction (t=100 Days).
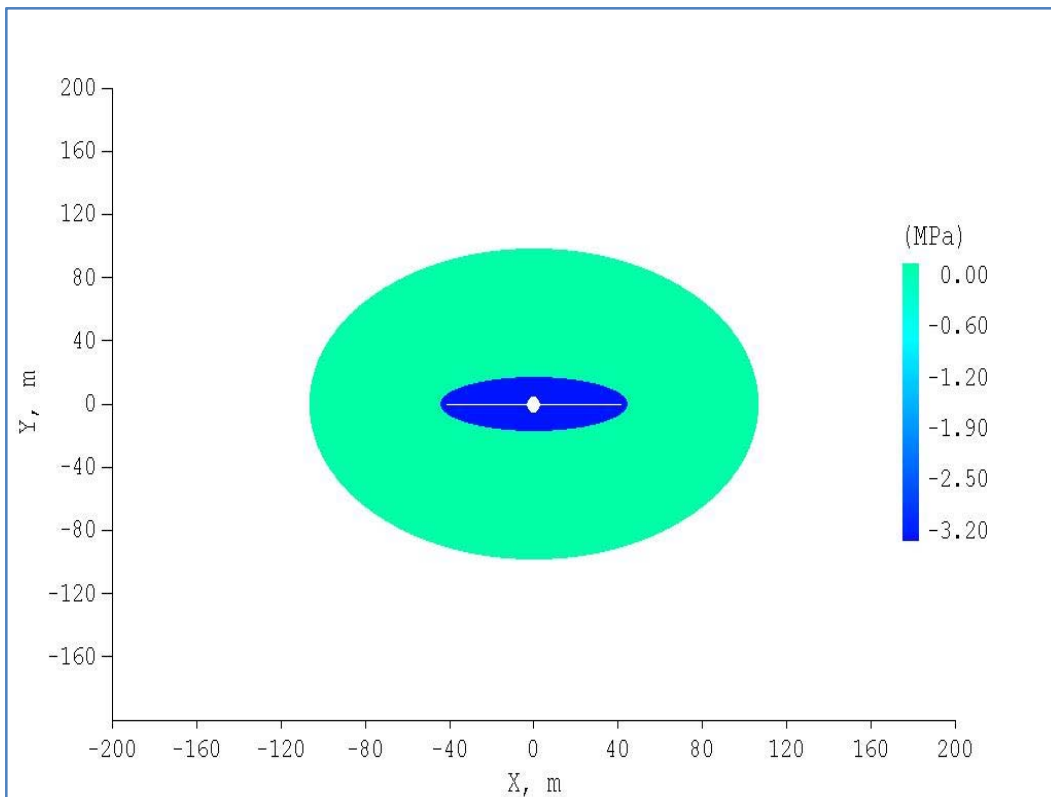
Fig.4.3 Thermo-Induced Stresses Distribution X Axis Direction (t=100 Days).

48

The examples of poroelastic and thermoelastic induced stresses could also be found in my previous studies (Ge, 2009). Here Fig. 4.2 and 4.3 give an example on the poroelastic and thermoelastic stress respectively.

In this study, these calculations are updated with the 3-D dimensions around the fracture, which is based on the penny shaped fracture propagation dimensions. The temperature distribution was also updated based on the Carslaw & Jaeger's (1959) Solution for Temperature Distribution around a Crack.

4.3 Induced Stresses by Fracture Compression

The more accurate 3-D stress changes due to fracture compression are employed according to the analysis for a constant pressurized flat crack in a homogeneous material from a potential function (Green and Sneddon, 1950; Kassir and Sih, 1966; Sid and Liebowitz, 1968; Jaeger and Cook, 1979):

$$\Phi = \frac{ab^2(p_f - \sigma_{min})}{32G\ E(k)} \int_\lambda^\infty \left(\frac{x^2}{a^2+s} + \frac{y^2}{b^2+s} + \frac{Z^2}{s} - 1 \right) \frac{ds}{\sqrt{s(a^2+s)(b^2+s)}} \qquad (4.9)$$

In which, the potential function Φ is give in an ellipsoidal coordinate system, which is defined by (λ, μ, ε). The definite integral is given by the function of the variable s in the interval [λ, ∞]. G is the shear modulus, p_f is the internal pressure, a is the half-length, and b is the half height of the crack. Coordinates are x (fracture length direction), y (fracture height direction, which is vertical for vertical fracture) and Z (horizontally perpendicular to the fracture surface). E(k) is the complete elliptic integral of the second kind, k is the modulus defined by:

$$k = \sqrt{a^2 - b^2}/a \tag{4.10}$$

Thus, the induced stresses by fracture were solved and expressed in terms of coordinates, elliptic functions, and elliptical integrals as shown in equation 4.11-4.16 (Ge and Ghassemi, 2014).

$$\sigma_{xx} = 8G\left(\frac{2A}{a^3k^2}\{u - E(u)\} + \frac{2Ax}{a^3k^2}\left\{sn^2u\frac{du}{d\lambda}\frac{\partial\lambda}{\partial x}\right\} + 2v\frac{2A}{a^3k^2}\left\{\left(\frac{a}{b}\right)^2 E(u) - u - \right.\right.$$

$$\frac{a^2-b^2}{b^2}\frac{(snu)(cnu)}{dnu}\right\} + \frac{2Ay}{a^3k^2}\left\{\left(\frac{a}{b}\right)^2 dn^2u - 1 - \frac{a^2-b^2}{b^2}\left(\frac{cn^2u}{dn^2u} - sn^2u\right)\right\}\frac{du}{d\lambda}\frac{\partial\lambda}{\partial y} +$$

$$z\frac{2A}{a^3}\left\{sn^2u\frac{du}{d\lambda}\frac{\partial\lambda}{\partial z}\right\} + \frac{2Ax}{a^3k^2}\left(\begin{array}{c}2(snu)(cnu)(dnu)\left(\frac{du}{d\lambda}\right)^2\frac{\partial\lambda}{\partial x}\frac{\partial\lambda}{\partial z} + \\ sn^2u\left(\frac{d^2u}{d\lambda^2}\frac{\partial\lambda}{\partial x}\frac{\partial\lambda}{\partial z} + \frac{du}{d\lambda}\frac{\partial^2\lambda}{\partial x\partial z}\right)\end{array}\right)\right) \tag{4.11}$$

$$\sigma_{xy} = 8G\left[(1-2v)\left(\frac{2Ax}{a^3}\left\{sn^2u\frac{du}{d\lambda}\frac{\partial\lambda}{\partial y}\right\}\right) + Z\left(\frac{2Ax}{a^3}\left\{2(snu)(cnu)(dnu)\left(\frac{du}{d\lambda}\right)^2\frac{\partial\lambda}{\partial Z}\frac{\partial\lambda}{\partial y} + \right.\right.\right.$$

$$\left.\left.\left. sn^2u\left(\frac{d^2u}{d\lambda^2}\frac{\partial\lambda}{\partial y}\frac{\partial\lambda}{\partial Z} + \frac{du}{d\lambda}\frac{\partial^2\lambda}{\partial y\partial Z}\right)\right\}\right)\right] \tag{4.12}$$

$$\sigma_{xz} = 8GZ\frac{2A}{ab^2}\left\{k'^2\frac{sn^2u}{cn^2u}\right\}\frac{du}{d\lambda}\frac{\partial\lambda}{\partial x} + \frac{2AZ}{ab^2}\left\{\left(\frac{(k'^2)(snu)(dnu)}{cn^3u}\right)\left(\frac{du}{d\lambda}\right)^2\frac{\partial\lambda}{\partial x}\frac{\partial\lambda}{\partial Z} + \right.$$

$$\left.\left(k'^2\frac{sn^2u}{cn^2u}\right)\left(\frac{d^2u}{d\lambda^2}\frac{\partial\lambda}{\partial x}\frac{\partial\lambda}{\partial Z} + \frac{du}{d\lambda}\frac{\partial^2\lambda}{\partial x\partial Z}\right)\right\} \tag{4.13}$$

$$\sigma_{yy} = 8G\left(\frac{2A}{a^3k^2}\left\{\left(\frac{a}{b}\right)^2 E(u) - u - \frac{a^2-b^2}{b^2}\frac{(snu)(cnu)}{dnu}\right\} + \frac{2Ay}{a^3k^2}\left\{\left(\frac{a}{b}\right)^2 dn^2u - 1 - \right.\right.$$

$$\frac{a^2-b^2}{b^2}\left(\frac{cn^2u}{dn^2u} - sn^2u\right)\right\}\frac{du}{d\lambda}\frac{\partial\lambda}{\partial y} + 2v\frac{2A}{a^3k^2}\{u - E(u)\} + \frac{2Ax}{a^3k^2}\left\{sn^2u\frac{du}{d\lambda}\frac{\partial\lambda}{\partial x}\right\} +$$

$$Z\frac{2A}{a^3k^2}\left\{\left(\frac{a}{b}\right)^2 dn^2u - 1 - \frac{a^2-b^2}{b^2}\left(\frac{cn^2u}{dn^2u} - sn^2u\right)\right\}\frac{du}{d\lambda}\frac{\partial\lambda}{\partial Z} +$$

$$\frac{2Ay}{a^3k^2}\left\{\left(\frac{a}{b}\right)^2 2(-k^2)(dnu)(cnu)(snu) + 2\frac{a^2-b^2}{b^2}\left(\frac{(k\prime^2)(snu)(cnu)}{dn^3u} + \right.\right.$$

$$\left.\left.(snu)(cnu)(dnu)\right)\right\}\left(\frac{du}{d\lambda}\right)^2\frac{\partial\lambda}{\partial y}\frac{\partial\lambda}{\partial Z} + \frac{2Ay}{a^3k^2}\left\{\left(\frac{a}{b}\right)^2 dn^2u - 1 - \right.$$

$$\left.\frac{a^2-b^2}{b^2}\left(\frac{cn^2u}{dn^2u} - sn^2u\right)\right\}\left\{\frac{d^2u}{d\lambda^2}\frac{\partial\lambda}{\partial y}\frac{\partial\lambda}{\partial Z} + \frac{du}{d\lambda}\frac{\partial^2\lambda}{\partial y\,\partial Z}\right\}\right) \tag{4.14}$$

$$\sigma_{zz} = 8G\left(-\frac{2A}{ab^2}\left\{\frac{(snu)(dnu)}{cnu} - E(u)\right\} + \frac{2AZ}{ab^2}\left\{k\prime^2\frac{sn^2u}{cn^2u}\right\}\frac{du}{d\lambda}\frac{\partial\lambda}{\partial Z} + \frac{2AZ^2}{ab^2}\left\{k\prime^2\frac{sn^2u}{cn^2u}\right\}\left\{\frac{d^2u}{d\lambda^2}\left(\frac{\partial\lambda}{\partial Z}\right)^2 + \right.\right.$$

$$\left.\left.\frac{du}{d\lambda}\frac{\partial^2\lambda}{\partial Z^2}\right\} + \frac{4AZ^2}{ab^2}\left\{k\prime^2\frac{(snu)(dnu)}{cn^3u}\right\}\left(\frac{du}{d\lambda}\right)^2\left(\frac{\partial\lambda}{\partial Z}\right)^2\right) \tag{4.15}$$

$$\sigma_{yz} = 8GZ\frac{2A}{ab^2}\left\{k\prime^2\frac{sn^2u}{cn^2u}\right\}\frac{du}{d\lambda}\frac{\partial\lambda}{\partial y} + \frac{2AZ}{ab^2}\left\{\left(\frac{(k\prime^2)(snu)(dnu)}{cn^3u}\right)\left(\frac{du}{d\lambda}\right)^2\frac{\partial\lambda}{\partial y}\frac{\partial\lambda}{\partial Z} + \right.$$

$$\left.\left(k\prime^2\frac{sn^2u}{cn^2u}\right)\left(\frac{d^2u}{d\lambda^2}\frac{\partial\lambda}{\partial y}\frac{\partial\lambda}{\partial Z} + \frac{du}{d\lambda}\frac{\partial^2\lambda}{\partial y\,\partial Z}\right)\right\} \tag{4.16}$$

In which G is the shear modulus, p_f is the average internal pressure in the hydraulic fracture, a is the fracture half length, b is the fracture half height, corresponding to the L_f and H_f in the Fig.3.5. The functions snu (elliptic sine sn u), cnu (elliptic cosine cn u) and dnu (delta amplitude dn u) are Jacobian elliptic functions as inverses of the incomplete elliptic integral of the first kind, A is given by:

$$A = \frac{ab^2(p_f - \sigma_{min})}{16G\,E(k)} \tag{4.17}$$

And u(λ) is defined as: no vertical lines above and below

$$\lambda = \frac{a^2 cn^2u}{sn^2u} \tag{4.18}$$

The ellipsoidal coordinates are defined by:

$$a^2(a^2 - b^2)x^2 = (a^2 + \lambda)(a^2 + \mu)(a^2 + \varepsilon) \qquad (4.19)$$

$$b^2(b^2 - a^2)y^2 = (b^2 + \lambda)(b^2 + \mu)(b^2 + \varepsilon) \qquad (4.20)$$

$$a^2 b^2 z^2 = \lambda\mu\varepsilon \qquad (4.21)$$

The above equations are expressed in terms of coordinates, elliptic functions, and elliptical integrals. The detailed process for deduction of these expressions will not be involved here due to the limitation of the thesis length, but will be seen in the Appendix A. A specific case study is performed with the equations and programmed in FORTRAN language. The parameters used in this case are reasonable values for a liquid saturated sandstone reservoir at a depth of approximately 5000 ft. Fig.4.4 to Fig.4.6 are examples on the stress redistributions around the hydraulic fracture
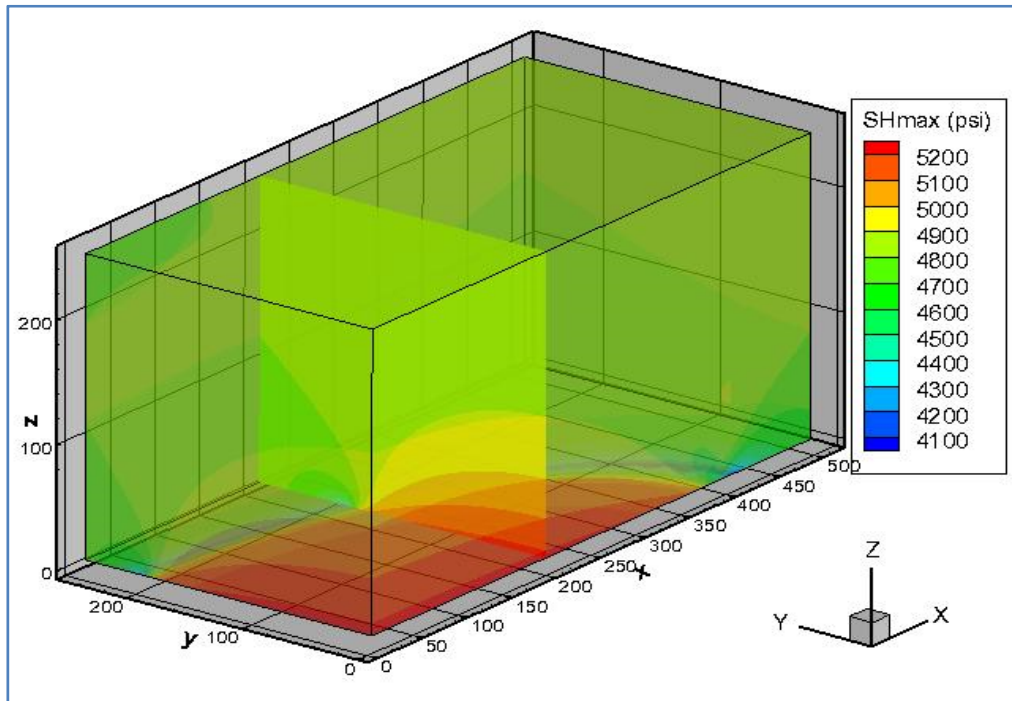
Fig. 4.4 Example of the Maximum Horizontal Stress Redistribution around the Hydraulic Fracture in 3-D (1/8 of the Stress Field Regime).
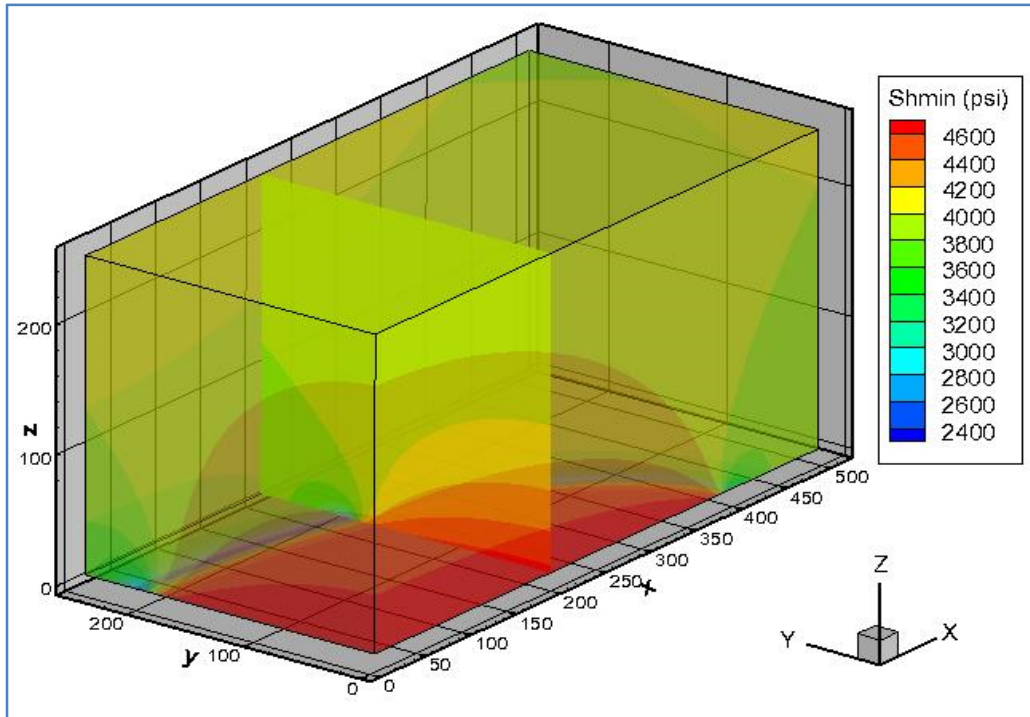
Fig. 4.5 Example of the Minimum Horizontal Stress Redistribution around the Hydraulic
Fracture in 3-D (1/8 of the Stress Field Regime).
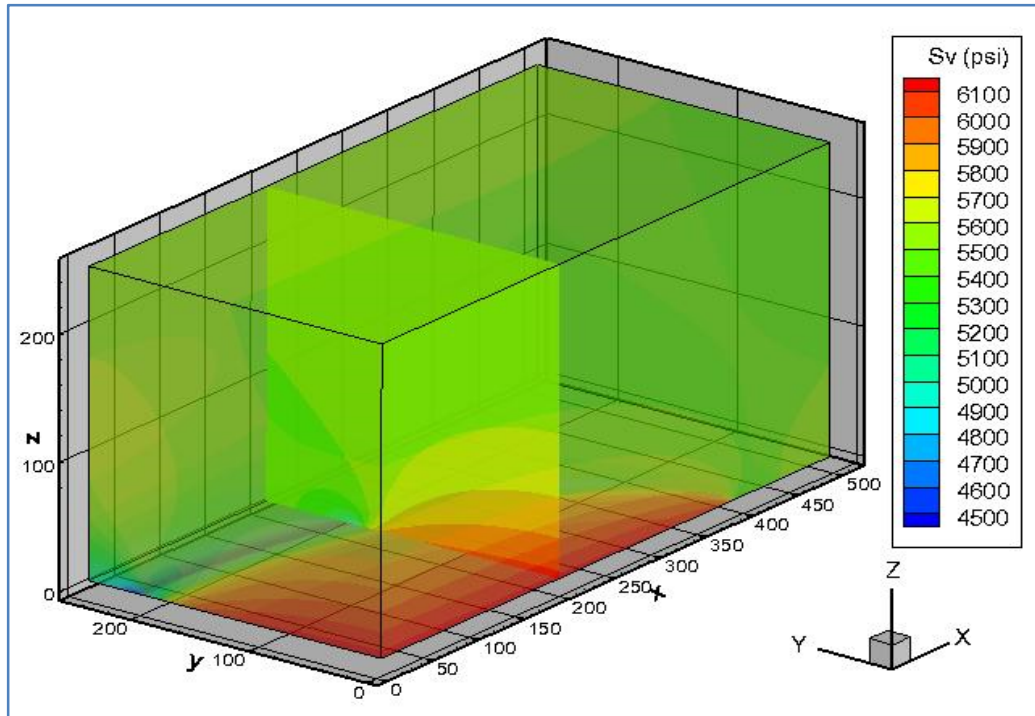
Fig. 4.6 Example of the Vertical Stress Redistribution around the Hydraulic Fracture in 3-
D (1/8 of the Stress Field Regime).

CHAPTER V

HYDRAULIC FRACTURE INTERACTION WITH NATURAL FRACTURES

In previous chapter, we have investigated the distributions of pore pressure and stresses around a hydraulically induced fracture. In the following, shear slip or failure along planes of weakness of natural fractures caused by pore pressure and stresses redistribution during injection of fluid is investigated. Knowledge of in-situ stress, and strength for the planes of weakness, is needed to predict potential failure area around the hydraulic fracture.

If the problem is simplified for certain sets of natural fractures, the additional pore pressure could be found with simple calculations. And for the formation with a certain set of natural fractures around a hydraulic fracture, the pore pressure changes are calculated, as well as the induced stress changes by the poroelasticity, thermoelasticiy, and fracture compression. The failure potential area for the existing set of natural fractures could be plotted near the fracture surface.

The failure of rock mass around the fracture is also studied to roughly predict the failure distance from the central fracture surface. It may have significant impact on permeability around a hydraulic fracture, and therefore on production. This in conjunction with the microseismic cloud is used to estimate the stimulated volume and the resulting rock mass permeability (Palmer et al., 2005; Palmer et al., 2007). The injected permeability is greater than the virgin permeability, and this is interpreted as enhanced permeability due to shear

or tensile failure away from the central fracture plane. In our model, the initial permeability and the fracturing geometry are given to simulate the in-situ stress variations and predict the failure zone.

It is generally accepted that the microseismicity during hydraulic fracturing operations are from the reactivation of natural fracture in the reservoir. The reactivation of natural fractures due to the potential risk of failure is analyzed by considering the fractures' orientations, the strength for the fracture planes, and the in-situ stress conditions. Different natural fractures can be theoretically expected for different slip regimes. This has been discussed a lot in previous studies (Ge, 2009, Ge and Ghassemi, 2011, 2012, 2014).

5.1 Mohr-Coulomb Failure Criterion

In this study, to investigate failure of natural fractures around a hydraulic fracture, the Mohr-Coulomb failure criterion is used (Warpinski et al., 2004):

$$|\tau| = \tau_s + \sigma_n' \tan\varphi' \tag{5.1}$$

Where τ is the shear stress, τ_s is the shear strength or cohesive strength, σ_n' is the effective normal stress and φ' is the joint friction angle.

In equation 5.1, the effective normal stress and shear stress on the planes of weakness are given by Jaeger and Cook (1979) as the following:

$$\sigma_n' = l^2\sigma_1 + m^2\sigma_2 + n^2\sigma_3$$
$$\tau = \sqrt{l^2 m^2 (\sigma_1 - \sigma_2)^2 + n^2 m^2 (\sigma_3 - \sigma_2)^2 + l^2 n^2 (\sigma_3 - \sigma_1)^2}$$
(5.2)

In which, l, m, and n are direction cosines for a given plane to the direction of the three

principal stresses, which can be expressed by [7, 23]:

$$d_H = \cos(90 - \delta) \times \cos(90 - \varphi)$$
$$d_h = \cos(90 - \delta) \times \sin(90 - \varphi)$$
$$d_v = \sin(90 - \delta)$$
(5.3)

In which, d_H, d_h, and d_v are direction cosines for the given plane to the direction of the three

stresses σ_H, σ_h and σ_v. δ is the dip angle and φ is the dip direction angle. If we simplify

the model by assuming the original three in-situ stresses σ_H, σ_h and σ_v are corresponding

to the three principal stresses, their direction cosines d_H, d_h, and d_v will also be

corresponding to the three direction cosines for a given plane to the direction of the three

principal stresses.

5.2 Structural Permeability Diagram

With the failure criterion and the orientations of natural fractures, a slip map can be

constructed to decide the required additional pore pressure for the reactivation of natural

fractures in any point around the hydraulic fracture in the reservoirs due to the shear effects

from the pore pressure increase.

An example plot is shown in Fig.5.1 for the slip map of joints in a shale reservoir (Ge and

Ghassemi, 2011). The circles in the plot represent the dip angle of joints (0°-90°), and the radial dashed lines represent the dip direction angles (0°-360°). The additional pressure required to reactivate the existing faults or natural fractures depends on not only the pore pressure and stress regime, but also the orientations of the fractures.
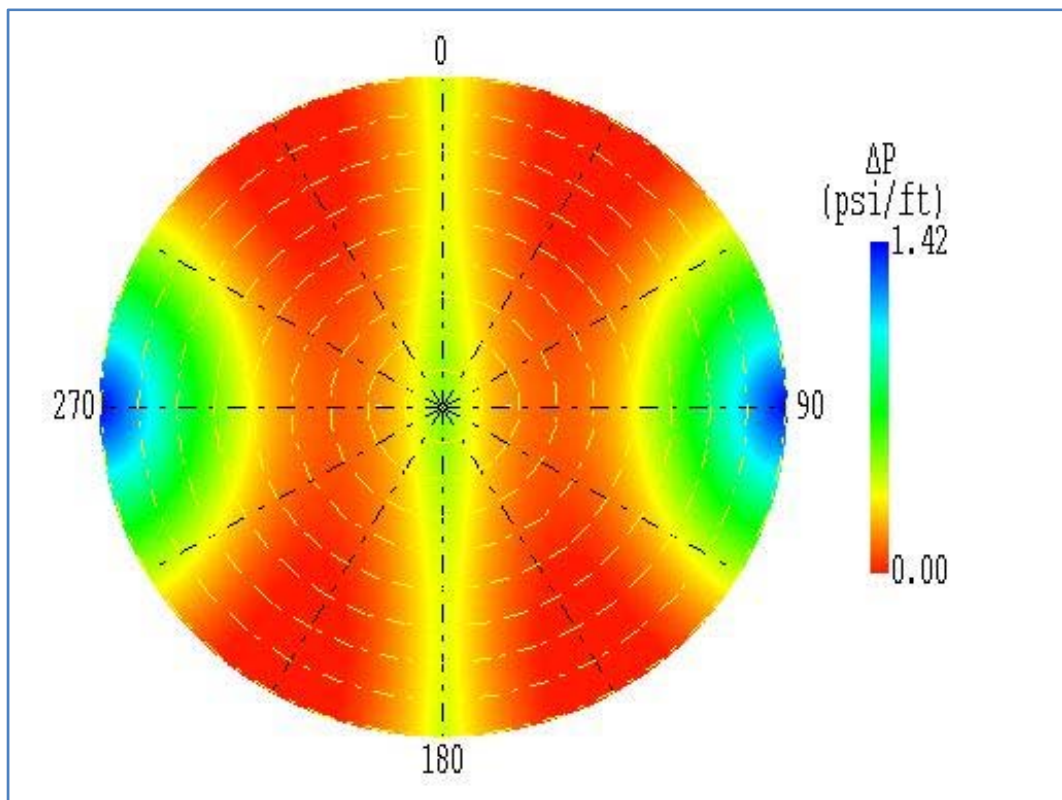
Fig.5.1. Example Plot Showing the Required Additional Pore Pressure for Shear Failure.

In previous study (Ge, 2009), a program in the FracJStim model for plotting the structural permeability diagram was constructed. The more detailed construction process of the structural permeability diagram is in Appendix B. In this section, we will compare some of our results with previous works and will apply the structural permeability diagram to some shale reservoirs in next chapter.

We simulated the data of Otway Basin on the southern Australian passive margin given by Mildren et al., 2005 (Table 5.1). The structural permeability maps are shown in Fig.5.2 and Fig.5.3. Minor difference on maximum required treating pressure can be attributed to uncertainty in the input data used. From the Fig.5.2 and Fig.5.3, there are perfect agreement in plot shapes and values, which verified our program for the structural permeability diagram.

Table 5.1 Otway Basin Data from Mildren et al. (2005)

Parameter	Value	Unit
Depth (D):	2.845	km
Minimum horizontal stress (S_h) gradient:	16.1	MPa/km
Maximum horizontal stress (S_H) gradient:	37.1	MPa/km
Vertical Stress (S_v) gradient:	22.4	MPa/km
Initial reservoir pressure (P_o) gradient:	9.8	MPa/km
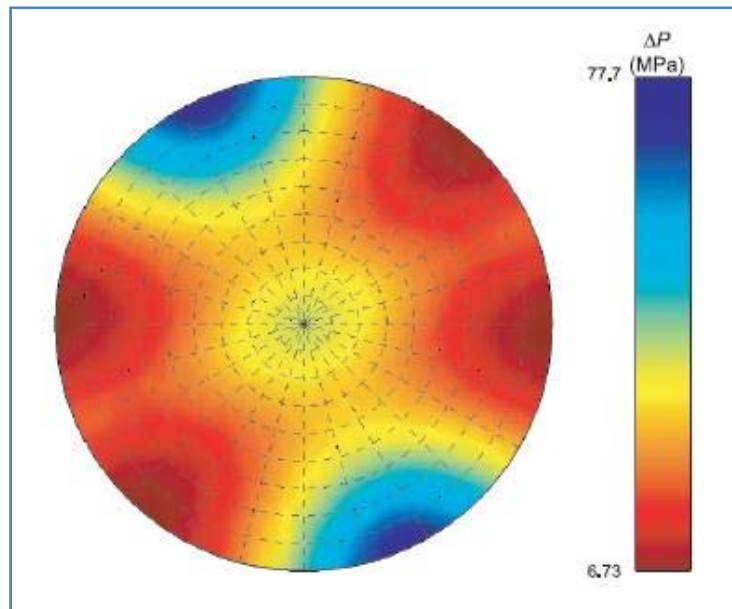
Fig.5.2 Structural Permeability Diagram for Otway Basin (Mildren et al. 2005).
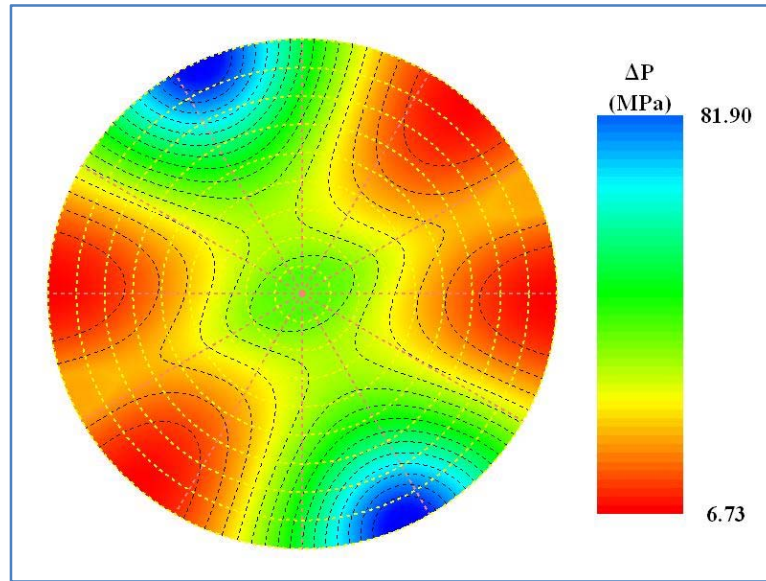
Fig.5.3 Structural Permeability Diagram for Otway Basin (Ge, 2009).

5.3 Stimulated Reservoir Volume

From previous description, we know that the elliptically distributed pore pressure is decreasing from the fracture surface to the far field. The position where the pore pressure and stress changes are too small to reactivate the joints marks the boundary of the failure zone the treating pressure can create.

If we assume the failed distance is uniform along the fracture height, therefore, we can estimate the failed reservoir volume as shown Fig.5.4 and Fig.5.5 (Ge and Ghassemi, 2012):

$$FRV = \pi y_d x_d h \qquad (5.4)$$

Where y_d is the failed distance, and x_d is the failed distance in X direction, and h is assumed equal to the fracture height H_f.
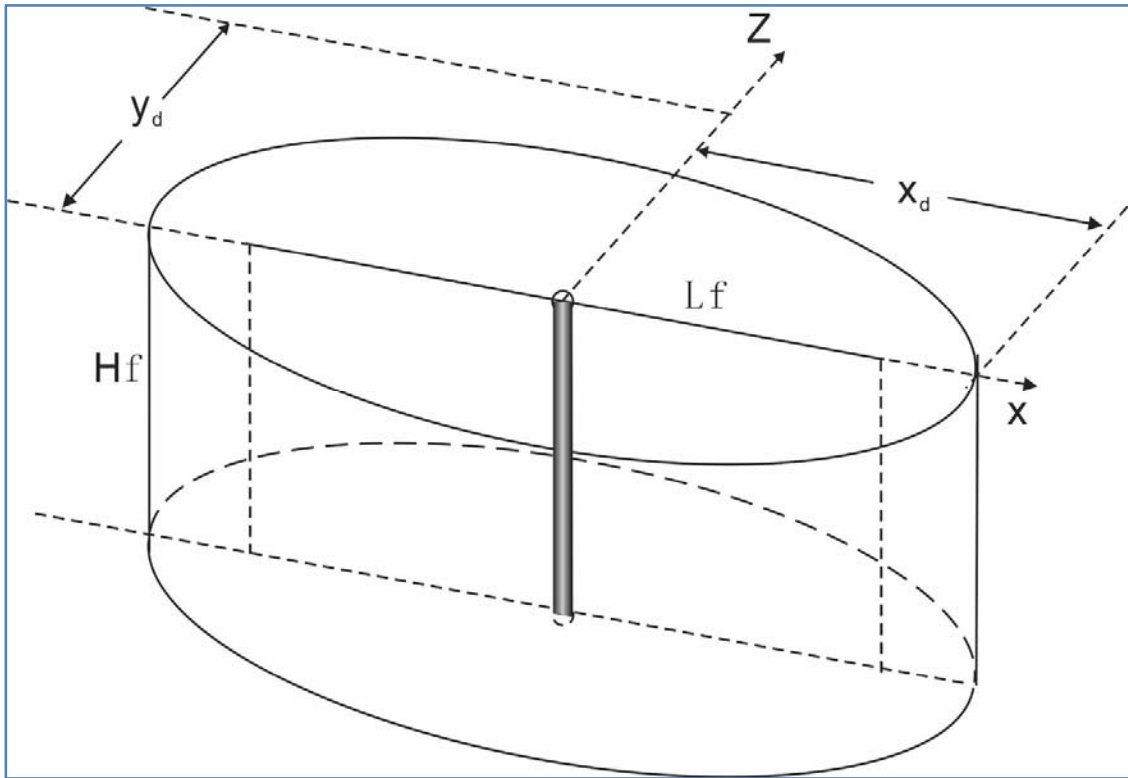
Fig.5.4 Failed Reservoir Volume from Vertical Well (Ge and Ghassemi, 2012).
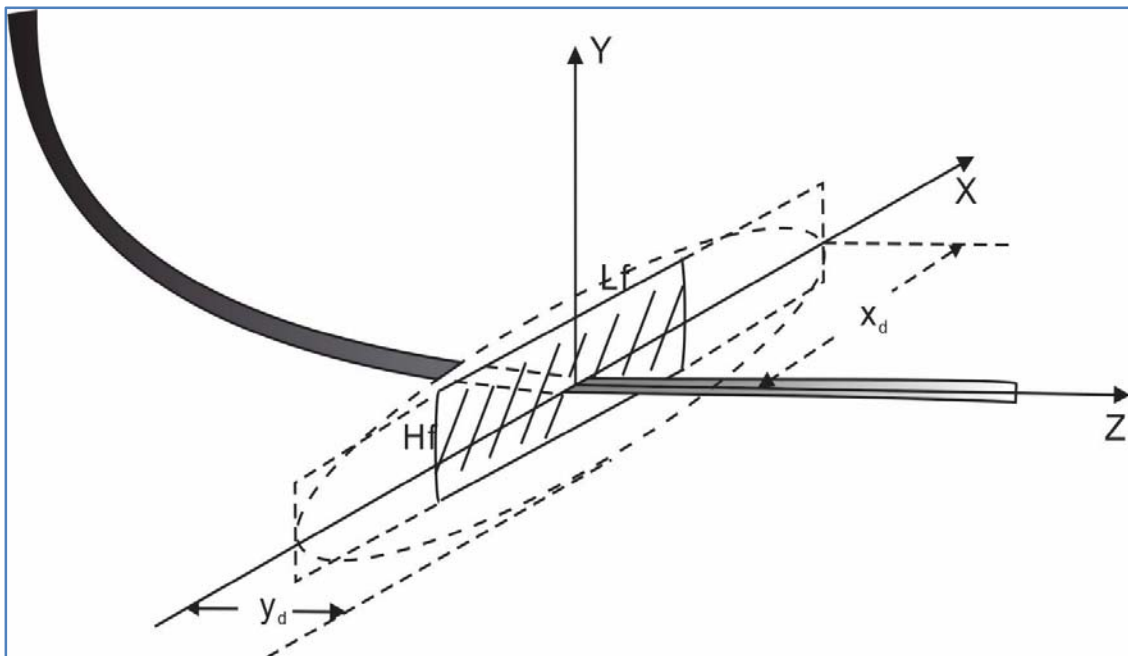
Fig.5.5 Failed Reservoir Volume from Horizontal Well (Ge and Ghassemi, 2012).

5.4 Enhanced Permeability

According to previous work by Palmer et al. (2005), the permeability enhancement during

a fracture treatment is mainly due to the coupled process between the pressure transient

and permeability increase. The pressure is transmitted along the natural fractures from the

central fracture surface, and this increased pore pressure will cause the shear failure of the

natural fractures and thus stimulates the permeability enhancement. Then, with higher

permeability in the reservoir, the pressure will be transmitted faster and further away from

the hydraulic fracture surface. Therefore, with the pore pressure distribution, and the

required additional pore pressure for joint reactivation, the failed distance could be

estimated. And using the assumed geometry for failed region, the failed reservoir volume

is calculated.
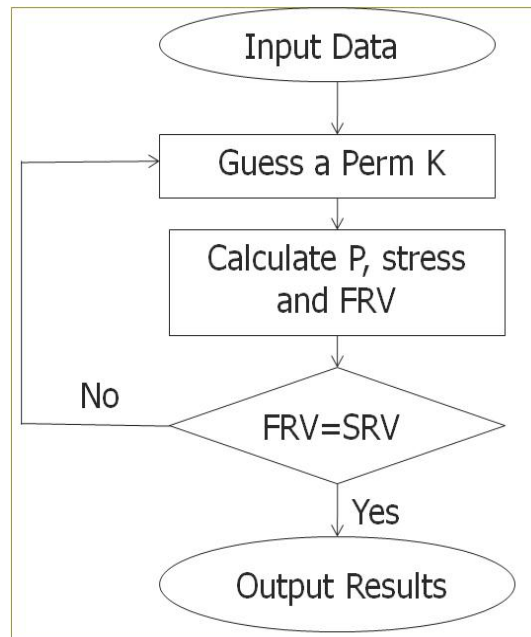
Fig.5.6 Flow Chart for the Estimation of Permeability Enhancement

A trial-and-error procedure is employed to predict the permeability enhancement in the failed region around the hydraulic fracture as shown in the flow chart in Fig.5.6 (Palmer, 2007; Ge, 2009; Ge and Ghassemi, 2012).

This procedure can be described as (Ge, 2009):

- Guess an injection/enhanced permeability.

- For a selected net fracture pressure, find the pore pressure distribution and stress variations, construct the slip map to find the required additional pore pressure for the joint reactivation.

- Estimate the failed distance and failed reservoir volume.

- By matching the failed reservoir volume with the stimulated reservoir volume (from microseismic clouds), the enhanced permeability is estimated.

CHAPTER VI

CASE STUDIES

To verify the constructed model in this study, several examples are given as case studies to investigate the pore pressure and stress redistribution around a hydraulic fracture, as well as the stimulated reservoir volume and the enhanced permeability, depending on the available data. The fracture and waterflooding dimensions are based on the fracture propagation model as described in previous chapters, and the examples for the model could be found in the thesis by Ge (2009).

In this chapter, the case studies will focus on the waterflooding hydraulic fracturing model to demonstrate the stress variations by the poroelasticity, thermoelasticity, and fracture compression. Moreover, with the natural fractures information of the reservoir, the treating pressure required to reactivate these pre-existing weakness planes will be estimated. If the microseismic data are available, the stimulated reservoir volume and enhanced permeability by the hydraulic fracturing operation could also be investigated.

6.1 Well Stimulation in Barnett Shale

A case study on Barnett Shale gas reservoir with our model is in the following. To compare with the previous work, we use the data from Palmer et al. (2007) for Barnett shale, as shown in Table 6.1.

In addition, according to previous study (Ge and Ghassemi, 2012), two sets of natural

fractures are employed here, including a north-south–trending set and a dominant, younger,

west-northwest–east-southeast– trending set. And the in-situ stress is assumed with S_{Hmax}

treading northeast-southwest (Ge and Ghassemi, 2012).

Table 6.1 Input Parameters from Barnett Shale Case

Parameter	Value	Unit
Depth (D):	8200	ft
Minimum horizontal stress (S_h):	5658	psi
Maximum horizontal stress (S_H):	6286	psi
Vertical Stress (S_v):	8200	psi
Initial reservoir pressure (P_o):	4100	psi
Friction angle (ϕ'):	31	degree
Cohesion (c):	100	psi
Modulus (E):	3.00E+06	psi
Porosity:	0.1	
Poisson's ratio:	0.25	
Bulk compressibility (c_t):	3.69E-06	1/psi
Water viscosity at res. temp.	0.3	cp
Fracture half height (H_f):	200	ft
Fracture half length (X_f):	1000	ft
Pumping time (T):	5	hour
Fracturing net pressure (P_f):	100-900	psi
Fracturing rate (Q_0):	70	bpm
Fracture fluid volume (V):	800,000-1,000,000	gal

Using the parameters for Barnett Shale in Table 6.1, we plot the pore pressure distribution

for this case study. Fig.6.1 shows us the pore pressure distribution around the fracture

center plane in Barnett Shale at water flooding time t=9 hours. The maximum pore pressure

lies around the fracture surface, with a value of 6558 psi. The pore pressure is elliptically

distributed around the fracture surface and is decreasing from the central fracture to the

reservoir formation (Ge, 2009; Ge and Ghassemi, 2011, 2012).
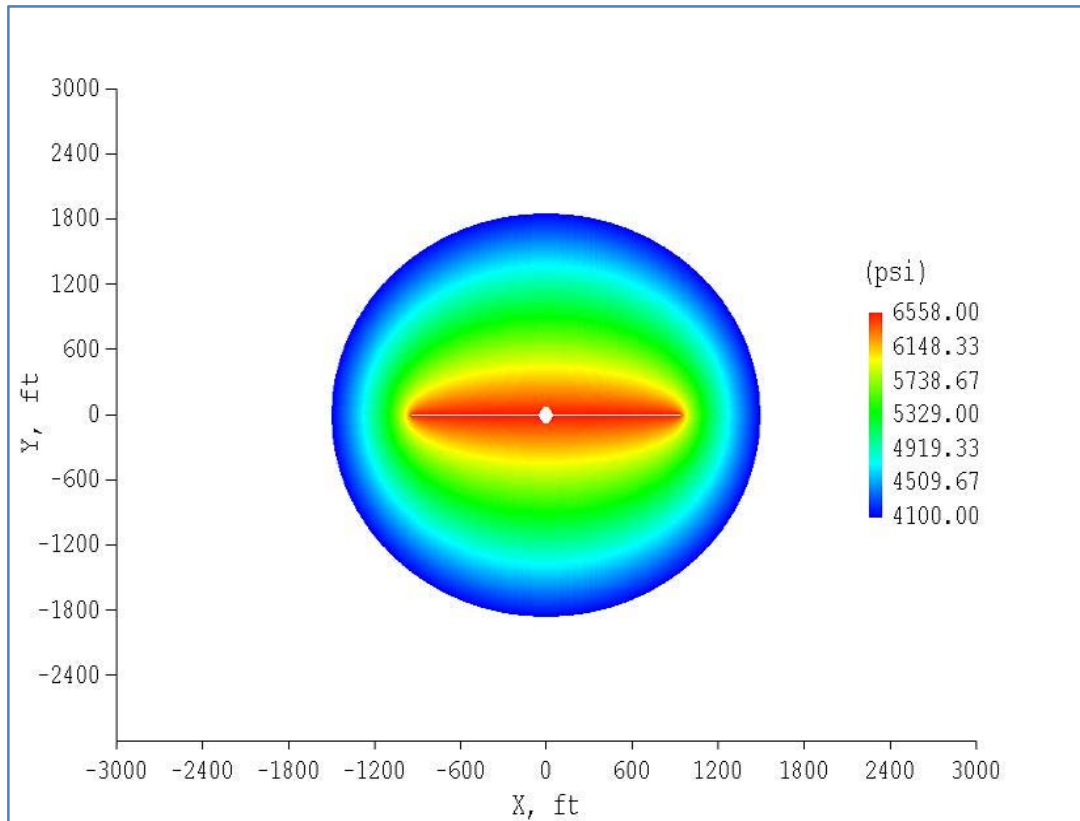
Fig.6.1 Pore Pressure Distribution around Fracture (t=9 hours for Barnett Shale).

The required effective treating pressure to reactivate fabrics of different orientations of

joints in the reservoir of Barnett Shale is shown in Fig.6.2 (Parameters are from Table 6.1).

In Fig.6.2, if we assume there are enough joints in the formation around the hydraulic

fracture, the required effective treating pore pressure to stimulate the joints shouldn't be

less than 0.06 psi/ft.
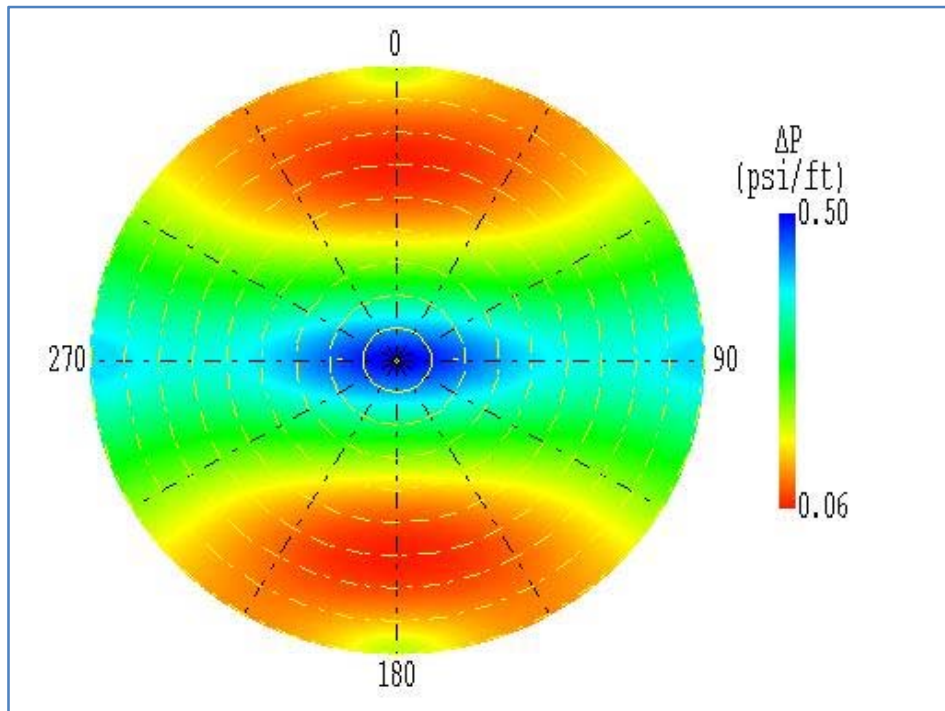
Fig.6.2 Slip Map Showing the Required Additional Pore Pressure for the Natural Fractures Reactivation in Barnett Shale.

With the pore pressure distribution and the slip map for Barnett Shale, the failed distance and the failed reservoir volume are calculated. The failed reservoir volume is then matched with the stimulated reservoir volume that estimated from the microseismic cloud to adjust the enhanced permeability and failed distance.

The stimulated reservoir volume in this case study is calibrated from the trendlines for the stimulated reservoir volume vs. net fracture pressure (Palmer, et al., 2007).
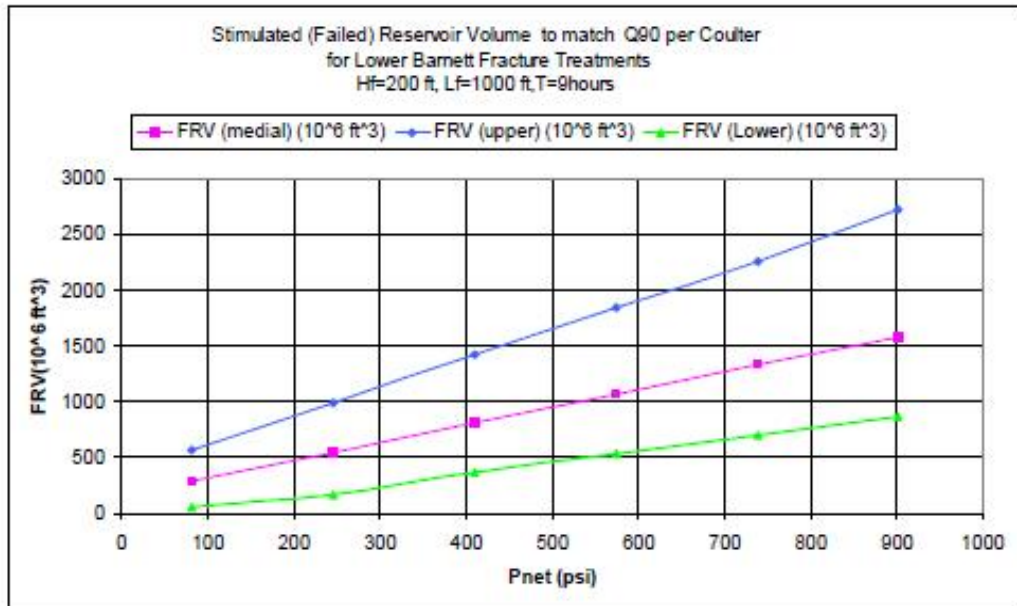
Fig.6.3 Trendlines for Stimulated Reservoir Volume (FRV=SRV) vs Net Fracture Pressure (Palmer, et al., 2007).
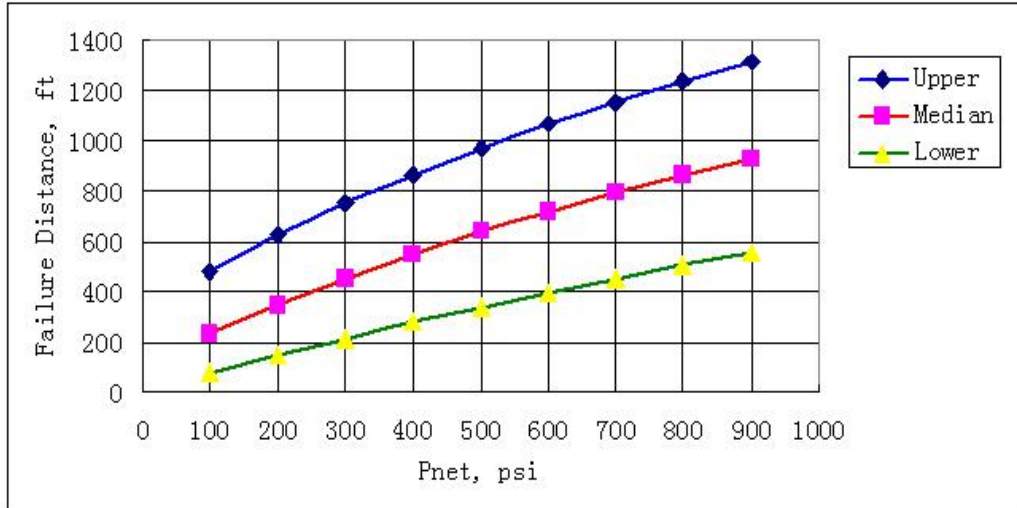
Fig.6.4 Estimated Failed Distance Normal to the Fracture Surface.

67
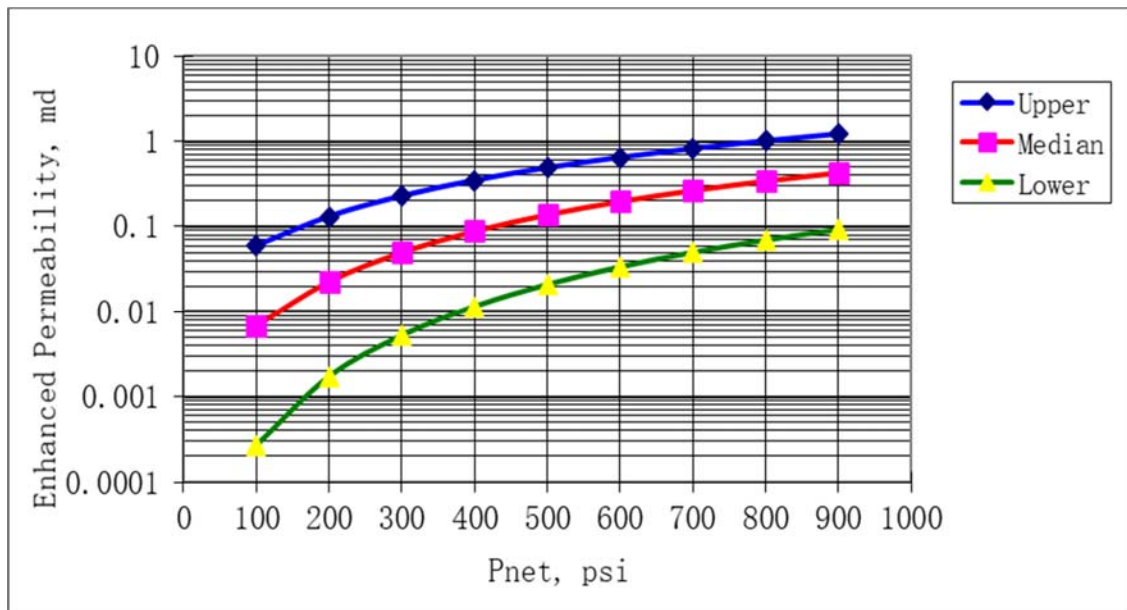
Fig.6.5 Matched Enhanced Permeability for Barnett Shale.

After matching the calculated reservoir volume with the stimulated reservoir volume at any selected net fracture pressure (from 0 to 900 psi for this study), the failed distance normal to the fracture surface is plotted in Fig.6.4. And the matched enhanced permeability is also plotted as a function of net fracture pressure in Fig.6.5.

To validate our results and model, we compare the enhanced permeability in our model with the results from previous study (Palmer, et al., 2007). By comparing, the enhanced permeability in this study is close to the results from previous work. The permeabilities are found to be increased 1-2000 times (as shown in Fig.6.6) of the original permeability of the Barnett Shale.
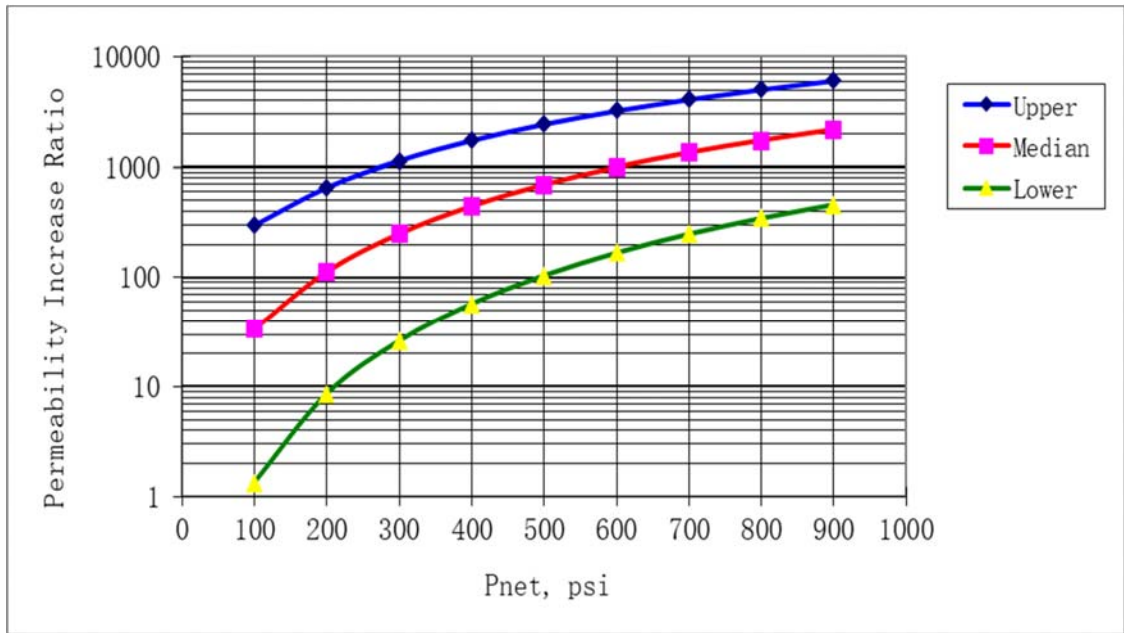
Fig.6.6 Permeability Enhancement Ratio (k/ki) during Injection to Barnett Shale Fracture Treatments.

6.2 Hydraulic Fracturing in Bakken Shale

For most unconventional reservoirs, the reservoir permeability is very small. For example, the permeability of Bakken is mostly less than 0.1 md (Kurtoglu, 2013). Even with the consideration of fracture permeability, it is still very low. Of course, after the stimulation by hydraulic fracturing, the permeability could be enhanced as previously studied (Ge and Ghassemi, 2011). So, this case study was performed representing a typical hydraulic fracturing in the horizontal well of a shale reservoir. The used parameters are shown in Table 6.2.

Table 6.2. Input Parameters for Bakken Shale

Parameter	Value	Unit
Minimum horizontal stress (Sh):	7000	psi
Maximum horizontal stress (SH):	7500	psi
Vertical stress (Sv):	10000	psi
Initial reservoir pressure (Po):	4400	psi
Fracturing net pressure (Pf):	800	psi
Coefficient of friction:	0.6	
Cohesion (c):	100	psi
Shear Strength:	1	psi
Modulus (E):	5.00E+06	psi
Poisson's ratio:	0.3	
Porosity:	0.15	
Effective Permeability:	4	md
Biot's modulus:	1	
Fluid compressibility (ct):	3.30E-06	1/psi
Fluid viscosity:	0.3	cp
Fracture half height (Hf):	50	ft
Fracture half length (Xf):	1000	ft
Elapsed leakoff time (t):	10	hour
Coefficient of thermal expansion (β):	3.10E-06	1/ºF
Temperature difference (ΔT):	150	ºF

The pore pressure and stresses redistribution of this case are shown in Fig.6.7-6.10. The figures of the stresses redistribution around the hydraulic fracture have shown the new stress regime after a certain time of fracturing operation. In this case, the required treating pressure for the reactivation of existing faults or natural fractures in the reservoir is plotted in the slip map. In this case, from the Fig.6.11, the minimum required treating pressure to reactivate the fault is 1180 psi, which is larger than the assumed treating pressure. That means, there is less likely that natural fractures will be reactivated during this treatment, unless higher treating pressure is operated in the field.

Fig.6.7 3-D Pore Pressure Distribution around a Hydraulic Fracture (1/8 part of the whole region) for Bakken Case.

Fig.6.8 Maximum Horizontal Stress Redistributions around the Hydraulic Fracture in 3-D (1/8 of the Stress Field Regime) for Bakken Case.

Fig. 6.9 Minimum Horizontal Stress Redistributions around the Hydraulic Fracture in 3-D (1/8 of the Stress Field Regime) for Bakken Case.

Fig. 6.10 Vertical Stress Redistributions around the Hydraulic Fracture in 3-D (1/8 of the Stress Field Regime) for Bakken Case.

72
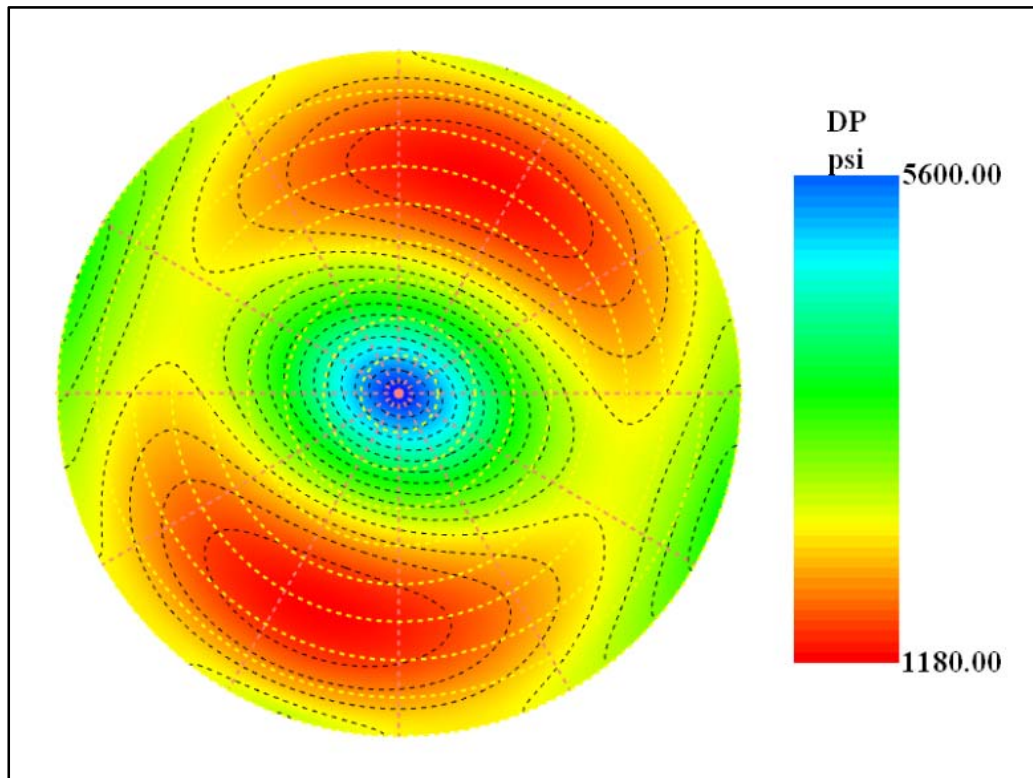
Fig. 6.11 Required Treating Pressure for the Reactivation of Natural Fractures for Bakken Case.

If there is one set of natural fractures in the NNE-SSW directions with a dip angle 50º to 70º, the required treating pressure for reactivation of these natural fractures would be around 1200 psi. This analysis would be helpful to instruct the field hydraulic fracturing operations for the optimal drilling process.

6.3 Case Study on Enhanced Geothermal System

In the following, we have performed another case study with our proposed model. The parameters used for a case representing an Enhanced Geothermal Reservoir are shown in Table 6.3.

Similarly, the pore pressure distribution of this case is shown in Fig.6.12. From this plot, the pore pressure is decreasing outward elliptically from the fracture surface to the reservoir pressure in the far field.

Table 6.3 Input Parameters for Enhanced Geothermal Reservoir

Parameter	Value	Unit
Minimum horizontal stress (Sh):	4000	psi
Maximum horizontal stress (SH):	4800	psi
Vertical stress (Sv):	5500	psi
Initial reservoir pressure (Po):	2500	psi
Fracturing net pressure (Pf):	800	psi
Coefficient of friction:	0.6	
Cohesion (c):	100	psi
Shear Strength:	5	psi
Modulus (E):	4.00E+06	psi
Poisson's ratio:	0.2	
Porosity:	0.15	
Effective Permeability:	100	md
Biot's modulus:	0.99	
Fluid compressibility (ct):	3.30E-06	1/psi
Fluid viscosity:	1	cp
Fracture half height (Hf):	200	ft
Fracture half length (Xf):	400	ft
Elapsed leakoff time (t):	1	hour
Coefficient of thermal expansion (β):	3.10E-06	1/ºF
Temperature difference (ΔT):	210	ºF

Fig. 6.13-6.15 show the 3-D stress redistributions around the hydraulic fracture. For the convenience of visualization, only 1/8 region around the hydraulic fracture is plotted in each stress regime. Hydraulic fracturing is propagating in the x direction (maximum horizontal stress direction) and opens against to the z direction (the minimum horizontal stress direction, as shown in Fig. A-1). The y-axis is in the vertical direction in this case
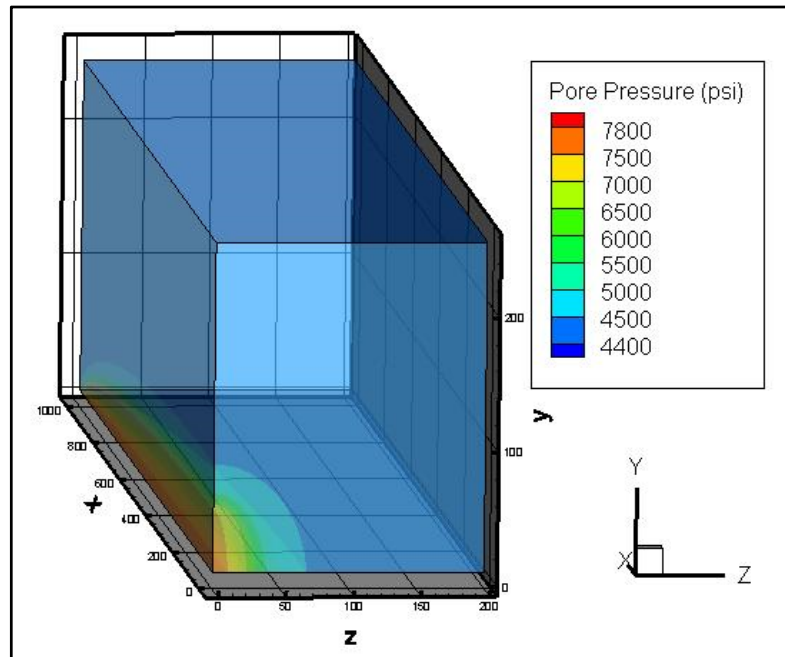
study.
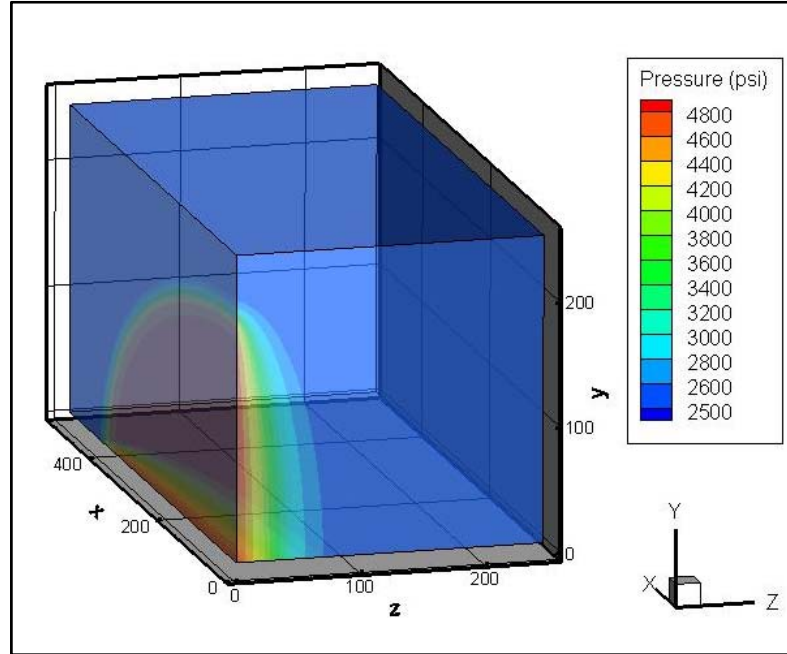
Fig.6.12 3-D Pore Pressure Distribution around a Hydraulic Fracture (1/8 part of the whole region) for EGS Case.
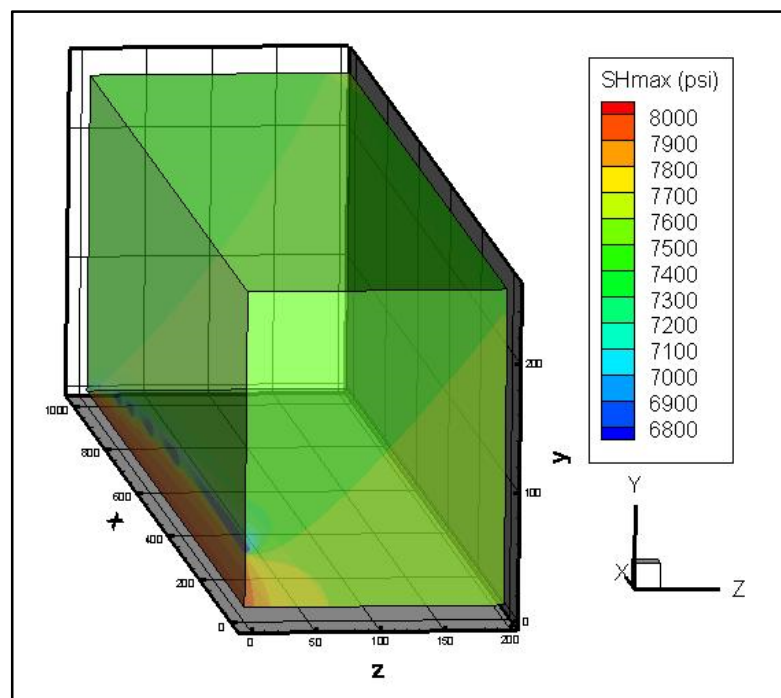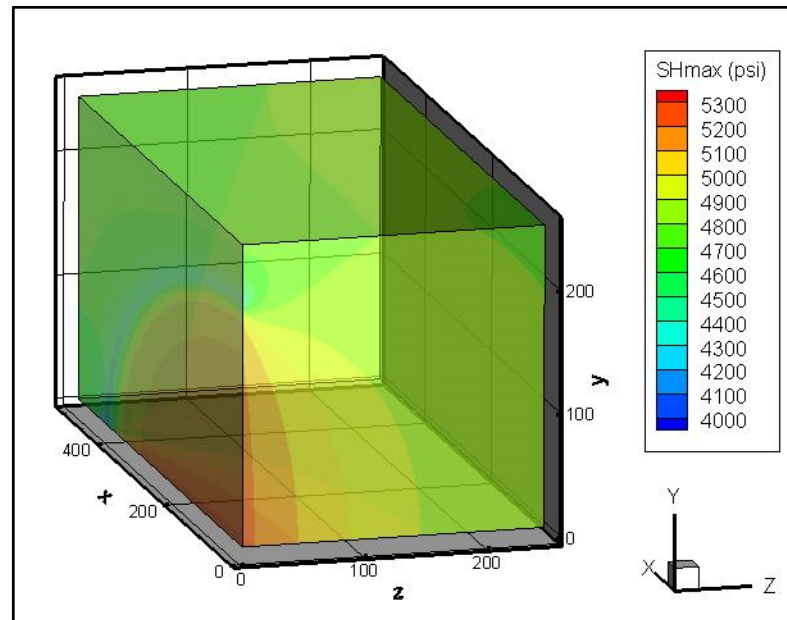

Fig.6.13 Maximum Horizontal Stress Redistributions around the Hydraulic Fracture in 3-D (1/8 of the Stress Field Regime) for EGS Case.

75
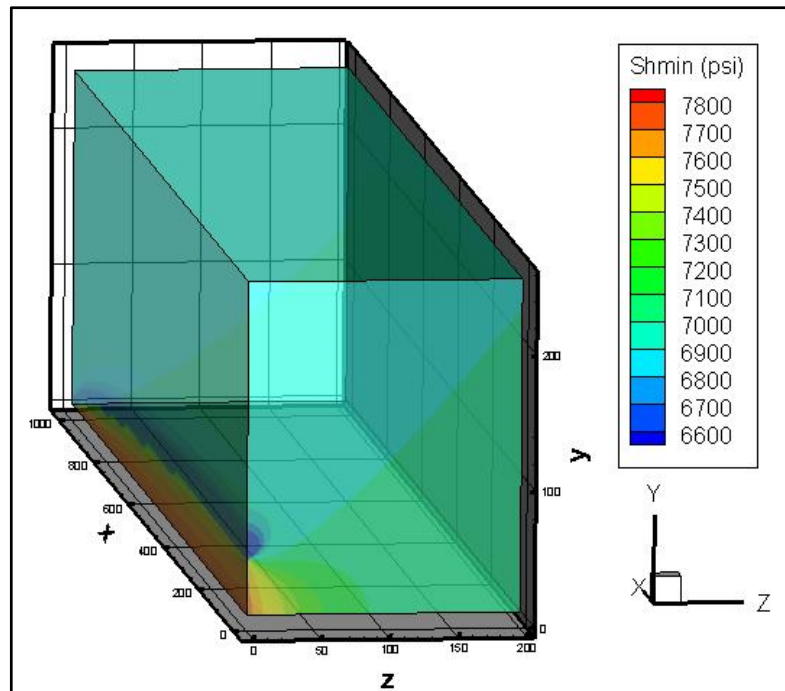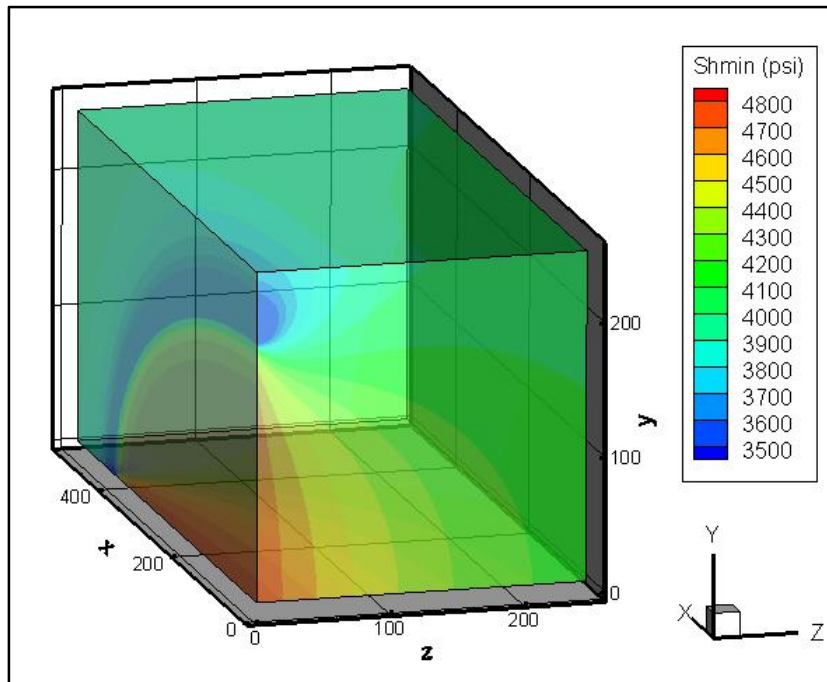
Fig.6.14 Minimum Horizontal Stress Redistributions around the Hydraulic Fracture in 3-D (1/8 of the Stress Field Regime) for EGS Case.
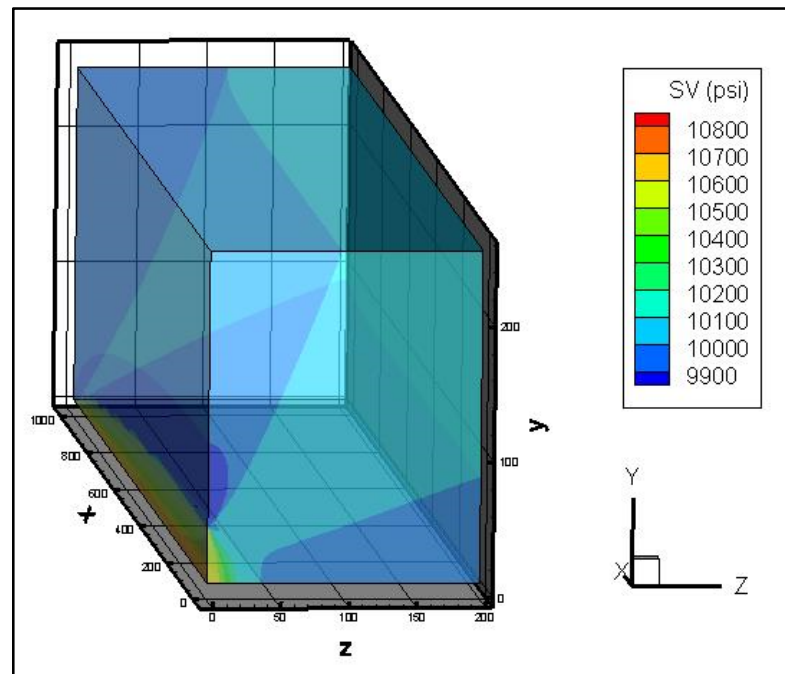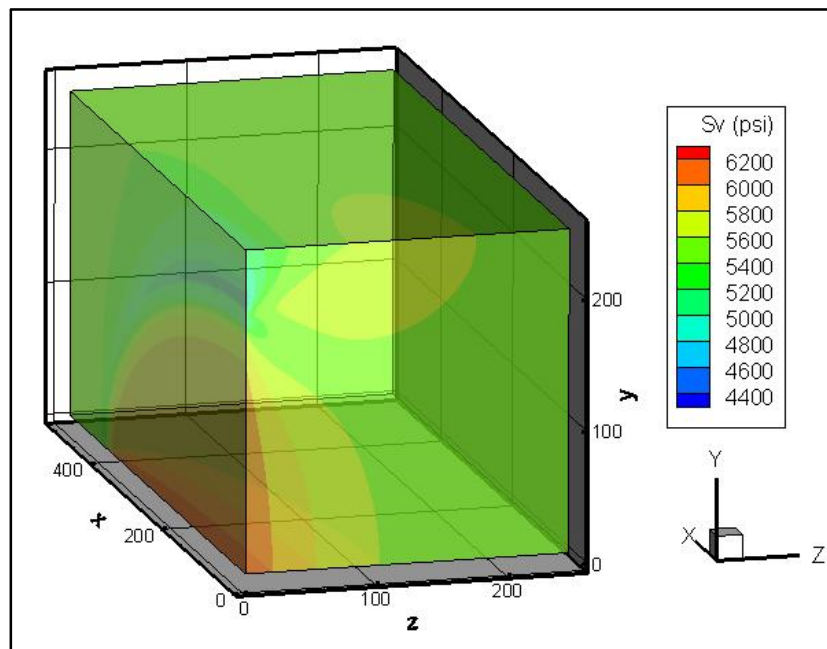

Fig.6.15 Vertical Stress Redistributions around the Hydraulic Fracture in 3-D (1/8 of the Stress Field Regime) for EGS Case.

With the failure criterion and the orientations of natural fractures, a slip map is constructed to decide the required additional pore pressure for the reactivation of existing weakness planes (including faults, natural fractures and joints). Fig.6.16 shows the required treating pressure for the geothermal reservoir. From this figure, if we assume there are enough joints in the formation around the hydraulic fracture, the effective treating pressures required for reactivating the rock joints are from 792 psi to 3000 psi, depending on the locations and orientations of the natural fractures. The proposed treating pressure as shown in table 6.3 can only reactivate certain natural fractures with orientations in the NNW-SSE direction and high dip angle around 50º-80º (as shown in Fig.6.16).
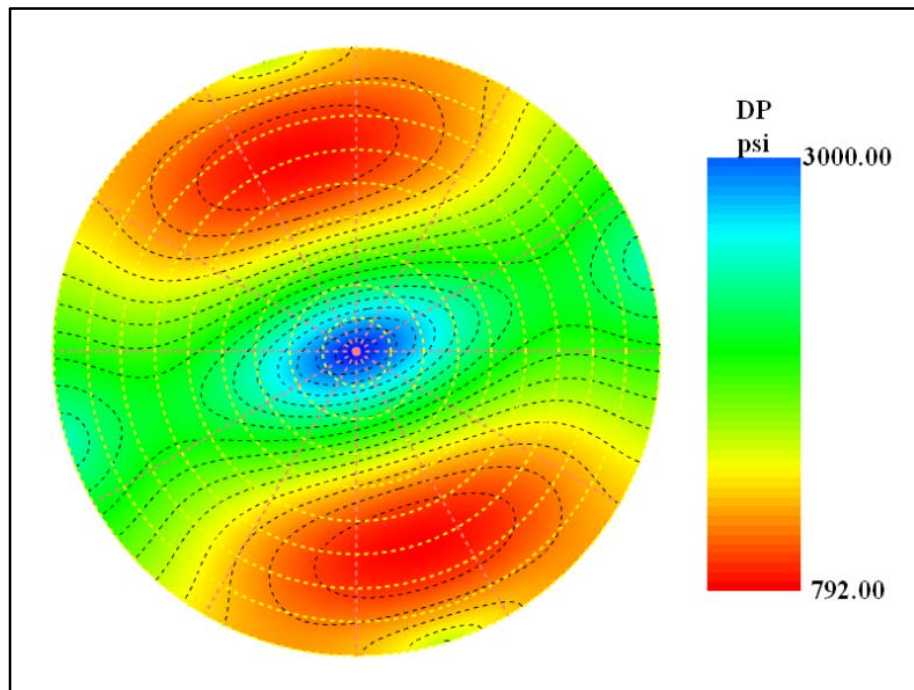
Fig. 6.16 Required Additional Pore Pressure for the Reactivation of Natural Fractures for EGS Case.

CHAPTER VII

SUMMARY, CONCLUSIONS AND DISCUSSIONS

The success of the hydraulic fracturing operations in unconventional reservoirs relies on the accurate understanding of the reservoir and rock mechanical properties. The pore pressure and stress variations in the reservoir during the hydraulic fracturing process are among the most important factors that affect the accuracy of a hydraulic fracturing model. As a necessary verification of more complex numerical modeling and simulations, and a quick support in the field operations, the more straightforward semi-analytical model is necessary.

In this study, we summarized and improved the fracture model by Ge and Ghassemi (2011, 2012, 2014) for hydraulically induced fracture in an infinite unconventional reservoir by using more accurate 3-D pore pressure and stresses analysis. And this study also investigated the potential reactivations of the existing faults or natural fractures in the reservoir, which can be used to estimate the stimulated reservoir volume from the response of the reservoir rock in the vicinity of the main fracture with reference to rock failure and permeability variation. The response of the rock mass to the variations of pore pressure and stresses is calculated by considering the joint orientations and frictional properties, as well as a rock mass failure criterion. And several case studies were performed to verify this model.

From the simulation results of the case studies, we can have the idea on how the pore pressure and stresses are redistributed after the hydraulic fracturing operation. The shape of the hydraulic fracture, the permeability of the reservoir, the rock mechanical properties, and the original stress anisotropy, all can affect the redistributions of the stress regime.

Both cases show that stresses, including the horizontal stresses and the vertical stress, have decreased at the fracture tip and increased on the fracture surface. The induced stresses in the minimum horizontal stress direction are larger than the induced stresses in the maximum horizontal stress direction; however, the new minimum horizontal stresses are still less than the maximum horizontal stresses. This indicates that a stress reversal does not happen in these cases. Further studies could be performed to find out the conditions for stress reversal near the fracture surface area by assuming that the original stress anisotropy is small enough.

This work is of interest in interpretation of the induced micro-seismicity in the hydraulic fracturing operations and in assessing permeability enhancement by the stimulation. With further modifications, this model can also be used to optimize the drilling and injection activities for stimulation in unconventional shale oil and gas reservoirs. By considering the stress redistribution and natural fractures distribution in the reservoir, this work will benefit the design of the re-fracturing operations in unconventional reservoirs.

7.1 Summary

In this research, the traditional two dimensional hydraulic fracturing propagation models are reviewed, the fracture propagation model was constructed to estimate the dimensions of the hydraulic fracture, the cooled region, and the waterflooded region. The 3-D pore pressure and stress redistributions around a hydraulically induced fracture are investigated, considering the effects from poroelasticity, thermoelasticity, and fracture compression.

The distributions of pore pressure and stresses around a fracture is of interest in conventional hydraulic fracturing, fracturing during water-flooding of petroleum reservoirs, and injection/extraction operation in a geothermal reservoir. The stress and pore pressure fields are affected by: poroelastic, thermoelastic phenomena as well as by fracture opening under the combined action of applied pressure and in-situ stress.

The methodology of Perkins and Gonzalez (1985) is used for calculating the fracture lengths, bottomhole pressures (BHP's), and elliptical shapes of the flood front as the injection process proceeds. The 3-D pore pressure distribution was estimated based on the linear flow approximation around 3-D flat elliptic crack (Warpinski, et al., 2004). The temperature distribution was originally considered uniform in the cooled region, and later updated in the 3-D flat crack.

A semi-analytical model has been set up to estimate both the 2-D and 3-D pore pressure and stress distribution around a hydraulic fracture. For the first time in this work, the

combination of the poroelastic, thermoelastic, and the fracture compression effects was studied. The model calculates the stress and pore pressure distribution around a fracture of a given length under the action of applied internal pressure and in-situ stresses as well as their variation due to cooling and pore pressure changes. It also calculates the failure potentials and slip map of natural fractures around the fracture based on the t Mohr-Coulomb failure criterion to estimate the additional pore pressure needed to reactivate the pre-existing natural fractures. Case studies were performed on natural fractured shale reservoirs. This is of interest in interpretation of micro-seismicity in hydraulic fracturing and in assessing permeability variation around a stimulation zone.

7.2 Conclusions

The following conclusions are drawn from this study.

1. Poroelasticity and thermoelasticity can cause some significant changes in the pore pressure and stress redistributions around a hydraulic fracture.

2. A hydraulic fracturing propagation model was developed for calculating the length of a water-flood induced fracture from a single well in an infinite reservoir.

3. A 3-D semi-analytical model was proposed to calculate the pore pressure and the stress changes at any point around the fracture caused by thermoelasticity, poroelasticity and fracture compression. The effect of the fracture opening on the stress redistribution could be analytically calculated by some assumptions.

4. By using the Mohr-Coulomb failure criterion, we can estimate the failure potentials of natural fractures and the required additional treating pressure to reactivate the natural fractures in shale reservoirs.

5. If we know the stimulated reservoir volume from the microseismic cloud, we can estimate the enhanced permeability by the stimulation of hydraulic fracturing operations.

6. The low permeability shale reservoirs with lots of natural fractures could be affected by the stress redistribution due to the interactions between the hydraulic fracture and the natural fractures.

7. This study can be applied to investigate the effects of hydraulic fracturing operations on the induced stress regime, pore pressure and permeability variations in natural fractured reservoirs.

8. It can be used to estimate the potential stress reversal during the hydraulic fracturing process due to the fracture opening and temperature change and assist the candidate well selection for refracturing operations.

9. It can also be used to simulate the stimulated reservoir volume and help in the interpretation of micro-seismicity induced by hydraulic fracturing.

10. The models may be used for assessing the more complexed numerical models and software package.

7.3 Recommendations

In this study, we only focused on the pore pressure and stress redistribution around one hydraulic fracture. Further work could be done to investigate the multiple hydraulic fractures based on this work.

The unconventional shale reservoirs have specific characterizations, such as the heterogeneity and vertical traverse isotropy, which could also be very interesting topics to study in the future.

It is worth collecting more data from shale reservoirs, specially from Bakken, and combine the model with the shale reservoir data to design hydraulic fracturing operations.

It will also be interesting to investigate the special conditions under which the magnitude of the two horizontal stresses could be reversed.

The equations and calculations in this study could also be incorporated into a more complex numerical model, if enough data and computational capability are available.

APPENDICES

APPENDIX A

DEDUCTIONS OF THE INDUCED 3-D STRESSES BY FRACTURE COMPRESSION

In this work, the 3-D fracture induced stresses are based on the work by Green and Sneddon's solution (1950) for a flat elliptic crack in a homogeneous, linear elastic material. Kassir and Sih (1966) extended their work to the three-dimensional stress distribution around an elliptical crack under arbitrary loadings. Warpinski et al. (2004) applied the fracture induced stress in their model for prediction of microseismicity. However, in all the previous work, the detailed deduction process and final expressions for induced stresses was not given clearly. So based on their work, we give detailed analysis and the deduction process in this work.
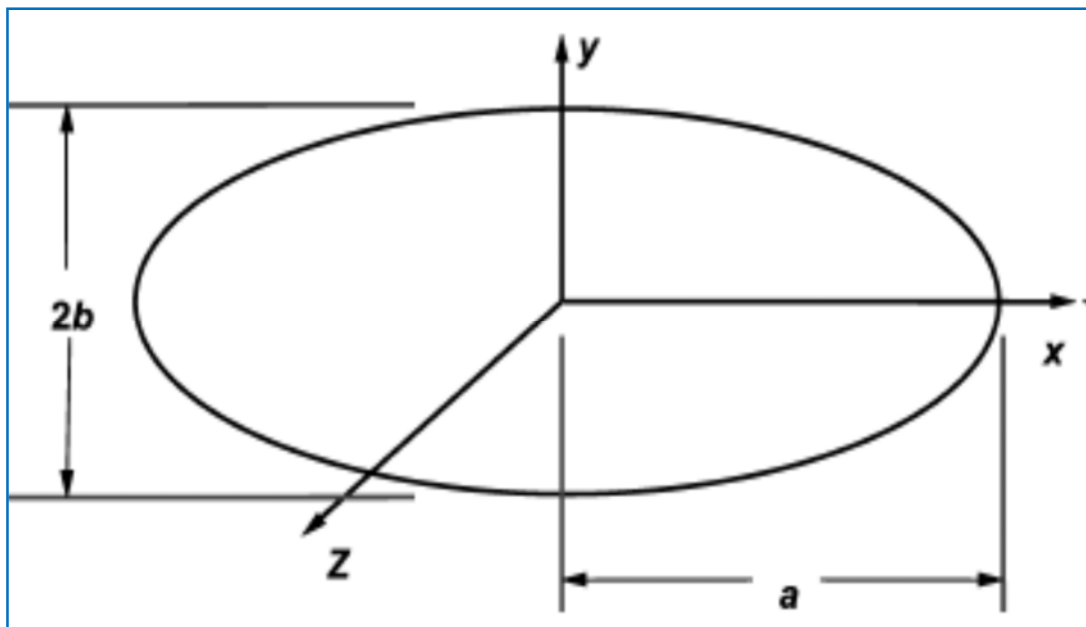
Fig.A.1 Geometric for Flat Elliptic Crack.

Given Conditions:

Green and Sneddon (1950) gave the solution for a constant pressure crack in a homogeneous material and the potential function is:

$$\Phi = \frac{ab^2(p_f - \sigma_{min})}{32G\ E(k)} \int_\lambda^\infty \left(\frac{x^2}{a^2 + s} + \frac{y^2}{b^2 + s} + \frac{Z^2}{s}\right.$$

$$\left. - 1\right) \frac{ds}{\sqrt{s(a^2 + s)(b^2 + s)}}$$

In which:

G is the shear modulus, p_f is the internal pressure, a is the fracture half length, b is the fracture half height. E(k) is the complete elliptic integral of the second kind, k is the modulus defined by:

$$k = \sqrt{a^2 - b^2}/a \qquad \text{(A. 1)}$$

The ellipsoidal coordinates are defined by:

$$a^2(a^2 - b^2)x^2 = (a^2 + \lambda)(a^2 + \mu)(a^2 + \varepsilon)$$

$$b^2(b^2 - a^2)y^2 = (b^2 + \lambda)(b^2 + \mu)(b^2 + \varepsilon) \qquad \text{(A. 2)}$$

$$a^2 b^2 Z^2 = \lambda\mu\varepsilon$$

Where:

86

$$\infty > \lambda \geq 0 \geq \mu \geq -b^2 \geq \varepsilon \geq -a^2 \tag{A. 3}$$

The coordinates x and y are within the crack plane, a complex variable z is defined as $x+iy$ and the axis normal to the crack surface is defined by the Z coordinate. Note not to confuse the Z coordinate and the complex variable z. $\bar{z}$ is the complex conjugate of z.

Expressions for stresses by the potential function: (Green & Sneddon, 1950; Sih & Liebowitz, 1968; Warpinski, et al. 2004)

$$\sigma_{xx} + \sigma_{yy} = -8G \left[(1 + 2v) \frac{\partial^2 \phi}{\partial Z^2} + Z \frac{\partial^3 \phi}{\partial Z^3} \right] \tag{A. 4}$$

$$\sigma_{xx} - \sigma_{yy} + 2 i \sigma_{xy} = 32G \frac{\partial}{\partial \bar{z}^2} \left[(1 - 2v)\phi + Z \frac{\partial \phi}{\partial Z} \right] \tag{A. 5}$$

$$\sigma_{zz} = -8G \left[\frac{\partial^2 \phi}{\partial Z^2} - Z \frac{\partial^3 \phi}{\partial Z^3} \right] \tag{A. 6}$$

$$\sigma_{xz} + i \sigma_{yz} = 16GZ \frac{\partial^3 \phi}{\partial \bar{z} \, \partial Z^2} \tag{A. 7}$$

Solving Expressions for each Stress Component by Potential Function (ϕ):

$$2\sigma_{xx} + 2 i \sigma_{xy} = -8G \left[(1 + 2v) \frac{\partial^2 \phi}{\partial Z^2} + Z \frac{\partial^3 \phi}{\partial Z^3} \right]$$
$$+ 32G \frac{\partial}{\partial \bar{z}^2} \left[(1 - 2v)\phi + Z \frac{\partial \phi}{\partial Z} \right] \tag{A. 8}$$

Now, we need to get the partial derivative to the conjugate of complex variable z:

$$\frac{\partial \phi}{\partial \bar{z}} = \frac{1}{2}\left(\frac{\partial \phi}{\partial x} + i \frac{\partial \phi}{\partial y}\right) \tag{A. 9}$$

$$\frac{\partial^2 \phi}{\partial \bar{z}^2} = \frac{1}{2}\left[\frac{1}{2}\frac{\partial}{\partial x}\left(\frac{\partial \phi}{\partial x} + i \frac{\partial \phi}{\partial y}\right) + i\frac{1}{2}\frac{\partial}{\partial y}\left(\frac{\partial \phi}{\partial x} + i \frac{\partial \phi}{\partial y}\right)\right]$$

$$= \frac{1}{4}\left[\left(\frac{\partial^2 \phi}{\partial x^2} - \frac{\partial^2 \phi}{\partial y^2}\right) + 2i\left(\frac{\partial^2 \phi}{\partial x \partial y}\right)\right] \tag{A. 10}$$

$$2\sigma_{xx} + 2\,i\,\sigma_{xy} = 8G\left\{-\left[(1+2v)\frac{\partial^2 \phi}{\partial Z^2} + Z\frac{\partial^3 \phi}{\partial Z^3}\right]\right.$$

$$+ \left[(1-2v)\left(\frac{\partial^2 \phi}{\partial x^2} - \frac{\partial^2 \phi}{\partial y^2}\right) + (1-2v)2i\left(\frac{\partial^2 \phi}{\partial x \partial y}\right)\right. \tag{A. 11}$$

$$\left.\left. + Z\left(\frac{\partial^3 \phi}{\partial x^2 \partial Z} - \frac{\partial^3 \phi}{\partial y^2 \partial Z} + 2i\frac{\partial^3 \phi}{\partial x \partial y \partial Z}\right)\right]\right\}$$

Separate the real and imagine part of the equation, we can get:

$$2\sigma_{xx} = 8G\left\{-\left[(1+2v)\frac{\partial^2 \phi}{\partial Z^2} + Z\frac{\partial^3 \phi}{\partial Z^3}\right]\right.$$

$$+ \left[(1-2v)\left(\frac{\partial^2 \phi}{\partial x^2} - \frac{\partial^2 \phi}{\partial y^2}\right)\right. \tag{A. 12}$$

$$\left.\left. + Z\left(\frac{\partial^3 \phi}{\partial x^2 \partial Z} - \frac{\partial^3 \phi}{\partial y^2 \partial Z}\right)\right]\right\}$$

$$2\,i\,\sigma_{xy} = 8G\left\{\left[(1-2v)2i\left(\frac{\partial^2 \phi}{\partial x \partial y}\right) + Z\left(2i\frac{\partial^3 \phi}{\partial x \partial y \partial Z}\right)\right]\right\} \tag{A. 13}$$

Rearrange the above equations to get:

$$\sigma_{xx} = 4G\left\{\left[(1-2v)\left(\frac{\partial^2\phi}{\partial x^2}-\frac{\partial^2\phi}{\partial y^2}\right)-(1+2v)\frac{\partial^2\phi}{\partial Z^2}\right]\right.$$

$$\left.+Z\left(\frac{\partial^3\phi}{\partial x^2\,\partial Z}-\frac{\partial^3\phi}{\partial y^2\,\partial Z}-\frac{\partial^3\phi}{\partial Z^3}\right)\right\} \tag{A. 14}$$

$$\sigma_{xy} = 8G\left\{\left[(1-2v)\left(\frac{\partial^2\phi}{\partial x\,\partial y}\right)+Z\left(\frac{\partial^3\phi}{\partial x\,\partial y\,\partial Z}\right)\right]\right\} \tag{A. 15}$$

Further rearrange the above equations to get:

$$\sigma_{xx} = 4G\left\{\left[\left(\frac{\partial^2\phi}{\partial x^2}-\frac{\partial^2\phi}{\partial y^2}-\frac{\partial^2\phi}{\partial Z^2}\right)-2v\left(\frac{\partial^2\phi}{\partial x^2}-\frac{\partial^2\phi}{\partial y^2}+\frac{\partial^2\phi}{\partial Z^2}\right)\right]\right.$$

$$\left.+Z\left(\frac{\partial^3\phi}{\partial x^2\,\partial Z}-\frac{\partial^3\phi}{\partial y^2\,\partial Z}-\frac{\partial^3\phi}{\partial Z^3}\right)\right\} \tag{A. 16}$$

$$\sigma_{xy} = 8G\left[(1-2v)\left(\frac{\partial^2\phi}{\partial x\,\partial y}\right)+Z\left(\frac{\partial^3\phi}{\partial x\,\partial y\,\partial Z}\right)\right] \tag{A. 17}$$

For the harmonic function ϕ, we have:

$$\frac{\partial^2\phi}{\partial x^2}+\frac{\partial^2\phi}{\partial y^2}+\frac{\partial^2\phi}{\partial Z^2}=0 \tag{A. 18}$$

$$\sigma_{xx} = 8G\left(\frac{\partial^2\phi}{\partial x^2}+2v\frac{\partial^2\phi}{\partial y^2}+Z\frac{\partial^3\phi}{\partial x^2\,\partial Z}\right) \tag{A. 19}$$

$$\sigma_{xy} = 8G\left[(1-2v)\left(\frac{\partial^2\phi}{\partial x\,\partial y}\right)+Z\left(\frac{\partial^3\phi}{\partial x\,\partial y\,\partial Z}\right)\right] \tag{A. 20}$$

Then, rearrange to get:

$$\sigma_{yy} = 8G \left(\frac{\partial^2 \phi}{\partial y^2} + 2v \frac{\partial^2 \phi}{\partial x^2} + Z \frac{\partial^3 \phi}{\partial y^2 \partial Z} \right) \tag{A. 21}$$

Similar process, we can get other components of stresses:

$$\sigma_{zz} = -8G \left(\frac{\partial^2 \phi}{\partial Z^2} - Z \frac{\partial^3 \phi}{\partial Z^3} \right) \tag{A. 22}$$

$$\sigma_{xz} = 8GZ \frac{\partial^3 \phi}{\partial x \partial Z^2} \tag{A. 23}$$

$$\sigma_{yz} = 8GZ \frac{\partial^3 \phi}{\partial y \partial Z^2} \tag{A. 24}$$

In the following, we will deduce these stresses with expressions by basic parameters.

Solving the Expressions for each Stress Component in Elliptic Functions and Ellipsoidal coordinates:

From the above equations, we can see there are partial derivatives of potential function to the coordinates, so we will first deduce out those partial derivatives.

Before deduction of the equations, let's set a function and a constant for the convenience of expression:

$$Q(s) = s(a^2 + s)(b^2 + s) \tag{A. 25}$$

$$A = \frac{ab^2 (p_f - \sigma_{min})}{16G \ E(k)} \tag{A. 26}$$

Therefore, the potential function can be expressed as:

$$\phi = \frac{A}{2} \int_{\lambda}^{\infty} \left(\frac{x^2}{a^2 + s} + \frac{y^2}{b^2 + s} + \frac{Z^2}{s} - 1 \right) \frac{ds}{\sqrt{s(a^2 + s)(b^2 + s)}} \qquad (A.27)$$

Now, we first deduce the partial derivative of ϕ to coordinate Z, so that we can compare

with previous work. From Eqn.3.3, we get:

$$\frac{\partial \phi}{\partial Z} = \frac{A}{2} \frac{\partial}{\partial Z} \left(\int_{\lambda}^{\infty} \left(\frac{x^2}{a^2 + s} + \frac{y^2}{b^2 + s} + \frac{Z^2}{s} - 1 \right) \frac{ds}{\sqrt{Q(s)}} \right) \qquad (A.28)$$

From the definition of ellipsoidal coordinates , we know that coordinate λ is also a

function of coordinate Z; therefore, the Leibniz Integral Rule is used to solve the above

equation.

According to Leibniz Integral Rule, a more general result, applicable when the limits of

integration a and b and the integrand $f(x, \alpha)$ all are functions of the parameter α is:

$$\frac{\partial}{\partial Z} \int_{a(Z)}^{b(Z)} f(x, Z) dx$$

$$= \int_{a(Z)}^{b(Z)} \frac{\partial f(x, Z)}{\partial Z} dx + f(b(Z), Z) \frac{\partial b}{\partial Z} \qquad (A.29)$$

$$- f(a(Z), Z) \frac{\partial a}{\partial Z}$$

Where the partial derivative of f indicates that inside the integral only the variation of

$f(x, \alpha)$ with α is considered in taking.

Apply the Leibniz Integral Rule to the above equation to get:

$$\frac{\partial \phi}{\partial Z} = \frac{A}{2}\left[\frac{\partial(\infty)}{\partial Z} \frac{\left(\frac{x^2}{a^2+\infty} + \frac{y^2}{b^2+\infty} + \frac{Z^2}{\infty} - 1\right)}{\sqrt{Q(\infty)}} \right.$$
$$- \frac{\partial(\lambda)}{\partial Z} \frac{\left(\frac{x^2}{a^2+\lambda} + \frac{y^2}{b^2+\lambda} + \frac{Z^2}{\lambda} - 1\right)}{\sqrt{Q(\lambda)}} \qquad\qquad (A.30)$$
$$\left. + \int_{\lambda}^{\infty} \frac{\partial}{\partial Z}\left(\frac{\frac{x^2}{a^2+s} + \frac{y^2}{b^2+s} + \frac{Z^2}{s} - 1}{\sqrt{Q(s)}} \right) ds \right]$$

The first part in the bracket of the equation is zero when getting limitation to infinite.

Since we know for the ellipsoidal coordinates, there is expression:

$$\frac{x^2}{a^2+\lambda} + \frac{y^2}{b^2+\lambda} + \frac{Z^2}{\lambda} - 1 = 0 \qquad\qquad (A.31)$$

$$\frac{\partial \phi}{\partial Z} = \frac{A}{2}\left[\int_{\lambda}^{\infty} \frac{\partial}{\partial Z}\left(\frac{\frac{x^2}{a^2+s} + \frac{y^2}{b^2+s} + \frac{Z^2}{s} - 1}{\sqrt{Q(s)}} \right) ds \right] \qquad\qquad (A.32)$$

Further rearrange the above equation, we can get:

$$\frac{\partial \phi}{\partial Z} = AZ \int_{\lambda}^{\infty} \frac{ds}{s\sqrt{Q(s)}} \qquad\qquad (A.33)$$

92

Now, the most difficult step in this deduction is the integral in the above equation. Now, I take it out of the equation and integrate it.

$$\int_\lambda^\infty \frac{ds}{s\sqrt{Q(s)}} = \int_\lambda^\infty \frac{(a^2+s)(b^2+s)}{s(a^2+s)(b^2+s)\sqrt{Q(s)}}\, ds$$

$$= \int_\lambda^\infty \frac{s^2 + (a^2+b^2)s + a^2 b^2}{\left(\sqrt{Q(s)}\right)^3}\, ds \qquad\qquad (A.\,34)$$

$$= \int_\lambda^\infty \frac{3s^2 + 2(a^2+b^2)s + a^2 b^2}{\left(\sqrt{Q(s)}\right)^3}\, ds - \int_\lambda^\infty \frac{2s^2 + (a^2+b^2)s}{\left(\sqrt{Q(s)}\right)^3}\, ds$$

Rearrange Eqn.A.34:

$$\int_\lambda^\infty \frac{ds}{s\sqrt{Q(s)}} = \int_\lambda^\infty \frac{d\big(Q(s)\big)}{\left(\sqrt{Q(s)}\right)^3}$$

$$-\int_\lambda^\infty \frac{2s^2 + (a^2+b^2)s}{s(a^2+s)(b^2+s)\sqrt{Q(s)}}\, ds$$

$$= \left.\frac{-2}{\sqrt{Q(s)}}\right|_\lambda^\infty - \int_\lambda^\infty \frac{2s^2 + (a^2+b^2)s}{s(a^2+s)(b^2+s)\sqrt{Q(s)}}\, ds \qquad (A.\,35)$$

$$= \frac{2}{\sqrt{Q(\lambda)}} - \int_\lambda^\infty \frac{2s + (a^2+b^2)}{(a^2+s)(b^2+s)\sqrt{Q(s)}}\, ds$$

$$\frac{\partial \phi}{\partial Z} = AZ\left\{\frac{2}{\sqrt{Q(\lambda)}} - \int_\lambda^\infty \frac{2s + (a^2+b^2)}{(a^2+s)(b^2+s)\sqrt{Q(s)}}\, ds\right\} \qquad .\,36)$$

In the following deduction, we will first get rid of the integral to simplify Eqn.A.36. For

93

this integral, I get the help from software Mathematica and the integral result is shown in

the following. The indefinite integral of it is given for simplification (because the definite

integral could not be given by software).

$$
\int \frac{2s + (a^2+b^2)}{(a^2 + s)(b^2 + s)\sqrt{Q(s)}}\,ds
$$

$$
= \Bigg\{ 2s \Bigg(\Bigg(\sqrt{\frac{s}{b^2+s}} \Bigg) (a^2 + b^2 + s)
$$

$$
+ i\, a^2 \sqrt{1 + \frac{s}{a^2}}\, \mathrm{EllipticE}\left[i\, \mathrm{ArcSinh}\left[\sqrt{\frac{s}{b^2}} \right], \frac{b^2}{a^2} \right] \qquad (A.\,37)
$$

$$
- i\, a^2 \sqrt{1 + \frac{s}{a^2}}\, \mathrm{EllipticF}\left[i\, \mathrm{ArcSinh}\left[\sqrt{\frac{s}{b^2}} \right], \frac{b^2}{a^2} \right] \Bigg) \Bigg\}
$$

$$
\Bigg/ \left(a^2 b^2 \sqrt{\frac{s}{b^2+s}} \sqrt{s(a^2 + s)(b^2 + s)} \right)
$$

In which:

EllipticE[φ,m]=E[φ|m], gives the elliptical integral of the second kind.

EllipticF[φ,m]=F[φ|m], gives the elliptical integral of the first kind.

The above equation needs to be simplified for the definite integral; therefore, in the first step,

I divided it into three parts to simplify:

$$\int \frac{2s + (a^2+b^2)}{(a^2 + s)(b^2 + s)\sqrt{Q(s)}} ds = (1) + (2) - (3)$$

$$(1) = \frac{2s\left(\sqrt{\frac{s}{b^2 + s}}\right)(a^2 + b^2 + s)}{\left(a^2 b^2 \sqrt{\frac{s}{b^2 + s}} \sqrt{s(a^2 + s)(b^2 + s)}\right)}$$

$$(2) = \frac{2s\, i\, a^2 \sqrt{1 + \frac{s}{a^2}}\, \text{EllipticE}\left[i\, \text{ArcSinh}\left[\sqrt{\frac{s}{b^2}}\right], \frac{b^2}{a^2}\right]}{\left(a^2 b^2 \sqrt{\frac{s}{b^2 + s}} \sqrt{s(a^2 + s)(b^2 + s)}\right)}$$

(A. 38)

$$(3) = \frac{2s\left(i\, a^2 \sqrt{1 + \frac{s}{a^2}}\, \text{EllipticF}\left[i\, \text{ArcSinh}\left[\sqrt{\frac{s}{b^2}}\right], \frac{b^2}{a^2}\right]\right)}{\left(a^2 b^2 \sqrt{\frac{s}{b^2 + s}} \sqrt{s(a^2 + s)(b^2 + s)}\right)}$$

For part (1) of Eqn.A.38, it is simplified as:

$$(1) = \frac{2s\left(\sqrt{\frac{s}{b^2 + s}}\right)(a^2 + b^2 + s)}{\left(a^2 b^2 \sqrt{\frac{s}{b^2 + s}} \sqrt{s(a^2 + s)(b^2 + s)}\right)}$$

$$= \frac{2s(a^2 + b^2 + s)}{a^2 b^2 \sqrt{s(a^2 + s)(b^2 + s)}}$$

(A. 39)

$$= \frac{2}{ab^2}\left\{\frac{s(a^2 + s)}{a\sqrt{s(a^2 + s)(b^2 + s)}} + \frac{b^2 s}{a\sqrt{s(a^2 + s)(b^2 + s)}}\right\}$$

Eqn.A.39 is kept here for future simplification of the integral.

In the following are the deductions of part (2) and (3) of Eqn.A.38.

Firstly simplify part (2) as:

$$(2) = \frac{2s\,i\,a^2\sqrt{1+\dfrac{s}{a^2}}\,\text{EllipticE}\left[i\,\text{ArcSinh}\left[\sqrt{\dfrac{s}{b^2}}\right],\dfrac{b^2}{a^2}\right]}{\left(a^2 b^2 \sqrt{\dfrac{s}{b^2+s}}\sqrt{s(a^2+s)(b^2+s)}\right)}$$

$$= \frac{2}{ab^2}\left\{\frac{s\,i\,a\sqrt{\dfrac{a^2+s}{a^2}}\,\text{EllipticE}\left[i\,\text{ArcSinh}\left[\sqrt{\dfrac{s}{b^2}}\right],\dfrac{b^2}{a^2}\right]}{\left(\sqrt{\dfrac{s}{b^2+s}}\sqrt{s(a^2+s)(b^2+s)}\right)}\right\} \tag{A. 40}$$

$$= \frac{2}{ab^2}\left\{i\,\text{EllipticE}\left[i\,\text{ArcSinh}\left[\sqrt{\dfrac{s}{b^2}}\right],\dfrac{b^2}{a^2}\right]\right\}$$

In Eqn.A.40, what we need to deal with is the elliptical integral. Before simplifying this equation, the knowledge of elliptical integral is introduced here as addition equations:

$$E(\varphi,k) = E(u|m) = E(\varphi\backslash\alpha) = \int_0^\varphi \sqrt{\left(1-\sin^2(\alpha)\sin^2(\theta)\right)}\,d\theta$$

$$= \int_0^\varphi \sqrt{\left(1-m\sin^2(\theta)\right)}\,d\theta \tag{A. 41}$$

$$= \int_0^\varphi \sqrt{\left(1-k^2\sin^2(\theta)\right)}\,d\theta$$

$$= \int_0^u \text{dn}^2 w\,dw$$

In which, the incomplete elliptical integral of the second kind can be expressed in different parameters. The relations between those variables are shown as:

$$m = \sin^2(\alpha) = k^2 \tag{A. 42}$$

$$\sin(\varphi) = sn\,u$$

96

$$\cos(\varphi) = cn\, u$$

In which the sn, cn and dn are Jacobi elliptic functions, which have the following

characteristics:

From the equation, we have the expression for E[φ|m]. Because the existences of the

imaginary number *i*, the equation from Aramowitz and Stegun (1970) is referred here:

$$E(i\,\varphi\backslash\alpha) = -i\,E\left(\theta\backslash\frac{\pi}{2} - \alpha\right) + i\,F\left(\theta\backslash\frac{\pi}{2} - \alpha\right)$$
$$+i\tan\theta\left(1 - cos^2(\alpha)sin^2(\theta)\right)^{1/2}$$

(A. 43)

In which, tan(θ)=sinh(φ).

Now the expression for E[φ|m]: $i\,\text{EllipticE}\left[i\,\text{ArcSinh}\left[\sqrt{\frac{s}{b^2}}\right], \frac{b^2}{a^2}\right]$, we have the following

relations: if we consider it as E[*i* φ|*m*]:

$$\varphi = \text{ArcSinh}\left[\sqrt{\frac{s}{b^2}}\right]$$

(A. 44)

$$m = \sin^2(\alpha) = \frac{b^2}{a^2}$$

$$tan\theta = \sqrt{\frac{s}{b^2}}$$

(A. 45)

$$\alpha = \text{ArcSin}\left(\frac{b}{a}\right)$$

Therefore, it can be changed to:

97

$$(2) = \frac{2}{ab^2}\left\{i\ \text{EllipticE}\left[i\ \text{ArcSinh}\left[\sqrt{\frac{s}{b^2}}\right],\frac{b^2}{a^2}\right]\right\}$$

$$= \frac{2}{ab^2}i\left\{-i\ E\left(\theta\backslash\frac{\pi}{2}-\alpha\right)+i\ F\left(\theta\backslash\frac{\pi}{2}-\alpha\right)\right.$$

$$\left.+i\tan\theta\left(1-cos^2(\alpha)sin^2(\theta)\right)^{1/2}\right\}$$

(A. 46)

Similarly, we have:

$$F(i\ \varphi\backslash\alpha)=i\ F\left(\theta\backslash\frac{\pi}{2}-\alpha\right)$$

(A. 47)

And like part 2, part 3 could be changed to:

$$(3)=\frac{2s\left(i\ a^2\sqrt{1+\frac{s}{a^2}}\ \text{EllipticF}\left[i\ \text{ArcSinh}\left[\sqrt{\frac{s}{b^2}}\right],\frac{b^2}{a^2}\right]\right)}{\left(a^2b^2\sqrt{\frac{s}{b^2+s}}\ \sqrt{s(a^2+s)(b^2+s)}\right)}$$

$$=\frac{2}{ab^2}\left\{i\ \text{EllipticF}\left[i\ \text{ArcSinh}\left[\sqrt{\frac{s}{b^2}}\right],\frac{b^2}{a^2}\right]\right\}$$

$$=\frac{2}{ab^2}i\left\{i\ F\left(\theta\backslash\frac{\pi}{2}-\alpha\right)\right\}$$

(A. 48)

Now, let's put the above equations together:

$$\int \frac{2s + (a^2+b^2)}{(a^2 + s)(b^2 + s)\sqrt{Q(s)}} ds = (1) + (2) - (3)$$

$$= \frac{2}{ab^2}\left\{\frac{s(a^2 + s)}{a\sqrt{s(a^2 + s)(b^2 + s)}}\right.$$

$$+ \left.\frac{b^2 s}{a\sqrt{s(a^2 + s)(b^2 + s)}}\right\} \tag{A.49}$$

$$+ \frac{2}{ab^2}i\left\{-i\,E\left(\theta\backslash\frac{\pi}{2} - \alpha\right) + i\,F\left(\theta\backslash\frac{\pi}{2} - \alpha\right)\right.$$

$$+ \left. i\tan\theta\left(1 - cos^2(\alpha)sin^2(\theta)\right)^{1/2}\right\}$$

$$- \frac{2}{ab^2}i\left\{i\,F\left(\theta\backslash\frac{\pi}{2} - \alpha\right)\right\}$$

Rearrange equation A.49, cancel the part for elliptical integral of the first kind, and cancel the imaginary number, we can get:

$$\int \frac{2s + (a^2+b^2)}{(a^2 + s)(b^2 + s)\sqrt{Q(s)}} ds$$

$$= \frac{2}{ab^2}\left\{\frac{s(a^2 + s)}{a\sqrt{s(a^2 + s)(b^2 + s)}}\right.$$

$$+ \left.\frac{b^2 s}{a\sqrt{s(a^2 + s)(b^2 + s)}}\right\} \tag{A.50}$$

$$+ \frac{2}{ab^2}\left\{E\left(\theta\backslash\frac{\pi}{2} - \alpha\right)\right.$$

$$- \left.\tan\theta\left(1 - cos^2(\alpha)sin^2(\theta)\right)^{1/2}\right\}$$

Obviously, Eqn.A.50 still needs to improve, so let's consider the expressions for θ and α.

$$tan\theta = \sqrt{\frac{s}{b^2}} \Rightarrow sin^2(\theta) = \frac{s}{s + b^2} \tag{A.51}$$

$$\alpha = \text{ArcSin}\left(\frac{b}{a}\right) \Rightarrow cos^2(\alpha) = \frac{a^2 - b^2}{a^2} \tag{A. 52}$$

Then,

$$\int \frac{2s + (a^2 + b^2)}{(a^2 + s)(b^2 + s)\sqrt{Q(s)}}ds$$

$$= \frac{2}{ab^2}\left\{\frac{s(a^2 + s)}{a\sqrt{s(a^2 + s)(b^2 + s)}}\right.$$

$$+ \frac{b^2 s}{a\sqrt{s(a^2 + s)(b^2 + s)}}\right\} \tag{A. 53}$$

$$+ \frac{2}{ab^2}\left\{E\left(\text{Arctan}\left(\sqrt{\frac{s}{b^2}}\right)\backslash\frac{\pi}{2} - \text{ArcSin}\left(\frac{b}{a}\right)\right)\right.$$

$$\left. - \sqrt{\frac{s}{b^2}}\left(1 - \frac{a^2 - b^2}{a^2}\frac{s}{s + b^2}\right)^{1/2}\right\}$$

Rearrange the upper equation:

Now, equation should be rearranged to simplify the expression. According to Aramowitz and Stegun (1970),

$$E(K - u) = E(k) - E(u) + k^2 \, sn(u)cd(u) \tag{A. 54}$$

In which, K is the quarter period of elliptic functions and expressed as:

$$K = \int_0^{\frac{\pi}{2}} \frac{1}{\sqrt{(1 - m\sin^2(\theta))}}d\theta = \int_0^{\frac{\pi}{2}} \frac{1}{\sqrt{(1 - k^2\sin^2(\theta))}}d\theta \tag{A. 55}$$

And u is related Jacobian Elliptic Functions and defined by:

$$u = \int_0^{\varphi} \frac{1}{\sqrt{(1 - m\sin^2(\theta))}} \, d\theta = \int_0^{\varphi} \frac{1}{\sqrt{(1 - k^2\sin^2(\theta))}} \, d\theta \qquad \text{(A. 56)}$$

Then, we can derive:

$$\frac{\dfrac{cnu}{dnu}}{k'\dfrac{snu}{dnu}} = \frac{\sin\left(Arctan\left(\sqrt{\dfrac{\lambda}{b^2}}\right)\right)}{\cos\left(Arctan\left(\sqrt{\dfrac{\lambda}{b^2}}\right)\right)} \qquad \text{(A. 57)}$$

Rearranging:

$$\frac{cnu}{k'snu} = \sqrt{\frac{\lambda}{b^2}} \qquad \text{(A. 58)}$$

We have known that:

$$k' = \sqrt{1 - k^2} = b/a \qquad \text{(A. 59)}$$

Put equation 3.48 into equation 3.47 and rearrange it to get:

$$\lambda = \frac{a^2 cn^2 u}{sn^2 u} \qquad \text{(A. 60)}$$

Now, we know all the expressions for the different parameters in the elliptical integral.

Now, let's summarize all the deduction for integral and put them back to the original

potential equation:

101

$$\frac{\partial \phi}{\partial Z} = AZ \left\{ \frac{2}{\sqrt{Q(\lambda)}} \right.$$

$$+ \frac{2}{ab^2} \left[\frac{b^2 \lambda}{a\sqrt{\lambda(a^2 + \lambda)(b^2 + \lambda)}} - E(u) \right. \tag{A. 61}$$

$$\left. \left. + k^2 \frac{snu\ cnu}{dnu} \right] \right\}$$

Now, we will further simplify it by using Jacobian elliptic functions instead of the

coordinate λ:

$$\frac{2}{\sqrt{Q(\lambda)}} = \frac{2}{\sqrt{\lambda(a^2 + \lambda)(b^2 + \lambda)}}$$

$$= \frac{2}{\sqrt{\frac{a^2 cn^2 u}{sn^2 u} \left(a^2 + \frac{a^2 cn^2 u}{sn^2 u}\right)\left(b^2 + \frac{a^2 cn^2 u}{sn^2 u}\right)}} \tag{A. 62}$$

$$= \frac{2}{ab^2} \left[\frac{snu\ dnu}{cnu} - \frac{snu\ cnu}{dnu} \right]$$

$$\frac{b^2 \lambda}{a\sqrt{\lambda(a^2 + \lambda)(b^2 + \lambda)}} = -k^2 \frac{snu\ cnu}{dnu} + \frac{snu\ cnu}{dnu} \tag{A. 63}$$

$$\frac{\partial \phi}{\partial Z} = AZ \frac{2}{ab^2} \left\{ \frac{snu\ dnu}{cnu} - \frac{snu\ cnu}{dnu} - k^2 \frac{snu\ cnu}{dnu} + \frac{snu\ cnu}{dnu} \right.$$

$$\left. - E(u) + k^2 \frac{snu\ cnu}{dnu} \right\} = \frac{2AZ}{ab^2} \left\{ \frac{snu\ dnu}{cnu} - E(u) \right\} \tag{A. 64}$$

The first important step for this whole deduction process is now finished.

With similar process, we can also deduce the other partial derivatives used for the stresses

by repeating all the previous deductions x, y and Z coordinates respectively. (Detailed

deducing processes are lengthy and done manually, not listed in the following)

$$\frac{\partial^2 \phi}{\partial Z^2} = \frac{2A}{ab^2}\left\{\frac{snu\ dnu}{cnu} - E(u)\right\} + \frac{2AZ}{ab^2}\left\{k'^2\frac{sn^2u}{cn^2u}\right\}\frac{du}{d\lambda}\frac{\partial\lambda}{\partial Z} \qquad (A.\,65)$$

$$\frac{\partial^3 \phi}{\partial Z^3} = \frac{4A}{ab^2}\left\{k'^2\frac{sn^2u}{cn^2u}\right\}\frac{du}{d\lambda}\frac{\partial\lambda}{\partial Z}$$

$$+ \frac{2AZ}{ab^2}\left\{k'^2\frac{sn^2u}{cn^2u}\right\}\left\{\frac{d^2u}{d\lambda^2}\left(\frac{\partial\lambda}{\partial Z}\right)^2 + \frac{du}{d\lambda}\frac{\partial^2\lambda}{\partial Z^2}\right\} \qquad (A.\,66)$$

$$+ \frac{4AZ}{ab^2}\left\{k'^2\frac{snu\ dnu}{cn^3u}\right\}\left(\frac{du}{d\lambda}\right)^2\left(\frac{\partial\lambda}{\partial Z}\right)^2$$

$$\frac{\partial\phi}{\partial x} = \frac{2Ax}{a^3k^2}\{u - E(u)\} \qquad (A.\,67)$$

$$\frac{\partial\phi}{\partial y} = \frac{2Ay}{a^3k^2}\left\{\left(\frac{a}{b}\right)^2 E(u) - u - \frac{a^2-b^2}{b^2}\frac{snu\ cnu}{dnu}\right\} \qquad (A.\,68)$$

$$\frac{\partial^2\phi}{\partial x\partial y} = \frac{2Ax}{a^3k^2}\left\{\frac{du}{d\lambda}\frac{\partial\lambda}{\partial y} - dn^2u\frac{du}{d\lambda}\frac{\partial\lambda}{\partial y}\right\} = \frac{2Ax}{a^3}\left\{sn^2u\frac{du}{d\lambda}\frac{\partial\lambda}{\partial y}\right\} \qquad (A.\,69)$$

$$\frac{\partial^2\phi}{\partial x^2} = \frac{2A}{a^3k^2}\{u - E(u)\} + \frac{2Ax}{a^3k^2}\left\{sn^2u\frac{du}{d\lambda}\frac{\partial\lambda}{\partial x}\right\} \qquad (A.\,70)$$

$$\frac{\partial^2\phi}{\partial y^2} = \frac{2A}{a^3k^2}\left\{\left(\frac{a}{b}\right)^2 E(u) - u - \frac{a^2-b^2}{b^2}\frac{snu\ cnu}{dnu}\right\}$$

$$+ \frac{2Ay}{a^3k^2}\left\{\left(\frac{a}{b}\right)^2 dn^2u - 1\right. \qquad (A.\,71)$$

$$\left. - \frac{a^2-b^2}{b^2}\left(\frac{cn^2u}{dn^2u} - sn^2u\right)\right\}\frac{du}{d\lambda}\frac{\partial\lambda}{\partial y}$$

$$\frac{\partial^3\phi}{\partial x^2\partial Z} = \frac{2A}{a^3}\left\{sn^2u\frac{du}{d\lambda}\frac{\partial\lambda}{\partial Z}\right\}$$

$$+ \frac{2Ax}{a^3k^2}\left\{2snu\ cnu\ dnu\left(\frac{du}{d\lambda}\right)^2\frac{\partial\lambda}{\partial x}\frac{\partial\lambda}{\partial Z}\right. \qquad (A.\,72)$$

$$\left. + sn^2u\left(\frac{d^2u}{d\lambda^2}\frac{\partial\lambda}{\partial x}\frac{\partial\lambda}{\partial Z} + \frac{du}{d\lambda}\frac{\partial^2\lambda}{\partial x\partial Z}\right)\right\}$$

$$\frac{\partial^3 \phi}{\partial y^2 \partial Z} = \frac{2A}{a^3 k^2} \left\{ \left(\frac{a}{b}\right)^2 dn^2 u - 1 - \frac{a^2 - b^2}{b^2} \left(\frac{cn^2 u}{dn^2 u} - sn^2 u\right) \right\} \frac{du}{d\lambda} \frac{\partial \lambda}{\partial Z}$$

$$+ \frac{2Ay}{a^3 k^2} \left\{ \left(\frac{a}{b}\right)^2 2(-k^2) dnu\, cnu\, snu \right.$$

$$+ 2\frac{a^2 - b^2}{b^2} \left(\frac{(k'^2)snu\, cnu}{dn^3 u}\right.$$

$$\left. + snu\, cnu\, dnu \right) \right\} \left(\frac{du}{d\lambda}\right)^2 \frac{\partial \lambda}{\partial y} \frac{\partial \lambda}{\partial Z}$$

$$+ \frac{2Ay}{a^3 k^2} \left\{ \left(\frac{a}{b}\right)^2 dn^2 u - 1 \right.$$

$$\left. - \frac{a^2 - b^2}{b^2} \left(\frac{cn^2 u}{dn^2 u} - sn^2 u\right) \right\} \left\{ \frac{d^2 u}{d\lambda^2} \frac{\partial \lambda}{\partial y} \frac{\partial \lambda}{\partial Z} + \frac{du}{d\lambda} \frac{\partial^2 \lambda}{\partial y\, \partial Z} \right\}$$

(A. 73)

$$\frac{\partial^3 \phi}{\partial Z^2 \partial x} = \frac{2A}{ab^2} \left\{ k'^2 \frac{sn^2 u}{cn^2 u} \right\} \frac{du}{d\lambda} \frac{\partial \lambda}{\partial x}$$

$$+ \frac{2AZ}{ab^2} \left\{ \left(\frac{(k'^2)snu\, dnu}{cn^3 u}\right) \left(\frac{du}{d\lambda}\right)^2 \frac{\partial \lambda}{\partial x} \frac{\partial \lambda}{\partial Z} \right.$$

$$\left. + \left(k'^2 \frac{sn^2 u}{cn^2 u}\right) \left(\frac{d^2 u}{d\lambda^2} \frac{\partial \lambda}{\partial x} \frac{\partial \lambda}{\partial Z} + \frac{du}{d\lambda} \frac{\partial^2 \lambda}{\partial x\, \partial Z}\right) \right\}$$

(A. 74)

$$\frac{\partial^3 \phi}{\partial Z^2 \partial y} = \frac{2A}{ab^2} \left\{ k'^2 \frac{sn^2 u}{cn^2 u} \right\} \frac{du}{d\lambda} \frac{\partial \lambda}{\partial y}$$

$$+ \frac{2AZ}{ab^2} \left\{ \left(\frac{(k'^2)snu\, dnu}{cn^3 u}\right) \left(\frac{du}{d\lambda}\right)^2 \frac{\partial \lambda}{\partial y} \frac{\partial \lambda}{\partial Z} \right.$$

$$\left. + \left(k'^2 \frac{sn^2 u}{cn^2 u}\right) \left(\frac{d^2 u}{d\lambda^2} \frac{\partial \lambda}{\partial y} \frac{\partial \lambda}{\partial Z} + \frac{du}{d\lambda} \frac{\partial^2 \lambda}{\partial y\, \partial Z}\right) \right\}$$

(A. 75)

$$\frac{\partial^3 \phi}{\partial x \partial y \partial Z} = \frac{2Ax}{a^3}\left\{2snu\ cnu\ dnu\left(\frac{du}{d\lambda}\right)^2 \frac{\partial\lambda}{\partial Z}\frac{\partial\lambda}{\partial y}\right.$$

$$\left. + sn^2u\left(\frac{d^2u}{d\lambda^2}\frac{\partial\lambda}{\partial y}\frac{\partial\lambda}{\partial Z} + \frac{du}{d\lambda}\frac{\partial^2\lambda}{\partial y\,\partial Z}\right)\right\}$$

(A. 76)

$$\sigma_{xx} = 8G\left(\frac{2A}{a^3k^2}\{u - E(u)\} + \frac{2Ax}{a^3k^2}\left\{sn^2u\frac{du}{d\lambda}\frac{\partial\lambda}{\partial x}\right\}\right.$$

$$+ 2v\frac{2A}{a^3k^2}\left\{\left(\frac{a}{b}\right)^2 E(u) - u - \frac{a^2 - b^2}{b^2}\frac{snu\ cnu}{dnu}\right\}$$

$$+ \frac{2Ay}{a^3k^2}\left\{\left(\frac{a}{b}\right)^2 dn^2u - 1\right.$$

$$\left.- \frac{a^2 - b^2}{b^2}\left(\frac{cn^2u}{dn^2u} - sn^2u\right)\right\}\frac{du}{d\lambda}\frac{\partial\lambda}{\partial y}$$

(A. 77)

$$+ Z\frac{2A}{a^3}\left\{sn^2u\frac{du}{d\lambda}\frac{\partial\lambda}{\partial Z}\right\}$$

$$+ \frac{2Ax}{a^3k^2}\left\{2snu\ cnu\ dnu\left(\frac{du}{d\lambda}\right)^2 \frac{\partial\lambda}{\partial x}\frac{\partial\lambda}{\partial Z}\right.$$

$$\left.\left.+ sn^2u\left(\frac{d^2u}{d\lambda^2}\frac{\partial\lambda}{\partial x}\frac{\partial\lambda}{\partial Z} + \frac{du}{d\lambda}\frac{\partial^2\lambda}{\partial x\,\partial Z}\right)\right\}\right)$$

$$\sigma_{xy} = 8G\left[(1 - 2v)\left(\frac{2Ax}{a^3}\left\{sn^2u\frac{du}{d\lambda}\frac{\partial\lambda}{\partial y}\right\}\right)\right.$$

$$+ Z\left(\frac{2Ax}{a^3}\left\{2snu\ cnu\ dnu\left(\frac{du}{d\lambda}\right)^2 \frac{\partial\lambda}{\partial Z}\frac{\partial\lambda}{\partial y}\right.\right.$$

(A. 78)

$$\left.\left.\left.+ sn^2u\left(\frac{d^2u}{d\lambda^2}\frac{\partial\lambda}{\partial y}\frac{\partial\lambda}{\partial Z} + \frac{du}{d\lambda}\frac{\partial^2\lambda}{\partial y\,\partial Z}\right)\right\}\right)\right]$$

$$\sigma_{yy} = 8G\left(\frac{2A}{a^3k^2}\left\{\left(\frac{a}{b}\right)^2 E(u) - u - \frac{a^2-b^2}{b^2}\frac{snu\ cnu}{dnu}\right\}\right.$$

$$+\frac{2Ay}{a^3k^2}\left\{\left(\frac{a}{b}\right)^2 dn^2u - 1\right.$$

$$-\frac{a^2-b^2}{b^2}\left(\frac{cn^2u}{dn^2u} - sn^2u\right)\right\}\frac{du}{d\lambda}\frac{\partial\lambda}{\partial y}$$

$$+2v\frac{2A}{a^3k^2}\{u - E(u)\} + \frac{2Ax}{a^3k^2}\left\{sn^2u\frac{du}{d\lambda}\frac{\partial\lambda}{\partial x}\right\}$$

$$+Z\frac{2A}{a^3k^2}\left\{\left(\frac{a}{b}\right)^2 dn^2u - 1\right.$$

$$-\frac{a^2-b^2}{b^2}\left(\frac{cn^2u}{dn^2u} - sn^2u\right)\right\}\frac{du}{d\lambda}\frac{\partial\lambda}{\partial Z}$$

$$+\frac{2Ay}{a^3k^2}\left\{\left(\frac{a}{b}\right)^2 2(-k^2)dnu\ cnu\ snu\right.$$

$$+2\frac{a^2-b^2}{b^2}\left(\frac{(k'^2)snu\ cnu}{dn^3u}\right.$$

$$\left.+ snu\ cnu\ dnu\right)\right\}\left(\frac{du}{d\lambda}\right)^2\frac{\partial\lambda}{\partial y}\frac{\partial\lambda}{\partial Z}$$

(A. 79)

$$+\frac{2Ay}{a^3k^2}\left\{\left(\frac{a}{b}\right)^2 dn^2u - 1\right.$$

$$-\frac{a^2-b^2}{b^2}\left(\frac{cn^2u}{dn^2u} - sn^2u\right)\right\}\left\{\frac{d^2u}{d\lambda^2}\frac{\partial\lambda}{\partial y}\frac{\partial\lambda}{\partial Z}\right.$$

$$\left.+\frac{du}{d\lambda}\frac{\partial^2\lambda}{\partial y\ \partial Z}\right\}\right)$$

(A. 80)

$$\sigma_{xz} = 8GZ\,\frac{2A}{ab^2}\left\{k'^2\,\frac{sn^2u}{cn^2u}\right\}\frac{du}{d\lambda}\frac{\partial\lambda}{\partial x}$$

$$+\frac{2AZ}{ab^2}\left\{\left(\frac{(k'^2)snu\,dnu}{cn^3u}\right)\left(\frac{du}{d\lambda}\right)^2\frac{\partial\lambda}{\partial x}\frac{\partial\lambda}{\partial Z}\right.\tag{A. 81}$$

$$\left.+\left(k'^2\,\frac{sn^2u}{cn^2u}\right)\left(\frac{d^2u}{d\lambda^2}\frac{\partial\lambda}{\partial x}\frac{\partial\lambda}{\partial Z}+\frac{du}{d\lambda}\frac{\partial^2\lambda}{\partial x\,\partial Z}\right)\right\}$$

$$\sigma_{yz} = 8GZ\,\frac{2A}{ab^2}\left\{k'^2\,\frac{sn^2u}{cn^2u}\right\}\frac{du}{d\lambda}\frac{\partial\lambda}{\partial y}$$

$$+\frac{2AZ}{ab^2}\left\{\left(\frac{(k'^2)snu\,dnu}{cn^3u}\right)\left(\frac{du}{d\lambda}\right)^2\frac{\partial\lambda}{\partial y}\frac{\partial\lambda}{\partial Z}\right.\tag{A. 82}$$

$$\left.+\left(k'^2\,\frac{sn^2u}{cn^2u}\right)\left(\frac{d^2u}{d\lambda^2}\frac{\partial\lambda}{\partial y}\frac{\partial\lambda}{\partial Z}+\frac{du}{d\lambda}\frac{\partial^2\lambda}{\partial y\,\partial Z}\right)\right\}$$

In which: sn, du, and cn are Jacobian elliptic functions; A is given by:

$$A = \frac{ab^2(p_f - \sigma_{min})}{16G\,E(k)}\tag{A. 83}$$

$$\lambda = \frac{a^2cn^2u}{sn^2u}\tag{A. 84}$$

$$k' = \sqrt{1-k^2} = b/a\tag{A. 85}$$

$$\frac{du}{d\lambda} = \frac{-1}{2a^3}\frac{sn^3u}{cnu\,dnu}\tag{A. 86}$$

$$\frac{d^2u}{d\lambda^2} = \frac{-sn^2u}{2a^2}\left(3 + \frac{sn^2u}{cn^2u} + k^2\,\frac{sn^2u}{dn^2u}\right)\frac{du}{d\lambda}\tag{A. 87}$$

$$\frac{\partial \lambda}{\partial Z} = \frac{Z}{2\lambda H_1^2} = \frac{2Z(a^2 + \lambda)(b^2 + \lambda)}{(\lambda - \mu)(\lambda - \varepsilon)} \tag{A.88}$$

$$\frac{\partial^2 \lambda}{\partial Z^2} = \frac{1}{2\lambda H_1^2} \left[1 - \frac{Z^2}{\lambda^2 H_1^2} + \frac{Z^2}{4\lambda^2 H_1^2} \left\{ \frac{x^2}{(a^2 + \lambda)^3} + \frac{y^2}{(b^2 + \lambda)^3} + \frac{Z^2}{\lambda^3} \right\} \right] \tag{A.89}$$

$$H_1^2 = \frac{(\lambda - \mu)(\lambda - \varepsilon)}{4\lambda(a^2 + \lambda)(b^2 + \lambda)} \tag{A.90}$$

Similarly, the other partial derivates and parameters can also be expressed by:

$$\frac{\partial \lambda}{\partial x} = \frac{x}{2(a^2 + \lambda)H_1^2} \tag{A.91}$$

$$\frac{\partial \lambda}{\partial y} = \frac{y}{2(b^2 + \lambda)H_1^2} \tag{A.92}$$

$$\frac{\partial^2 \lambda}{\partial x \, \partial Z} = \frac{x}{2} \left\{ \frac{-1}{(a^2 + \lambda)^2 H_1^4} \left[H_1^2 \frac{\partial \lambda}{\partial Z} + (a^2 + \lambda) \frac{\partial(H_1^2)}{\partial Z} \right] \right\} \tag{A.93}$$

$$\frac{\partial^2 \lambda}{\partial y \, \partial Z} = \frac{y}{2} \left\{ \frac{-1}{(b^2 + \lambda)^2 H_1^4} \left[H_1^2 \frac{\partial \lambda}{\partial Z} + (b^2 + \lambda) \frac{\partial(H_1^2)}{\partial Z} \right] \right\} \tag{A.94}$$

$$\frac{\partial(H_1^2)}{\partial Z} = \frac{\partial(H_1^2)}{\partial \lambda} \frac{\partial \lambda}{\partial Z} + \frac{\partial(H_1^2)}{\partial \mu} \frac{\partial \mu}{\partial Z} + \frac{\partial(H_1^2)}{\partial \varepsilon} \frac{\partial \varepsilon}{\partial Z} \tag{A.95}$$

$$\frac{\partial(H_1^2)}{\partial \lambda} = \frac{2\lambda - \varepsilon - \mu}{4\lambda(a^2 + \lambda)(b^2 + \lambda)} - \frac{(\lambda - \varepsilon)(\lambda - \mu)}{4\lambda(a^2 + \lambda)(b^2 + \lambda)^2}$$

$$- \frac{(\lambda - \varepsilon)(\lambda - \mu)}{4\lambda(a^2 + \lambda)^2(b^2 + \lambda)}$$

$$- \frac{(\lambda - \varepsilon)(\lambda - \mu)}{4\lambda^2(a^2 + \lambda)(b^2 + \lambda)} \tag{A.96}$$

$$\frac{\partial(H_1^2)}{\partial \mu} = \frac{\mu - \lambda}{4\lambda(a^2 + \lambda)(b^2 + \lambda)} \tag{A.97}$$

$$\frac{\partial(H_1^2)}{\partial \varepsilon} = \frac{\varepsilon - \lambda}{4\lambda(a^2 + \lambda)(b^2 + \lambda)} \tag{A.98}$$

$$\frac{\partial \mu}{\partial Z} = \frac{Z}{2\lambda H_2^2} \tag{A.99}$$

$$\frac{\partial \varepsilon}{\partial Z} = \frac{Z}{2\lambda H_3^2} \tag{A.100}$$

$$H_2^2 = \frac{(\mu - \lambda)(\mu - \varepsilon)}{4\mu(a^2 + \mu)(b^2 + \mu)} \tag{A.101}$$

$$H_3^2 = \frac{(\varepsilon - \lambda)(\varepsilon - \mu)}{4\varepsilon(a^2 + \varepsilon)(b^2 + \varepsilon)} \tag{A.102}$$

All these equations are to be examined and proved through a FORTRAN program.

APPENDIX B

SLIP MAP AND STRUCTURAL PERMEABILITY DIAGRAM

The slip maps of natural fractures in a given stress field are investigated by Jaeger and

Rosengren (1969). In their work, the following assumptions were made:

- The directions and magnitudes of the principal stresses are given, expressed by the

  parameters $\sigma_1, \sigma_2, \sigma_3$, and their directions.

- The orientations of natural fracture planes relative to the principal stresses

  (expressed by the angles between the normal of the joint and the directions of σ_1,

  σ_3: θ_1, θ_3), and the friction and cohesion of natural fractures (c and μ).

- Assuming the uniform conditions in the formations

Mohr-Coulomb failure criterion is used (Warpinski et al., 2004):

$$|\tau| = \tau_s + \sigma_n ' \tan \varphi' \tag{B.1}$$

Where τ is the shear stress, τs is the shear strength or cohesive strength, σn' is the effective

normal stress and φ' is the joint friction angle.

The conditions for sliding across any plane will be taken to be given by equation B.1. This

relation is represented by the line ABC in Fig.B.1. The normal and shear stress across a

plane whose normal makes angles θ_1, θ_3, respectively, with the direction of the principal

110

stresses σ_1, σ_3, is found by the usual three dimensional Mohr construction and is represented by the point P on Fig.B.1 (Jaeger and Rosengren, 1969). Here, the points D, E, F are representing principal stresses $\sigma_1, \sigma_2, \sigma_3$ on the σ axis; G and H are the centers of circles on FE and ED as diameters; the angels FGK and LHD are $2\theta_1$, $2\theta_3$, respectively; and P is the intersection of circle of center H passing through K with a circle of center G passing through L. If P lies below the line ABC sliding cannot take place on the plane.
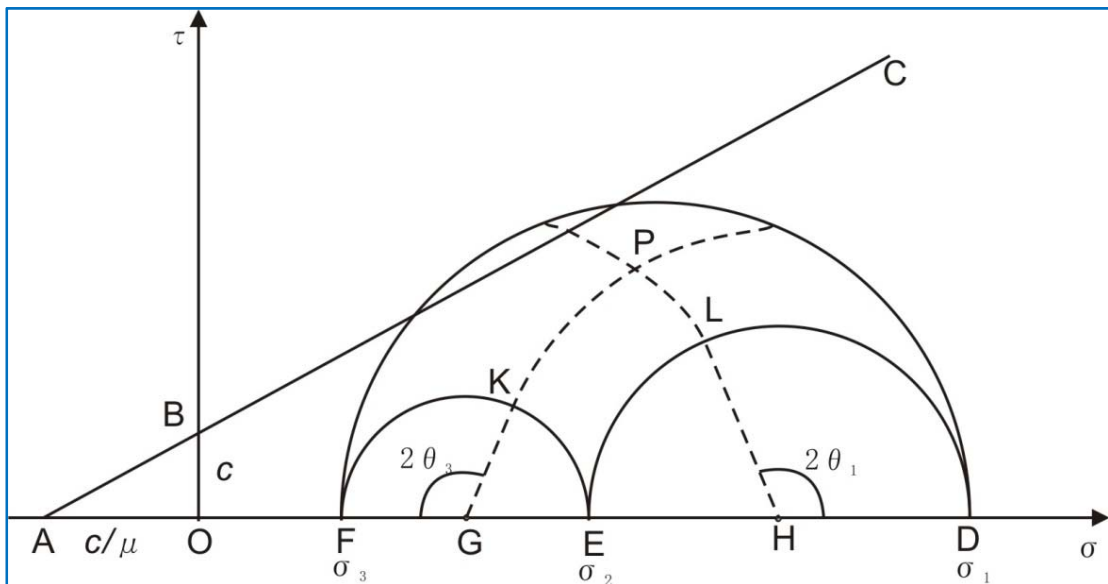

Fig.B.1 Determination of the Possibility of Sliding of Natural fractures Using the Mohr Diagram.

In the work of Jaeger and Rosengren (1969), an equal area projection showing the method of plotting the normal P to a plane was used to show the failed range of orientations of

natural fractures. As shown in the Fig.2 (Jaeger and Rosengren, 1969), the angles θ and ϕ (which are θ_1, θ_3 in our study), measured along great circles form σ_1, σ_3, respectively, determine the position of the normal P of natural fractures on the projection. In the special case, slip can occur on any plane only if its normal lies in one of the four lobes $Q_1R_1S_1$, etc. For this given case, the parameters used are:

$\sigma_3 / \sigma_1 = 0.1$;

$\sigma_2 / \sigma_1 = 0.3$;

And $\mu = 2/3$, assuming the pore pressure and cohesion are both zero.
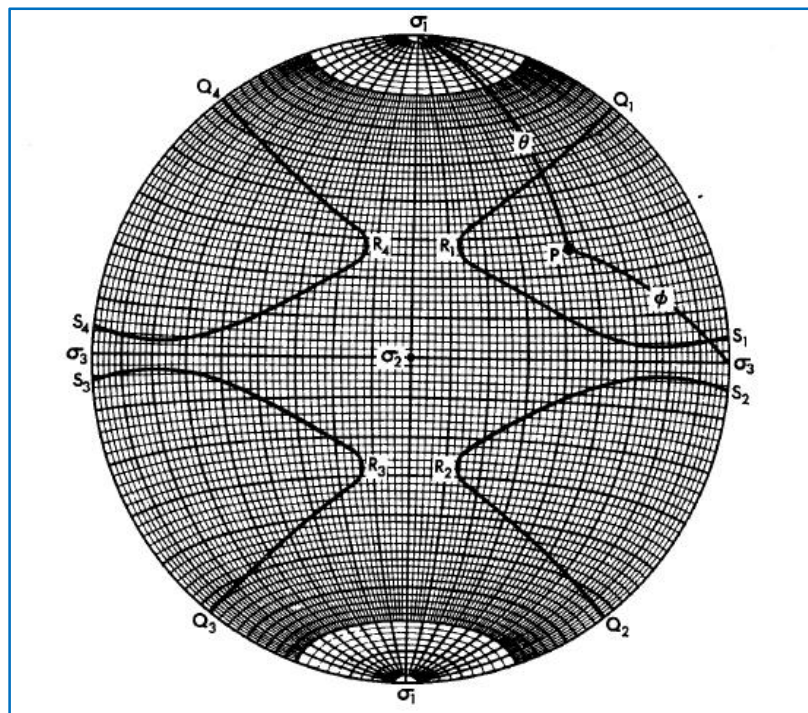

Fig.B.2 Equal Area Projection for Sliding Area of Natural fractures (Jaeger and Rosengren, 1969).

To program for this study, the following procedure is used.

In Fig.B.2, the plot is shown by latitude and longitude. In this study, we use angle α, β to represent latitude and longitude in the figure. The first step is to get the relations between α, β and θ_1, θ_3 which can be deduced by the following procedure.
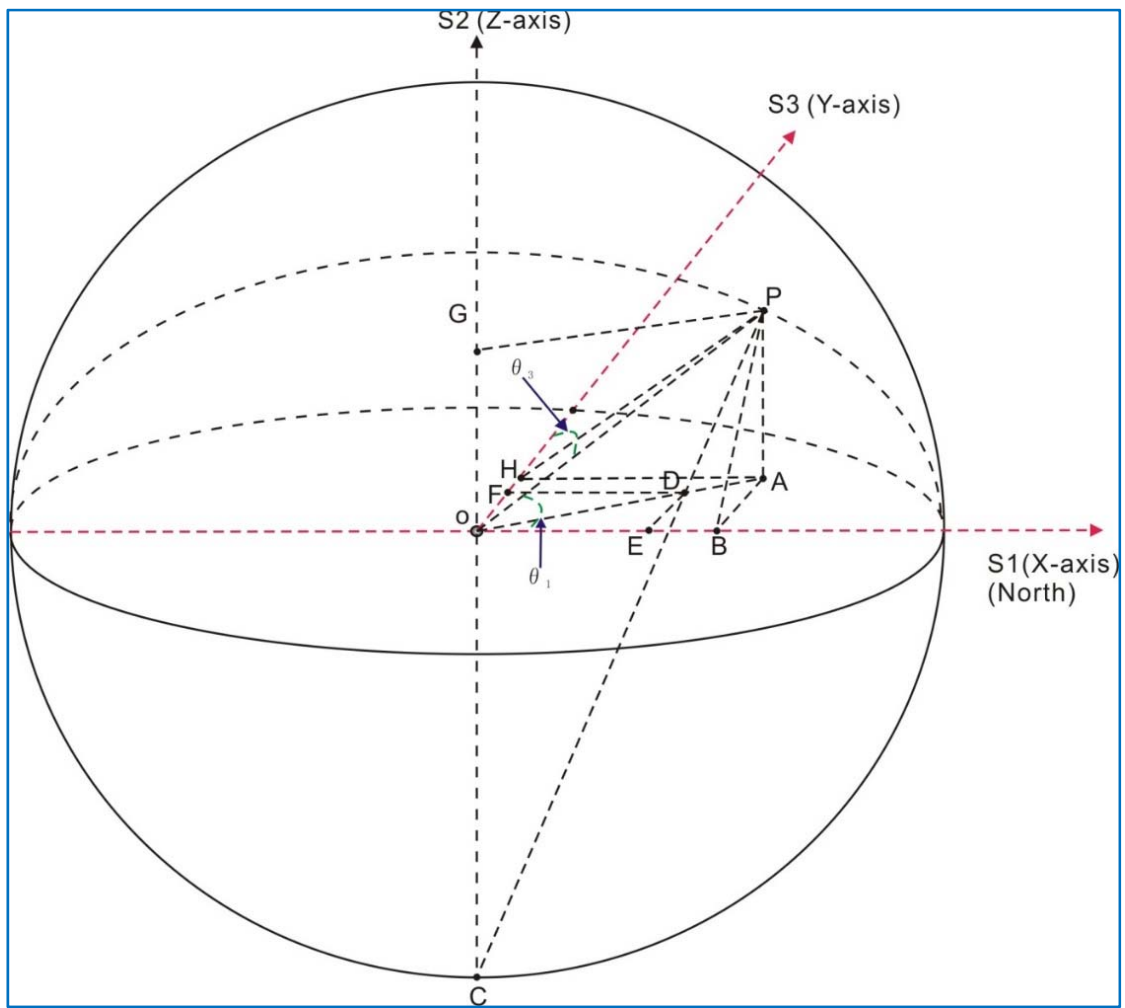

Fig.B.3 the Projection for Normal P.

As shown in Fig.B.3, OP is the normal of any a joint plane, and A is the vertical projection on the horizontal plane, point D is the Projection of P on the Wulff Net. Assuming the X-

113

axis and Y-axis are the direction of σ_1, σ_3, respectively. The angle POB here is the latitude α (here assume X-axis direction is North Pole for the convenience of analysis), and the angle BPA is the longitude β. The angle POX and POY are θ_1, θ_3 respectively. The right angles in Fig.3 include angle: PAO, PAB, PBO, DEO, DFO, and PGO. The PH is the vertical line to the Y-axis form point P.

From Fig.B.3, we can see that the angle POB and POX are the same angle, that is:

$$\theta_1 = \alpha \tag{B.2}$$

That's way we can directly read the angle θ from Fig.B.2 with latitude.

Now, assuming the radius of the ball in Fig.B.3 is r, and we can get:

$$PB = r \times \sin(\alpha) \tag{B.3}$$

$$OB = r \times \cos(\alpha) \tag{B.4}$$

$$BA = PB \times \sin(\beta) = r \times \sin(\alpha) \times \sin(\beta) \tag{B.5}$$

$$PA = PB \times \cos(\beta) = r \times \sin(\alpha) \times \cos(\beta) \tag{B.6}$$

In the rectangle OHAB, we get:

$$OH = BA = r \times \sin(\alpha) \times \sin(\beta) \tag{B.7}$$

So the angle POY, also θ_3 is the same angle with angle POH, therefore:

114

$$\cos(\theta_3) = \frac{OH}{OP} = \frac{r \times \sin(\alpha) \times \sin(\beta)}{r} = \sin(\alpha) \times \sin(\beta) \qquad \text{(B.8)}$$

Equations B.2 and B..8 give the relations between α, β and θ_1, θ_3.

In the program, we need to know the X-Y coordinates of the projection of point P so that we can plot at that point. In the following is the deduction of the X-Y coordinates of projection point D.

From Fig. B.3, we can see that the point D (x, y) can be given:

$$\begin{aligned} x &= DF = OE \\ y &= DE = OF \end{aligned} \qquad \text{(B.9)}$$

Because line PA is vertical to the horizontal plane, it is parallel to Z-axis, and the line PG is vertical to OZ, the length of PA is equal to the length of OG. Therefore, we can get:

$$OG = PA = PB \times \cos(\beta) = r \times \sin(\alpha) \times \cos(\beta) \qquad \text{(B.10)}$$

In the right-angled triangle OBA, the length of OA:

$$\begin{aligned} OA &= \sqrt{OB^2 + BA^2} \\ &= \sqrt{[r \times \cos(\alpha)]^2 + [r \times \sin(\alpha) \times \sin(\beta)]^2} \\ &= r\sqrt{1 - \sin^2(\alpha) \times \cos^2(\beta)} \end{aligned} \qquad \text{(B.11)}$$

In the rectangle PGOA, we get:

$$GP = OA = r\sqrt{1 - \sin^2(\alpha) \times \cos^2(\beta)} \qquad \text{(B.12)}$$

In the right-angled triangle PGC, the length of OD is parallel to GP, and there is a relation:

$$\frac{OD}{GP} = \frac{OC}{CG} = \frac{r}{r+OG} = \frac{1}{1+\sin(\alpha)\times\cos(\beta)} \tag{B.13}$$

So:

$$OD = GP\frac{OC}{CG} = \frac{r\sqrt{1-\sin^2(\alpha)\times\cos^2(\beta)}}{1+\sin(\alpha)\times\cos(\beta)} \tag{B.14}$$

In the triangle OBA, we have the relations:

$$\begin{aligned}\frac{DE}{BA} &= \frac{OD}{OA}\\[4pt]\frac{OE}{OB} &= \frac{OD}{OA}\end{aligned} \tag{B.15}$$

So:

$$\begin{aligned}DE &= BA\frac{OD}{OA}\\[4pt]&= \frac{r\sqrt{1-\sin^2(\alpha)\times\cos^2(\beta)}}{1+\sin(\alpha)\times\cos(\beta)}\frac{r\times\sin(\alpha)\times\sin(\beta)}{r\sqrt{1-\sin^2(\alpha)\times\cos^2(\beta)}}\\[4pt]&= \frac{r\times\sin(\alpha)\times\sin(\beta)}{1+\sin(\alpha)\times\cos(\beta)}\end{aligned} \tag{B.16}$$

And:

116

$$OE = OB\frac{OD}{OA}$$

$$= \frac{r\sqrt{1-\sin^2(\alpha)\times\cos^2(\beta)}}{1+\sin(\alpha)\times\cos(\beta)}\frac{r\times\cos(\alpha)}{r\sqrt{1-\sin^2(\alpha)\times\cos^2(\beta)}} \qquad\text{(B.17)}$$

$$= \frac{r\times\cos(\alpha)}{1+\sin(\alpha)\times\cos(\beta)}$$

Combing equations B.16 and 17 into 9, the coordinates of projection point D can be given:

$$x = DF = OE = \frac{r\times\cos(\alpha)}{1+\sin(\alpha)\times\cos(\beta)}$$

$$y = DE = OF = \frac{r\times\sin(\alpha)\times\sin(\beta)}{1+\sin(\alpha)\times\cos(\beta)} \qquad\text{(B.18)}$$

In fact, from the Fig. B.2, we can see that the north is Y direction; therefore, in the program, we used exchanged expressions for the coordinates.

The equations for calculation of normal and shear stresses on a plane were given by Jaeger and Cook (1979) as the following:

$$\sigma_n = l^2\sigma_1 + m^2\sigma_2 + n^2\sigma_3$$

$$\tau = \sqrt{l^2 m^2 (\sigma_1 - \sigma_2)^2 + n^2 m^2 (\sigma_3 - \sigma_2)^2 + l^2 n^2 (\sigma_3 - \sigma_1)^2} \qquad\text{(B.19)}$$

In which, l, m, and n are direction cosines for a given plane to the direction of the three principal stresses.

In order to compare with the work of Jaeger and Rosengren (1969), and verify the calculations and program in our work, the special cases are investigated.
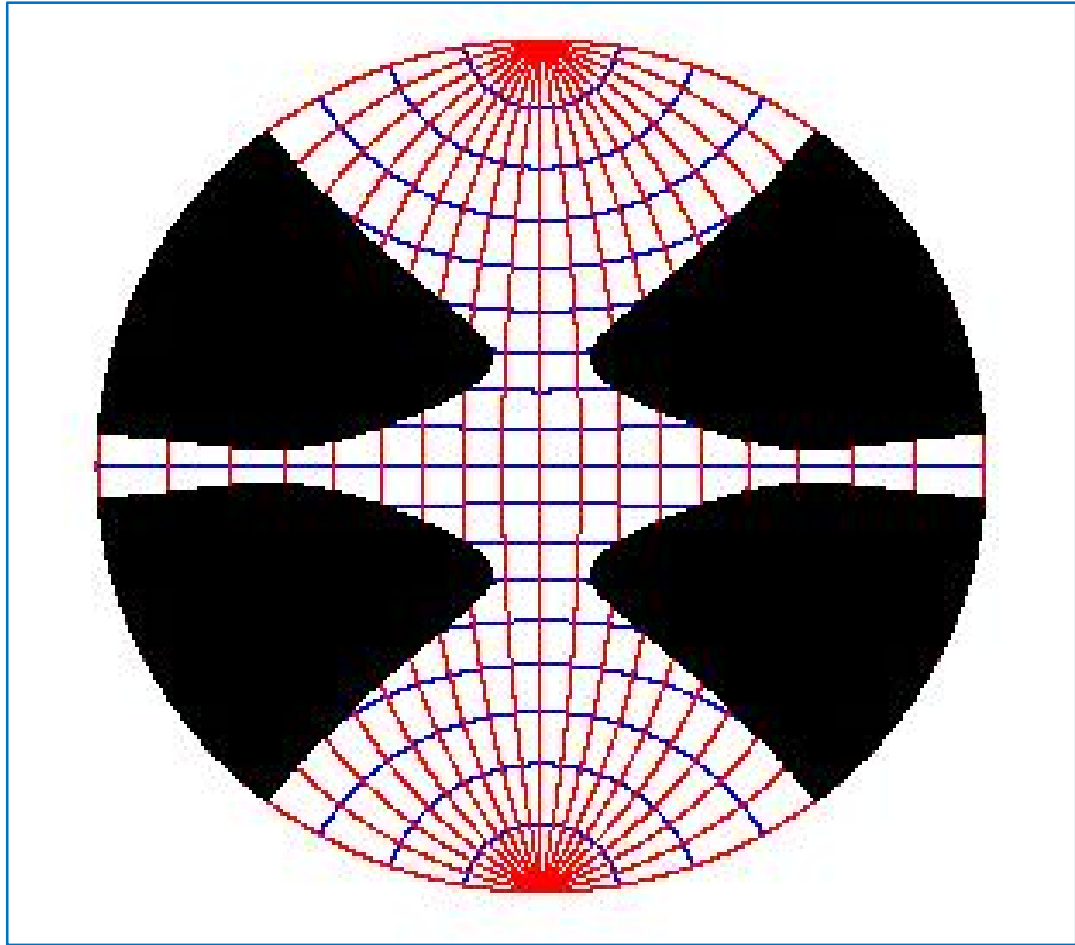
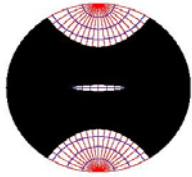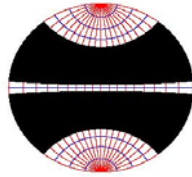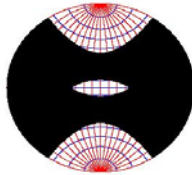Fig. B.4 Equal Area Projection for Sliding Area of Natural fractures.
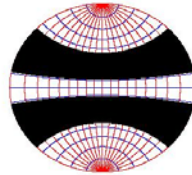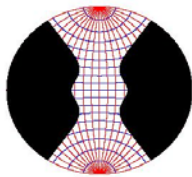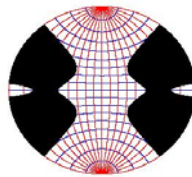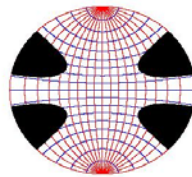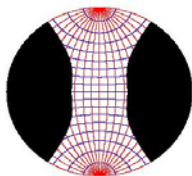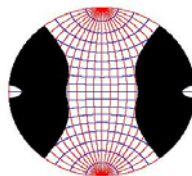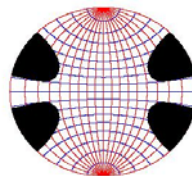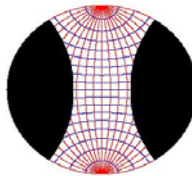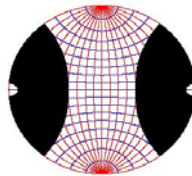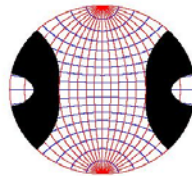
(σ_3/σ_1=0.1, σ_2/σ_1=0.3, and μ=2/3, P_p=0, c=0)

The first example is for the case of σ_3/σ_1=0.1, σ_2/σ_1=0.3, and μ=2/3, by assuming

the pore pressure and cohesion are both zero. The Fig. B.4 is the equal area projection for
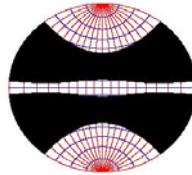
sliding area of natural fractures for this case, and it has exactly the same sliding area with

what Jaeger did as shown in Fig.B.2.

Furthermore, in this work, we get the sensitivity analysis on in-situ stresses and friction

coefficient. The results are shown in Table. B.1 and Table B.2, and those figures can also
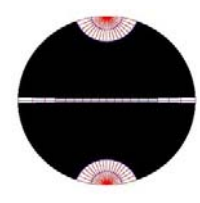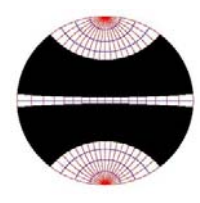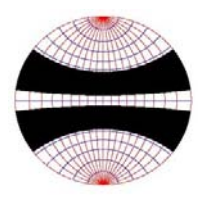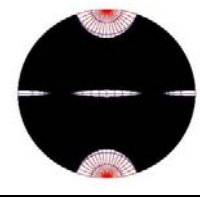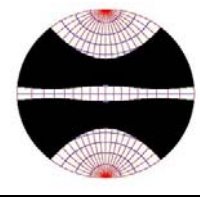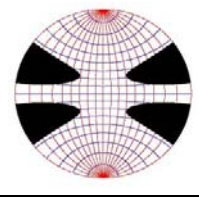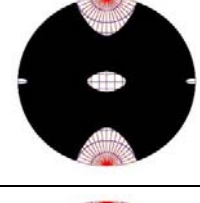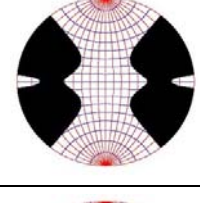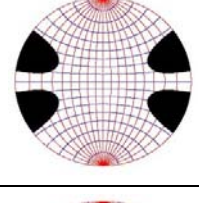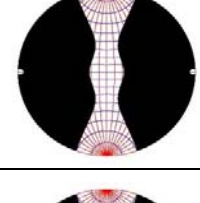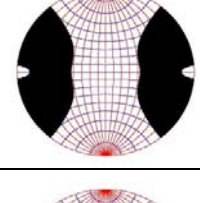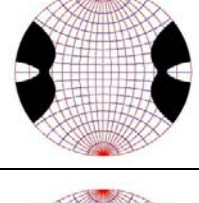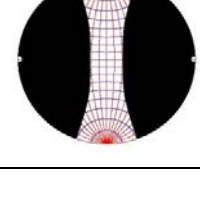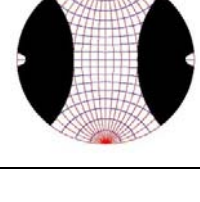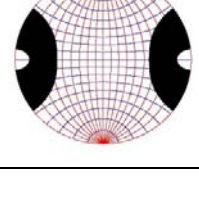
be compared with previous work (Jaeger and Rosengren, 1969).

Table.B.1 Equal Area Projection Showing the Sliding Area for μ =2/3

	σ_3 / σ_1 =0.0	σ_3 / σ_1 =0.1	σ_3 / σ_1 =0.2
σ_2 / σ_1 =0.1			
σ_2 / σ_1 =0.2			
σ_2 / σ_1 =0.4			
σ_2 / σ_1 =0.6			
σ_2 / σ_1 =0.8			

Through the compare between our work and the previous work (Jaeger and Rosengren, 1969), it gives a demonstration to our calculations and programs. After this verification, we applied our work on a special case to check its application.

119

Table.B.2 Equal Area Projection Showing the Sliding Area for σ_3/σ_1 =0.1

	μ =0.33	μ =0.67	μ =1.0
σ_2/σ_1 =0.1			
σ_2/σ_1 =0.2			
σ_2/σ_1 =0.4			
σ_2/σ_1 =0.6			
σ_2/σ_1 =0.8			

Some research works have been done on New Albany shale and according to the data from J Ray Clark well in Christian County, KY, we assume that the principal stresses are σ_1 =2500 psi, σ_2 =2200 psi, σ_3 =2000 psi, and pore pressure P_p=1800 psi with μ =0.6, and cohesion zero. Then, the equal area projection for the sliding range is given in Fig.B.5.
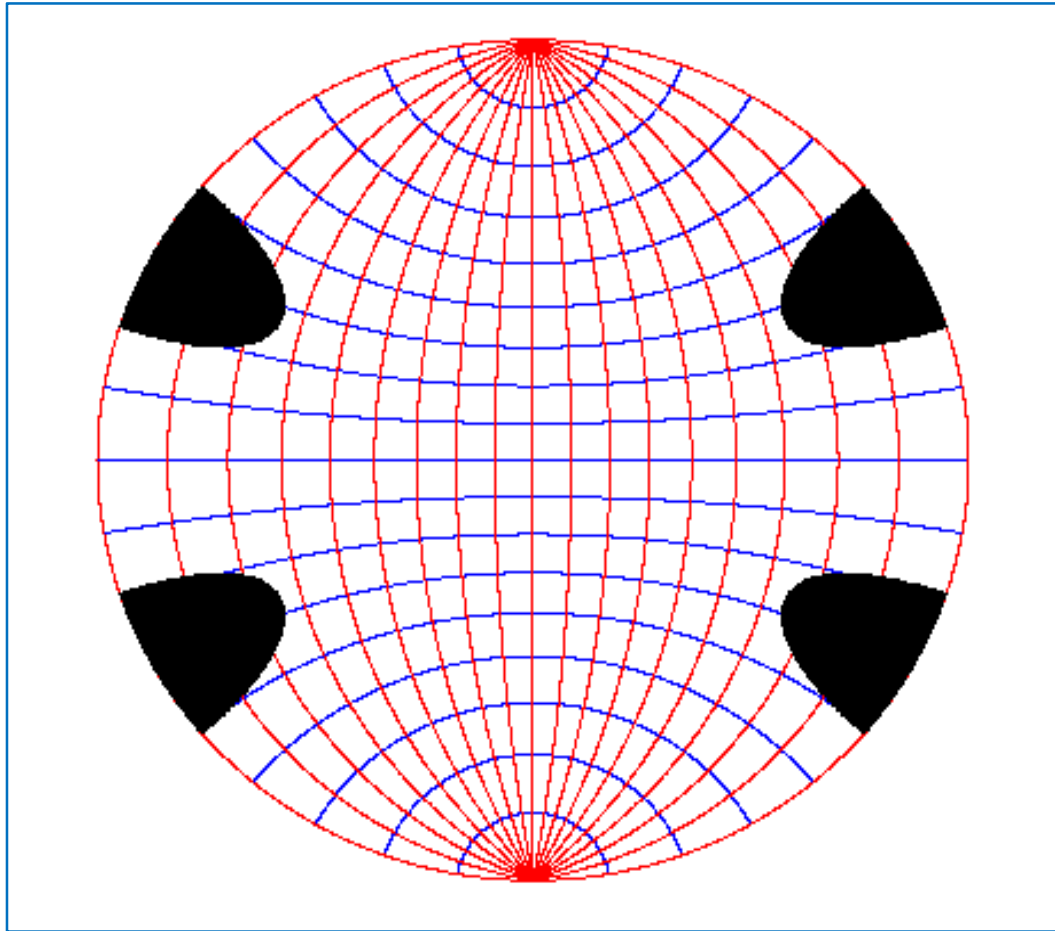
Fig.B.5 Equal Area Projection for Sliding Area of Natural fractures for New Albany Shale.

From Fig.B.5, we can see that with the assumed parameters, if the normal of the weakness plane lies in one of the four black areas, the slip can occur.

2. Pore Pressure Effects on Sliding of Natural fractures

When injection into a well, the pore pressure effects on the sliding of natural fractures are more of interest. In jointed rocks, the effects of increasing pore pressure on rock failure are

well documented in the literature (Jaeger&Cook, 1979). A structural permeability diagram can be used to show the ΔP required to reactivate fabrics of different orientations (Mildren et al. 2002; Nelson et al. 2007).

Here, in this study, we set up the program for this structural permeability diagram and verified it with the work of Mildren et al. 2002 and Nelson et al. 2007. Finally, we applied this program for the prediction of ΔP required to reactivate fabrics of different orientation in the well J Ray Clark in Christian County, KY.

First, the procedure for setting up the structural permeability diagram is researched and programmed. As one case we can see from Fig.B.6 in the following (Nelson et al. 2007), the structure permeability diagram is set up based on the dip angle δ and the angle from north to the dip direction of the natural fractures φ (clockwise positive). Here, the dip angle refers to the angle between the joint plane and the horizontal plane; and the dip direction is really vertical to the strike of the joint.

To get the structural permeability diagram, the direction cosines of the principal stresses should be found first using the known dip angle and dip direction angle.
Goodman (1989) gave the expressions for finding the direction cosines for a given plane relative to the X, Y and Z coordinates. However, in his work, he used the rise angle and the counterclockwise angle from X-axis to the horizontal projection the normal of the joint, instead of dip angle δ and the dip direction angle φ. The relations between those angles are

122

easily found from Fig. B.3, and this gives the direction cosines with dip angle δ and the dip

direction angle φ:
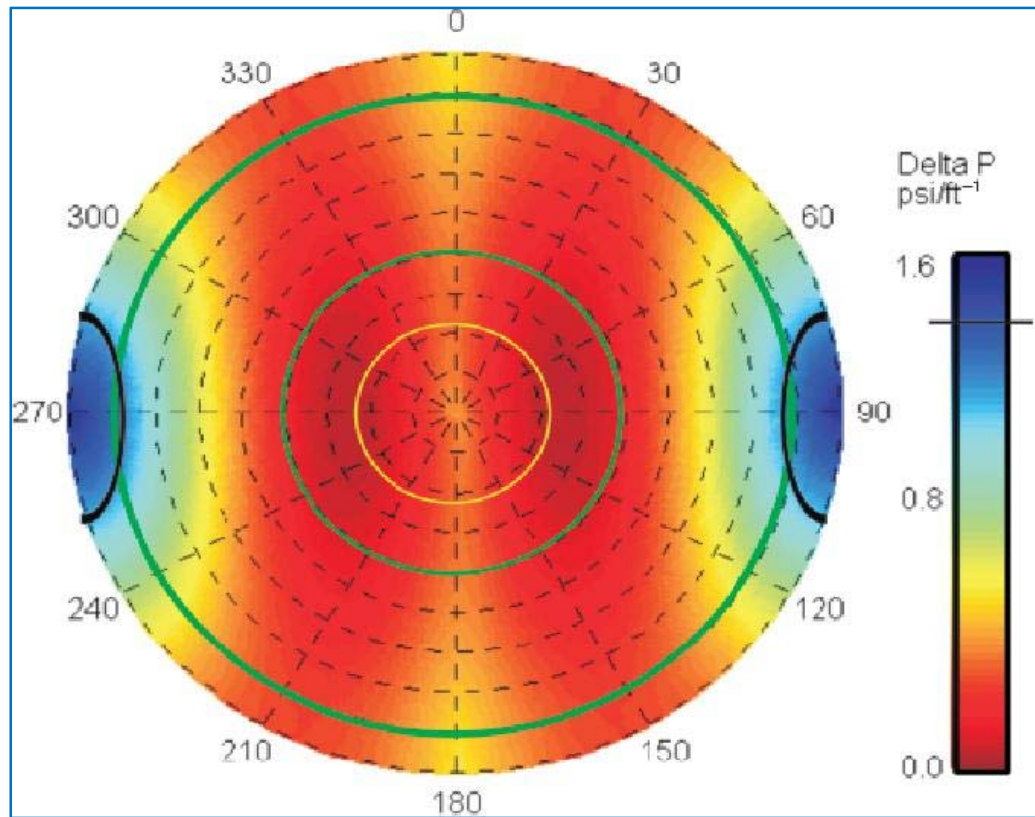
Fig.B.6 Structural permeability diagram showing the orientations of geological weaknesses that may be reactivated during fracture stimulation treatments at high treating pressures in the Cooper Basin (Nelson et al. 2007).

$$d_x = \cos(90 - \delta) \times \cos(90 - \varphi)$$
$$d_y = \cos(90 - \delta) \times \sin(90 - \varphi) \qquad \text{(B.20)}$$
$$d_z = \sin(90 - \delta)$$

In which, d_x, d_y, and d_z are direction cosines for a given plane to the direction of the three

stresses $\sigma_x, \sigma_y, \sigma_z$ on X, Y and Z coordinates (assuming they are principal stresses, but

don't know which is maximum and minimum). Note here they are not the direction cosines

to the principal stresses; therefore, before using Eqn. B.19, the corresponding values of

$\sigma_1, \sigma_2, \sigma_3$ to $\sigma_x, \sigma_y, \sigma_z$ should be found and the also their direction cosines. This can be

easily realized in the program. Sometimes, the X direction is not in the exact east. In our

program, an angle ω between the direction of σ_x and the East direction is added to adjust

the excursion.

After the confirmation of the three principal stresses and their direction cosines, the normal

and shear stress on the joint plane can be found using Eqn. B.19.

Finally, the required pore pressure to reactivate the joint plane is given by (Mildren et al.

2005).

$$P = \sigma_n + (c - \tau) / \mu \qquad (B.21)$$

If the effective treating pressure is ΔP, we have:

$$\Delta P = P - P_p \qquad (B.22)$$

In which P_p is the original in-situ pore pressure.

A FORTRAN program is used to calculate the required effective pore pressure and plot the

structural permeability diagram.

To verify the calculation and program, we first compared the special case given by Nelson

et al. (2007) for Cooper Basin.
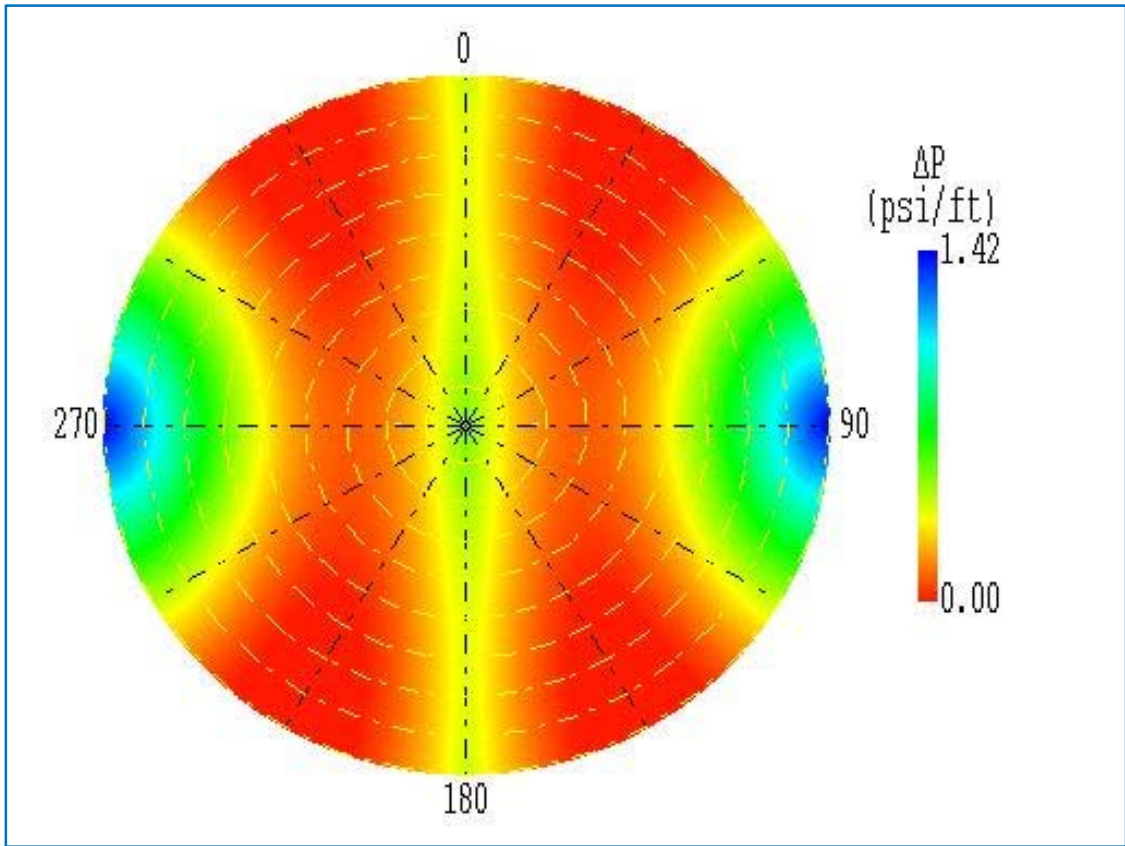
Fig.B.7 Structural permeability diagram showing the orientations of geological weaknesses that may be reactivated during fracture stimulation treatments at high treating pressures in the Cooper Basin (FORTRAN Program).

In Fig.B.7, the parameters we used are listed in Table. B.3.

Table. B.3 In-Situ Conditions for Cooper Basin (Nelson et al. 2007)

Parameter	Value	Unit
Depth (D):	9800	ft
Minimum horizontal stress (S_h) gradient:	0.84	psi/ft
Maximum horizontal stress (S_H) gradient:	1.85	psi/ft
Vertical Stress (S_v) gradient:	0.95	psi/ft
Initial reservoir pressure (P_o) gradient:	0.433	psi/ft

By comparing Fig.B.7 with Fig.B.6, we found two main differences.

One is the maximum effective treating pressure, there are about 0.2 psi/ft difference between them. This may be caused by different calculation process or some adjustments in their software or program. If we take a special point, say dip angle 90 degree and dip direction 90 degree, for example, the calculated required treating pressure from equation should be the maximum in-situ stresses, which is 1.85 psi/ft, and the effective treating pressure should be 1.42 psi/ft.

The other difference is on the distribution of the minimum required treating pressure. In Fig.B.6, they are distributed in the lower dips around the center, while in Fig.B.7, they are distributed in the four parts like 30º N dip direction and 90 dip angles. Through calculations on special points, if using our equations, the distributions should be like Fig.B.7 not Fig.B.6.

In order to further verify the program before application, we programmed in Mathematica in case for program mistakes. However, the result Fig. B.8 is exactly the same with Fig. B.7.
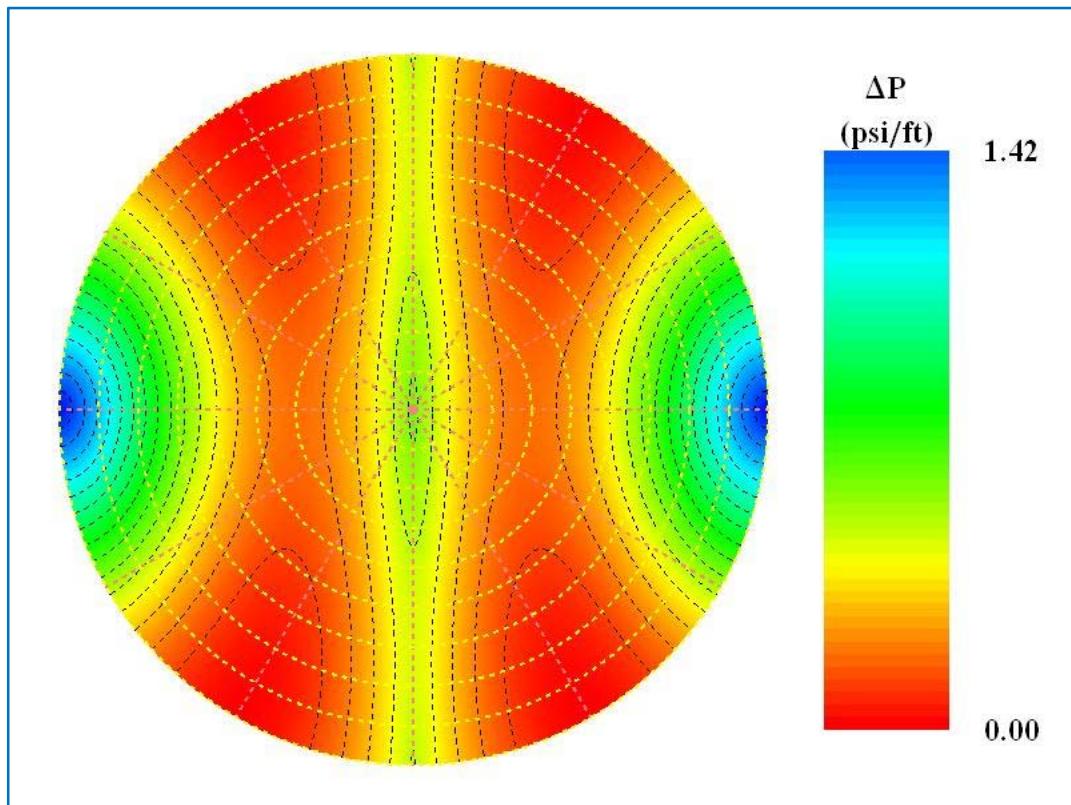
Fig.B.8 Structural permeability diagram (Compare with Fig.B.7 and B.6).

From the equal pressure lines (dashed black lines), we can clearly see the distributions of minimum treating pressures. And this is coincidence with Fig. B.7.

APPENDIX C

2-D STRESSES REDISTRIBUTION DEDUCTION

For the convenience of analysis and programming, the stresses around a hydraulically induced fracture are expressed in the elliptical coordinates system as shown in Fig. C.1. Elliptic coordinates are a two-dimensional orthogonal coordinate system in which the coordinate lines are confocal ellipses and hyperbolae. The two foci are generally taken to be fixed at $-L_f$ and L_f (fracture half length) respectively on x-axis of the Cartesian coordinate system.
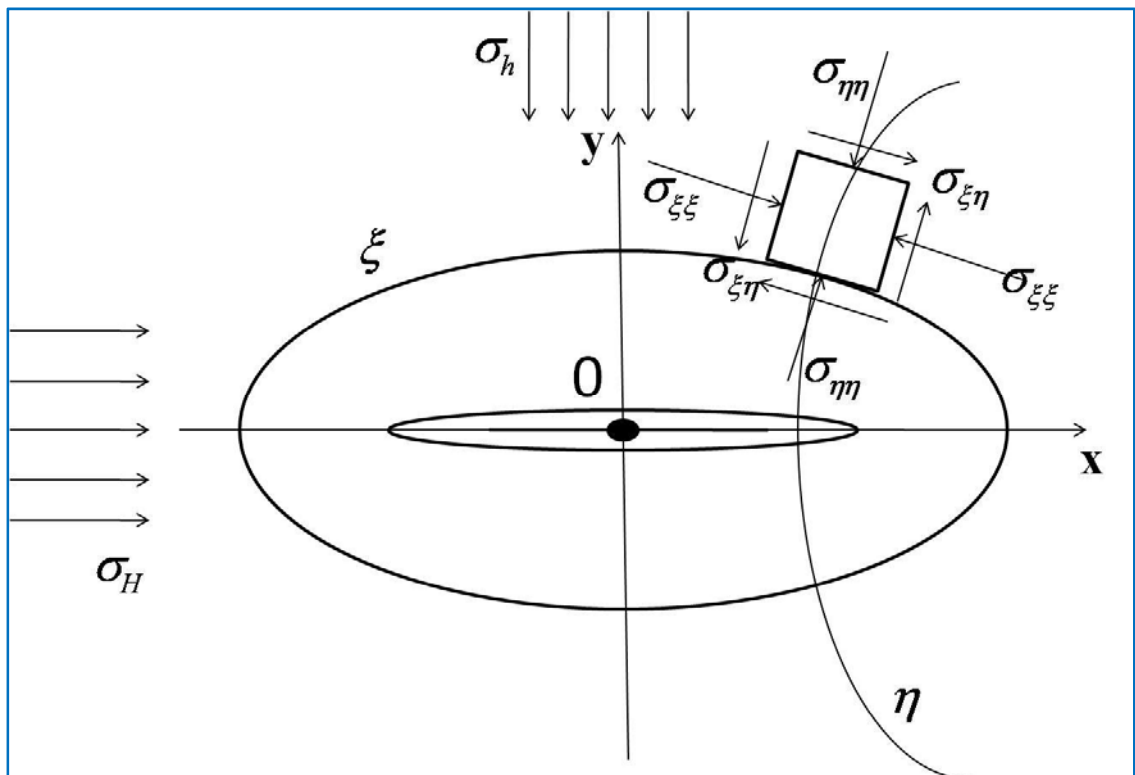
Fig.C.1 Stresses in Elliptical Coordinates System.

In the following analysis for the induced stresses from pore pressure, temperature variations and fracture compression are cited from relative references and all expressions are converted into the same Cartesian coordinate system for the convenience of calculations and programming.

1. 2-D Poroelastic Stresses

The stresses induced by the pore pressure variation around a hydraulic fracture were given by Koning (1985).   And the analytical fracture propagation model was constructed by him with the following assumptions.

1) A vertical fracture confined to the pay zone with fixed height and the geometry of PKN model extends laterally from a single well to an infinite reservoir.

2) The fracture has an infinite conductivity and the fluid pressure along the fracture length keeps constant.

3) The total leak-off rate equals to the constant injection rate.

4) The fracture propagates slow enough that the pressure distribution around the fracture behaves as quasi steady state. And the transient pressure distribution far away from the fracture moves radially outwards into the reservoir.

5) The fluid flow system can be separated into different elliptic zones as shown in Fig.3.1.

With the assumptions the stresses at any point (ξ, η) in the pressure affected region $0 \leq \xi \leq$

ξ_2 surrounding the fracture is solving the poroelastic stress-strain relations and are given by (Koning, 1985):

$$\frac{(1-v)}{EJ}\Delta\sigma_{\xi p}^{(m)} = \frac{1}{g^2}\Phi_{\xi\xi}^{(m)} - \frac{L_f^2}{2}\frac{\sinh 2\xi}{g^4}\Phi_{\xi}^{(m)} + \frac{L_f^2}{2}\frac{\sin 2\eta}{g^4}\Phi_{\eta}^{(m)} + \Delta p^{(m)}(\xi) \tag{C.1}$$

$$\frac{(1-v)}{EJ}\Delta\sigma_{\eta p}^{(m)} = \frac{1}{g^2}\Phi_{\eta\eta}^{(m)} + \frac{L_f^2}{2}\frac{\sinh 2\xi}{g^4}\Phi_{\xi}^{(m)} - \frac{L_f^2}{2}\frac{\sin 2\eta}{g^4}\Phi_{\eta}^{(m)} + \Delta p^{(m)}(\xi) \tag{C.2}$$

$$\frac{(1-v)}{EJ}\Delta\sigma_{\xi\eta p}^{(m)} = \frac{1}{g^2}\Phi_{\xi\eta}^{(m)} - \frac{L_f^2}{2}\frac{\sin 2\eta}{g^4}\Phi_{\xi}^{(m)} - \frac{L_f^2}{2}\frac{\sinh 2\xi}{g^4}\Phi_{\eta}^{(m)} \tag{C.3}$$

The linear coefficient of pore pressure expansion J is used as:

$$J = \frac{(1-2v)}{E} - \frac{c_{gr}}{3} \tag{C.4}$$

And where the superscript (m) is associated with the subregions:

$$\begin{aligned}m &= 1;\ \xi_1 \le \xi < \xi_2\\ &= 2;\ \xi_0 \le \xi < \xi_1\\ &= 3;\ 0 \le \xi < \xi_0\end{aligned} \tag{C.5}$$

And:

$$\Phi_{\xi\xi}^{(m)} = -\frac{L_f^2}{2}\Delta p(\xi)\cosh 2\xi + \cos 2\eta (4A_1^{(m)}e^{-2\xi} + 4A_2^{(m)}\cosh 2\xi) \tag{C.6}$$

$$\Phi_{\eta\eta}^{(m)} = \cos 2\eta[\frac{L_f^2}{2}\Delta p(\xi) - 4A_1^{(m)}e^{-2\xi} - 4A_2^{(m)}\cosh 2\xi] \tag{C.7}$$

$$\Phi_{\xi\eta}^{(m)} = \sin 2\eta [\frac{L_f^2}{4}\frac{\partial[\Delta p(\xi)]}{\partial \xi} + 4A_1^{(m)}e^{-2\xi} - 4A_2^{(m)}\sinh 2\xi] \qquad (C.8)$$

$$\Phi_{\eta}^{(m)} = \sin 2\eta [\frac{L_f^2}{4}\Delta p(\xi) - 2A_1^{(m)}e^{-2\xi} - 2A_2^{(m)}\cosh 2\xi] \qquad (C.9)$$

$$\Phi_{\xi}^{(m)} = -\frac{L_f^2}{2}\int_0^{\xi}[\Delta p(\xi)\cosh 2\xi]d\xi + \cos 2\eta[-\frac{L_f^2}{8}\frac{\partial[\Delta p(\xi)]}{\partial \xi}$$
$$- 2A_1^{(m)}e^{-2\xi} + 2A_2^{(m)}\sinh 2\xi] \qquad (C.10)$$

In which:

$$\int_0^{\xi}[\Delta p(\xi)\cosh 2\xi]d\xi = \frac{1}{2}\Delta p(\xi)\sinh 2\xi - \frac{1}{4}\frac{\partial[\Delta p(\xi)]}{\partial \xi}[\cosh 2\xi - 1]$$
$$\frac{\partial[\Delta p(\xi)]}{\partial \xi} = -\frac{i_w}{2\pi h\lambda_m} \qquad (C.11)$$

The pore pressure variations are given:

$$\Delta p(\xi) = \Delta p^{(1)}(\xi); \xi_1 \le \xi < \xi_2$$
$$= \Delta p^{(2)}(\xi); \xi_0 \le \xi < \xi_1$$
$$= \Delta p^{(3)}(\xi); 0 \le \xi < \xi_0 \qquad (C.12)$$
$$= 0; \xi \ge \xi_2$$

And:

$$A_1^{(3)} = \frac{i_w L_f^2}{32\pi h}[\frac{1}{\lambda_3}] \qquad (C.13)$$

$$A_1^{(2)} = A_1^{(3)} + \frac{i_w L_f^2}{32\pi h}[\frac{1}{\lambda_2} - \frac{1}{\lambda_3}]\cos h 2\xi_0 \qquad (C.14)$$

131

$$A_1^{(1)} = A_1^{(2)} + \frac{i_w L_f^2}{32\pi h}[\frac{1}{\lambda_1} - \frac{1}{\lambda_2}]\cos h2\xi_1 \tag{C.15}$$

$$A_2^{(1)} = -\frac{i_w L_f^2}{32\pi h}[\frac{1}{\lambda_1}]e^{-2\xi_2} \tag{C.16}$$

$$A_2^{(2)} = A_2^{(1)} + \frac{i_w L_f^2}{32\pi h}[\frac{1}{\lambda_1} - \frac{1}{\lambda_2}]e^{-2\xi_1} \tag{C.17}$$

$$A_2^{(3)} = A_2^{(2)} + \frac{i_w L_f^2}{32\pi h}[\frac{1}{\lambda_2} - \frac{1}{\lambda_3}]e^{-2\xi_0} \tag{C.18}$$

While in the pressure unaffected region $\xi \geq \xi_2$, the stress changes:

$$\frac{(1-v)}{EJ}\Delta\sigma_{\xi p}^{(0)} = \frac{1}{g^2}\Phi_{\xi\xi}^{(0)} - \frac{L_f^2}{2}\frac{\sinh 2\xi}{g^4}\Phi_{\xi}^{(0)} + \frac{L_f^2}{2}\frac{\sin 2\eta}{g^4}\Phi_{\eta}^{(0)} \tag{C.19}$$

$$\frac{(1-v)}{EJ}\Delta\sigma_{\eta p}^{(0)} = \frac{1}{g^2}\Phi_{\eta\eta}^{(0)} + \frac{L_f^2}{2}\frac{\sinh 2\xi}{g^4}\Phi_{\xi}^{(0)} + \frac{L_f^2}{2}\frac{\sin 2\eta}{g^4}\Phi_{\eta}^{(0)} \tag{C.20}$$

$$\frac{(1-v)}{EJ}\Delta\sigma_{\xi\eta p}^{(0)} = \frac{1}{g^2}\Phi_{\xi\eta}^{(0)} - \frac{L_f^2}{2}\frac{\sin 2\eta}{g^4}\Phi_{\xi}^{(0)} - \frac{L_f^2}{2}\frac{\sinh 2\xi}{g^4}\Phi_{\eta}^{(0)} \tag{C.21}$$

Where the superscript (0) stands for the region with zero pressure change.

And the constants are:

$$\Phi_{\xi\xi}^{(0)} = 4A_3^{(0)}e^{-2\xi}\cos 2\eta; \qquad \Phi_{\eta\eta}^{(0)} = -4A_3^{(0)}e^{-2\xi}\cos 2\eta \tag{C.22}$$

$$\Phi_{\xi\eta}^{(0)} = 4A_3^{(0)}e^{-2\xi}\sin 2\eta; \qquad \Phi_{\eta}^{(0)} = -2A_3^{(0)}e^{-2\xi}\sin 2\eta \tag{C.23}$$

132

$$\Phi_{\xi}^{(0)} = -2A_3^{(0)}e^{-2\xi}\cos 2\eta + A_4^{(0)}; \quad A_3^{(0)} = A_1^{(1)} - \frac{i_w L_f^2}{32\pi h\lambda_1}\cosh 2\xi_2 \tag{C.24}$$

$$A_4^{(0)} = -\frac{L_f^2}{2}\int_0^{\xi_2}[\Delta p(\xi)\cosh 2\xi]d\xi \tag{C.25}$$

The listed equations above are in elliptical coordinates system, and Koning (1985) gave

transformation of the pore pressure induced stresses from elliptic coordinate system into

the *x-y* coordinates system by the following equations (Koning, 1985).

$$\Delta\sigma_{px} = \Delta\sigma_{\xi p}g^2$$
$$\Delta\sigma_{py} = \Delta\sigma_{\eta p}g^2 \tag{C.26}$$
$$\Delta\sigma_{pxy} = \Delta\sigma_{\xi\eta p}g^2$$

In which the metric tensor *g* is given:

$$g = \sqrt{\frac{L_f^2}{2}(\cosh 2\xi - \cos 2\eta)} \tag{C.27}$$

In our work, we deduced the stresses transformation between these two coordinate

systems and the detailed deducing process can be found in Ge, 2009.

$$\begin{aligned}\sigma_{yy} &= \sigma_{\eta\eta}\cos 2\theta + \sigma_{\xi\eta}\sin 2\theta + (\sigma_{\xi\xi} + \sigma_{\eta\eta})\sin^2\theta \\ &= \sigma_{\eta\eta} + \sigma_{\xi\eta}\sin 2\theta + (\sigma_{\xi\xi} - \sigma_{\eta\eta})\sin^2\theta\end{aligned} \tag{C.28}$$

$$\sigma_{xx} = \sigma_{\xi\xi} - \sigma_{\xi\eta}\sin 2\theta - (\sigma_{\xi\xi} - \sigma_{\eta\eta})\sin^2\theta \tag{C.29}$$

$$\sigma_{xy} = (\sigma_{\xi\eta} - \frac{1}{2}(\sigma_{yy} - \sigma_{xx})\sin 2\theta)/\cos 2\theta \tag{C.30}$$

In which θ is given by:

$$\tan\theta = \frac{y}{x} = \frac{c\sinh\xi\sin\eta}{c\cosh\xi\cos\eta} \tag{C.31}$$

2. 2-D Thermoelastic Stresses

In this study, the poroelastic and thermoelastic induced stresses are still estimated with the method from Perkins and Gonzales (1985):

$$\frac{(1-v)\Delta\sigma_{Ty}}{E\beta\Delta T} = \frac{(b_0/a_0)}{1+(b_0/a_0)} + \left[\frac{1}{1+(b_0/a_0)}\right] \tag{C.32}$$
$$\left(1/\left\{1+\frac{1}{2}\left[1.45(\frac{h}{2b_0})^{0.9}+0.35(\frac{h}{2b_0})^2\right]\left[1+(\frac{b_0}{a_0})^{0.774}\right]\right\}\right)$$

$$\frac{(1-v)\Delta\sigma_{Tx}}{E\beta\Delta T} = \frac{1}{1+(b_0/a_0)} + \left[\frac{(b_0/a_0)}{1+(b_0/a_0)}\right] \tag{C.33}$$
$$\left(1/\left\{1+\left[1.45(\frac{h}{2b_0})^{0.9}+0.35(\frac{h}{2b_0})^2\right]\left[1+(1-\frac{b_0}{a_0})^{1.36}\right]\right\}\right)$$

In which, v is Poisson's ratio, E is Young's Modulus, ΔT is temperature change, h is the half fracture height, a_0 and b_0 are the semi axis of the cooled region, and β is the coefficient of thermal expansion.

3. 2-D Induced Stresses by Fracture Compression

1) Expressions from Jaeger and Cook

134
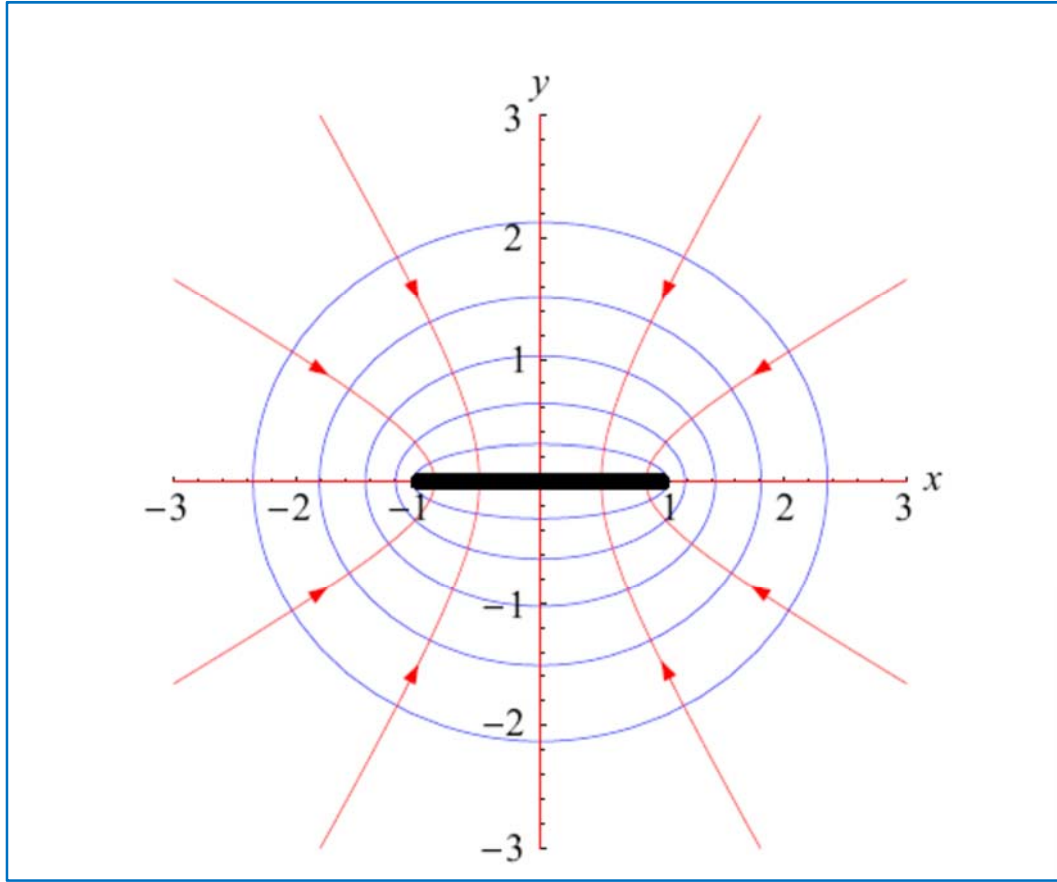
Fig.C.2 Elliptical Coordinate System.

As shown in Fig.C.2, considering the flat elliptic crack $\xi_0 = 0$, from J&C, for uniaxial

stress P$_2$ at infinity inclined at β to the plane of the crack:

$$\sigma_\xi + \sigma_\eta = P_2 \cos 2\beta + \alpha P_2[(1 - \cos 2\beta)\sinh 2\xi - \sin 2\beta \sin 2\eta] \qquad (C.34)$$

$$\begin{aligned}\sigma_\xi - \sigma_\eta &= \alpha P_2 \cos 2(\eta - \beta)\cosh 2\xi + \alpha^2 P_2 \{(1 - \cos 2\beta)\sinh 2\xi(\cos 2\eta - 1) \\ &- \cos 2\beta \cosh 2\xi + \cos 2(\eta - \beta) - \cosh 2\xi \sin 2\beta \sin 2\eta\}\end{aligned} \qquad (C.35)$$

$$\tau_{\xi\eta} = P_2 \frac{\alpha}{2} \sin 2(\beta - \eta) \sinh 2\xi$$
$$+0.5\alpha^2 P_2 \{\sinh 2\xi \sin 2\beta(\cos 2\eta - 1) \qquad \text{(C.36)}$$
$$+ \sin 2\eta(1 - \cos 2\beta)(\cosh 2\xi - 1)\}$$

In which

$$\alpha = (\cosh 2\xi - \cos 2\eta)^{-1} \qquad \text{(C.37)}$$

In order to check the equations we used in program, I firstly simplified the stresses on the axes Ox and Oy for the case $\beta = \frac{\pi}{2}$, and compared them with the plots in J&C: And the following plots shown are:
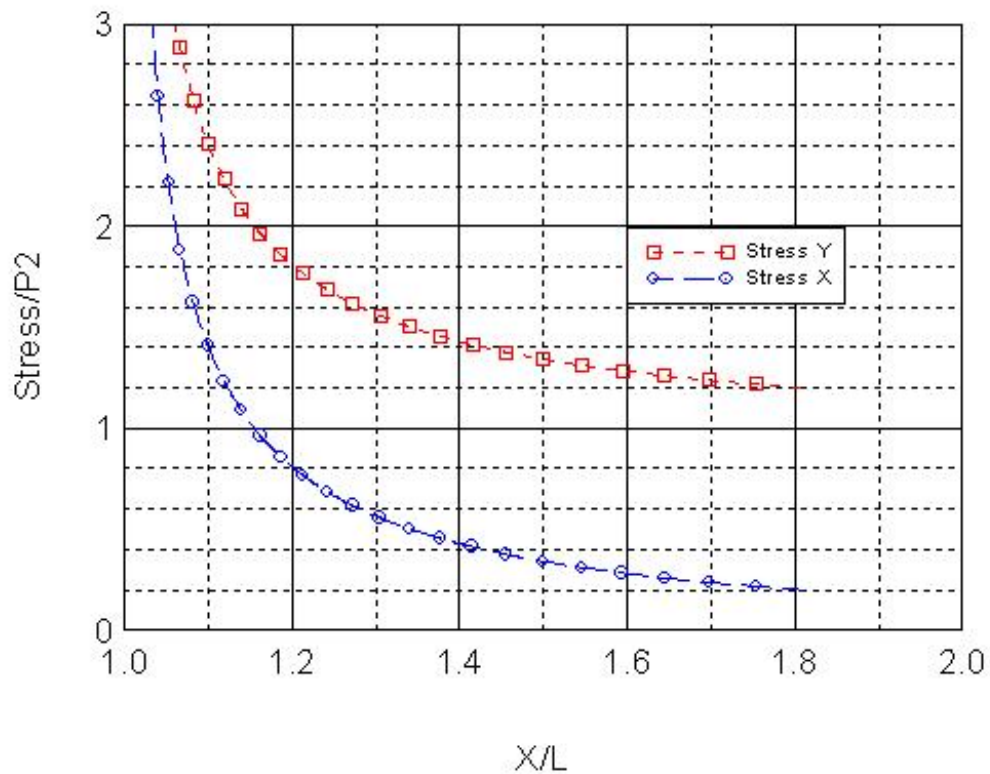
Fig.C.3 Stresses on the X-Axis.

136
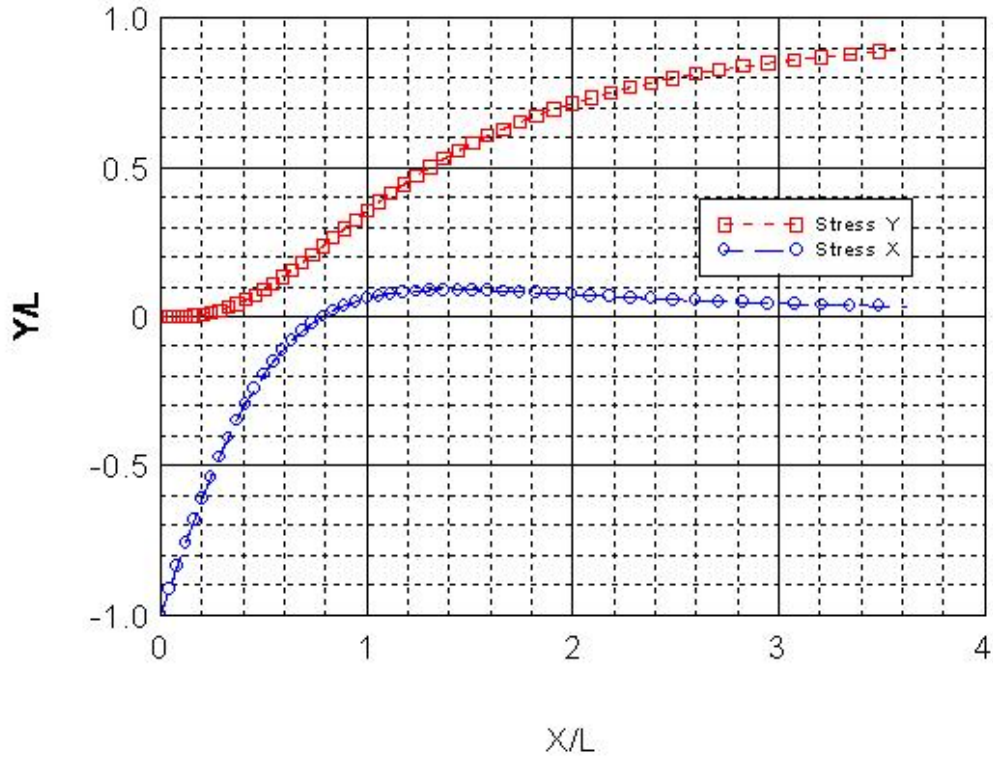
Fig.C.4 Stresses on the Y-Axis.

In the plots are shown the stresses σ_x and σ_y respectively, how could we get these

two values from σ_ξ and σ_η? We should use scale factors for the transform from

different coordinate systems. A transform factor we used in calculating the induced stress

by poro-thermo-elasticity for this is:

$$g = \sqrt{\frac{L^2}{2}(\cosh 2\xi - \cos 2\eta)} \qquad (C.38)$$

And:

$$\sigma_x = g^2 * \sigma_\xi; \quad \sigma_y = g^2\sigma_\eta; \quad \sigma_{xy} = g^2 * \sigma_{\xi\eta} \qquad (C.39)$$

137

However, in this problem, this factor is not right.

In fact, for the special directions: $\eta = 0$ and $\eta = \dfrac{\pi}{2}$; we get: $\sigma_{\xi\eta} = 0$

So, stresses on the a-axis are: $\sigma_x = \sigma_\xi$ and $\sigma_y = \sigma_\eta$

And, stresses on the b-axis are: $\sigma_x = \sigma_\eta$ and $\sigma_y = \sigma_\xi$

And this conclusion is right through comparing with the plots compared with what J&C got in their book (Fig.10.11.2, P268, 1979).

Then, the transformation factors in this problem are deduced in the following:

From J&C, we got the following equations:

$$\sigma_{\eta\eta} - \sigma_{\xi\xi} + 2i\sigma_{\xi\eta} = (\sigma_{yy} - \sigma_{xx} + 2i\sigma_{xy})e^{2i\theta} \tag{C.40}$$

$$\sigma_{\xi\xi} + \sigma_{\eta\eta} = \sigma_{yy} + \sigma_{xx} \tag{C.41}$$

Where

$$e^{2i\theta} = \cos 2\theta + i\sin 2\theta \tag{C.42}$$

$$\tan \theta = \frac{y}{x} = \frac{c\sinh\xi\sin\eta}{c\cosh\xi\cos\eta} \tag{C.43}$$

Subtract equation C.40 from C.41:

$$2(\sigma_{\xi\xi} - i\sigma_{\xi\eta}) = \sigma_{yy} + \sigma_{xx} - (\sigma_{yy} - \sigma_{xx} + 2i\sigma_{xy})e^{2i\theta} \tag{C.44}$$

So:

$$\begin{aligned}
2\sigma_{\xi\xi} - 2i\sigma_{\xi\eta} &= \sigma_{yy} + \sigma_{xx} - \sigma_{yy}\cos 2\theta + \sigma_{xx}\cos 2\theta \\
&\quad -(2i\sigma_{xy})(\cos 2\theta + i\sin 2\theta) \\
&\quad -(\sigma_{yy} - \sigma_{xx})(i\sin 2\theta)
\end{aligned} \tag{C.45}$$

$$\begin{aligned}
2\sigma_{\xi\xi} - 2i\sigma_{\xi\eta} &= \sigma_{yy} + \sigma_{xx} - \sigma_{yy}\cos 2\theta + \sigma_{xx}\cos 2\theta \\
&\quad +2\sigma_{xy}\sin 2\theta - 2i\sigma_{xy}\cos 2\theta - (\sigma_{yy} - \sigma_{xx})(i\sin 2\theta)
\end{aligned} \tag{C.46}$$

Therefore:

$$2\sigma_{\xi\xi} = (\sigma_{yy} + \sigma_{xx}) - (\sigma_{yy} - \sigma_{xx})\cos 2\theta + 2\sigma_{xy}\sin 2\theta \tag{C.47}$$

$$\begin{aligned}
-2i\sigma_{\eta\xi} &= -(\sigma_{yy} - \sigma_{xx})i\sin 2\theta - 2i\sigma_{xy}\cos 2\theta \\
or: \quad \sigma_{\eta\xi} &= \frac{1}{2}(\sigma_{yy} - \sigma_{xx})\sin 2\theta + \sigma_{xy}\cos 2\theta
\end{aligned} \tag{C.48}$$

We can also add C.40 to C.41, and get:

$$2\sigma_{\eta\eta} = (\sigma_{yy} + \sigma_{xx}) + (\sigma_{yy} - \sigma_{xx})\cos 2\theta - 2\sigma_{xy}\sin 2\theta \tag{C.49}$$

$$\sigma_{\eta\xi} = \frac{1}{2}(\sigma_{yy} - \sigma_{xx})\sin 2\theta + \sigma_{xy}\cos 2\theta \tag{C.50}$$

Then, equation C.49 times $\cos 2\theta$ and plus equation C.50 times $2\sin 2\theta$:

$$\sigma_{yy} - \sigma_{xx} = 2\sigma_{\eta\eta}\cos 2\theta + 2\sigma_{\xi\eta}\sin 2\theta - (\sigma_{\xi\xi} + \sigma_{\eta\eta})\cos 2\theta \qquad \text{(C.51)}$$

The same process, we can get:

$$\begin{aligned}\sigma_{yy} &= \sigma_{\eta\eta}\cos 2\theta + \sigma_{\xi\eta}\sin 2\theta + (\sigma_{\xi\xi} + \sigma_{\eta\eta})\sin^2\theta \\ &= \sigma_{\eta\eta} + \sigma_{\xi\eta}\sin 2\theta + (\sigma_{\xi\xi} - \sigma_{\eta\eta})\sin^2\theta\end{aligned} \qquad \text{(C.52)}$$

$$\sigma_{xx} = \sigma_{\xi\xi} - \sigma_{\xi\eta}\sin 2\theta - (\sigma_{\xi\xi} - \sigma_{\eta\eta})\sin^2\theta \qquad \text{(C.53)}$$

$$\sigma_{xy} = (\sigma_{\xi\eta} - \frac{1}{2}(\sigma_{yy} - \sigma_{xx})\sin 2\theta)/\cos 2\theta \qquad \text{(C.54)}$$

We can then get the expression for σ_{xy}.

2) Method from Pollard and Segall

Pollard and Segall (1989) have reported the general expressions for the stress field about the crack.

140
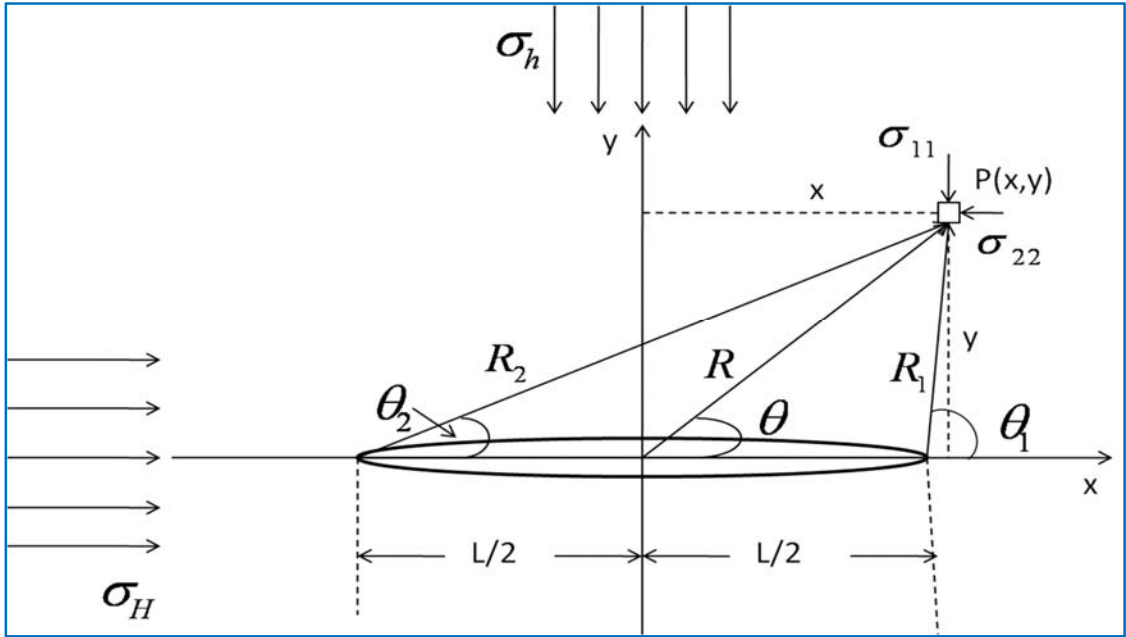
Fig.C.5 Stresses Changes due to Fracture Compression (Modified from Pollard and Segall, 1989).

In order to compare with the expressions in Warpinski, I used the same 2-D crack with the expressions from Pollard and Segall, and transformed them into x-y coordinates system:

$$\sigma_{xx} = \sigma_{22} + \Delta\sigma_I [Rr^{-1} * \cos(\theta - \Theta) - 1 - (L/2)^2 Rr^{-3} \sin\theta \sin 3\Theta]$$
$$+ \Delta\sigma_{II} [2Rr^{-1} * \sin(\theta - \Theta) - (L/2)^2 Rr^{-3} \sin\theta \cos 3\Theta] \tag{C.55}$$

$$\sigma_{yy} = \sigma_{11} + \Delta\sigma_I [Rr^{-1} * \cos(\theta - \Theta) - 1 + (L/2)^2 Rr^{-3} \sin\theta \sin 3\Theta]$$
$$+ \Delta\sigma_{II} [(L/2)^2 Rr^{-3} \sin\theta \cos 3\Theta] \tag{C.56}$$

$$\sigma_{xy} = \sigma_{12} + \Delta\sigma_{II} [Rr^{-1} * \cos(\theta - \Theta) - 1 - (L/2)^2 Rr^{-3} \sin\theta \sin 3\Theta]$$
$$+ \Delta\sigma_I [(L/2)^2 Rr^{-3} \sin\theta \cos 3\Theta] \tag{C.57}$$

In which σ_{11} is the remote stress normal to the crack, σ_{22} is the remote parallel stress, and σ_{12} is the remote shear stress. $[\Delta\sigma_I, \Delta\sigma_{II}] = [(\sigma_{11} - \sigma_{11}^c), (\sigma_{12} - \sigma_{12}^c)]$ in which σ_{11}^c

141

refers to the normal stress on the crack internal surface, and $\sigma_{12}{}^{c}$ refers to the shear stress

on the crack internal. L is the crack length, and the geometric relations are given by the

following equations: (as shown in the upper Fig. C.3)

$$R = \sqrt{x^2 + y^2}, \theta = \tan^{-1}(y/x) \tag{C.58}$$

$$R_1 = \sqrt{y^2 + (\frac{L}{2} - x)^2}, \quad \theta_1 = \tan^{-1}[y/(x - L/2)] \tag{C.59}$$

$$R_2 = \sqrt{y^2 + (x + L/2)^2}, \quad \theta_2 = \tan^{-1}[y/(x + L/2)] \tag{C.60}$$

$$r = (R_1 R_2)^{1/2} \quad \text{and} \quad \Theta = (\theta_1 + \theta_2)/2 \tag{C.61}$$

Negative values of θ, θ_1, and θ_2 should be replaced by $\pi + \theta$, $\pi + \theta_1$, and $\pi + \theta_2$

respectively, because these angles are in $(0, \pi)$.

APPENDIX D

FRACTURE PROPAGATION DIMENSIONS

The dimensions of the assumed regions around the hydraulic fracture were calculated based

on the previous work (Ge, 2009; Perkins and Gonzalez, 2985).

The bottom hole pressure is given by:

$$P_{iwf} = P_R + \Delta P_1 + \Delta P_2 + \Delta P_3 + \overline{\Delta P_f} \qquad \text{(D.1)}$$

In which:

$$\Delta P_1 = \frac{0.5 \times (\text{Ln}(K \times t/(\phi \times \mu \times c_t \times (0.5 \times r^2)) + 0.80907)}{1 - 0.5 \times (\text{Ln}(K \times t/(\phi \times \mu \times c_t \times (0.5 \times r^2)) + 0.80907)} (\Delta P_2) \qquad \text{(D.2)}$$

And

$$P_D(\xi, \eta, t_{DL}) = \frac{P_i - P(\xi, \eta, t)}{P_i - P_{wf}} \qquad \text{(D.3)}$$

And $P_D = 0.5 \times (\text{Ln}(K \times t/(\phi \times \mu \times c_t \times (0.5 \times r^2)) + 0.80907)$

In which P_i is the initial reservoir pressure, and P_{wf} is the pressure at the inner boundary,

as shown in the plan view of Fig.3.1: the inner boundary is the hot/cold boundary, and the

outer boundary is the water/oil boundary.

So, here

$$P_D(\xi, \eta, t_{DL}) = \frac{P_i - P(\xi, \eta, t)}{P_i - P_{wf}} = \frac{\Delta P_1}{\Delta P_1 + \Delta P_2} \tag{D.4}$$

then,

$$\Delta P_1 = \Delta P_2 \times P_D / (1 - P_D) = \frac{0.5 \times (\text{Ln}(K \times t / (\phi \times \mu \times c_t \times (0.5 \times r^2)) + 0.80907)}{1 - 0.5 \times (\text{Ln}(K \times t / (\phi \times \mu \times c_t \times (0.5 \times r^2)) + 0.80907)} (\Delta P_2) \tag{D.5}$$

In which C_t is the total compressibility. The most reasonable value of r appears to be a$_1$.

However, Kucuk and Brigham (1979.) did not mention a criterion for selection of r except

that it should be large enough; On the other hand, they also provided a different expression

for pressure that does not require r. namely:

$$P_{wD} = \frac{1}{2}(\ln t_{DL} + 2.19537) \tag{D.6}$$

In which

$$t_{DL} = \frac{3.6 * 10^{-6} k_o t}{\phi \mu c_t L^2} \tag{D.7}$$

$$\Delta P_1 = \frac{q\mu}{7.2 * 10^{-6} \pi k_o h} P_{wD} \tag{D.8}$$

As will be seen, the results from the previous Eqn. are closer to those of P&G.   This might

be because ΔP_1 in the latter equation is equal to the sum of ΔP_1, ΔP_2 and ΔP_3, so that the

accuracy is less than the separated calculation.

144

ΔP_2 and ΔP_3 are calculated from the following equations:

$$\Delta P_2 = i_w \mu_w \ln(\frac{a_1 + b_1}{a_0 + b_0}) / (2\pi k k_{rw} h) \qquad \text{(D.9)}$$

$$\Delta P_3 = i_w \mu_w \ln(\frac{a_0 + b_0}{L_f}) / (2\pi k k_{rw} h) \qquad \text{(D.10)}$$

$$\Delta \overline{P}_f = 0.00074 [\frac{i_w \mu_w L_f E^3}{(1 - \upsilon^2)^3 h^4}]^{1/4} \qquad \text{(D.11)}$$

Calculating the semi-axes of the cool region and flooded zone:

$$W_i = Qt \qquad \text{(D.12)}$$

$$V_{wt} = W_i / (\phi * (1 - S_{or} - S_{wi})) \qquad \text{(D.13)}$$

$$Vc = \frac{\rho_w C_w W_i}{\rho_{gr} C_{gr}(1 - \phi) + \rho_w C_w \phi(1 - S_{or}) + \rho_o C_o \phi S_o r} \qquad \text{(D.14)}$$

$$F1 = 2 * Vc / (\pi * h * L_f^2) + 0.5 * \sqrt{(\frac{4Vc}{\pi L_f^2 h})^2 + 4} \qquad \text{(D.15)}$$

$$F2 = 2 * V_{wt} / (\pi * h * L_f^2) + 0.5 * \sqrt{(\frac{4V_{wt}}{\pi L_f^2 h})^2 + 4} \qquad \text{(D.16)}$$

$$a_0 = L_f * (\sqrt{F1} + \frac{1}{\sqrt{F1}}) / 2 \qquad \text{(D.17)}$$

$$b_0 = L_f * (\sqrt{F1} - \frac{1}{\sqrt{F1}}) / 2 \qquad \text{(D.18)}$$

145

$$a_1 = L_f * (\sqrt{F2} + \frac{1}{\sqrt{F2}})/2 \tag{D.19}$$

$$b_1 = L_f * (\sqrt{F2} - \frac{1}{\sqrt{F2}})/2 \tag{D.20}$$

Calculating Fracture Length:

$$P_1 = \sigma_1 + \sqrt{\frac{\pi U E}{2(1-\upsilon^2)r_f}} \tag{D.21}$$

In which:

$$P_1 = P_{iwf} - 3\Delta P_f \tag{D.22}$$

$$\sigma_1 = (\sigma_H)_{min} + \Delta\sigma_{1T} + \Delta\sigma_{1P} \tag{D.23}$$

In which $\Delta\sigma_{1T}$ and $\Delta\sigma_{1P}$ are calculated from the following equations:

$$
\begin{aligned}
\frac{(1-v)\Delta\sigma_{1T}}{E\beta\Delta T} &= \frac{(b_0/a_0)}{1+(b_0/a_0)} + [\frac{1}{1+(b_0/a_0)}] \\
&\times (1/\{1+ \frac{1}{2}[1.45(\frac{h}{2b_0})^{0.9} + 0.35(\frac{h}{2b_0})^2] \\
&\times [1+(\frac{b_0}{a_0})^{0.774}]\})
\end{aligned} \tag{D.24}
$$

$$\frac{(1-\nu)\Delta\sigma_{1P}}{EJ\Delta P} = \frac{(b_0/a_0)}{1+(b_0/a_0)} + [\frac{1}{1+(b_0/a_0)}]$$

$$\times(1/\{1+[1.45(\frac{h}{2b_0})^{0.9}+0.35(\frac{h}{2b_0})^2]$$

$$\times[1+(1-\frac{b_0}{a_0})^{1.36}]\}) \qquad \text{(D.25)}$$

$$J = \frac{1-2\upsilon}{E} - \frac{c_{gr}}{3} \qquad \text{(D.26)}$$

The Bisection method for finding L_f is as the following:

Over some interval the function is known to pass through zero because it changes sign. Evaluate the function at the interval's midpoint and examine its sign. Use the midpoint to replace whichever limit that yields the same sign for F(x). After each iteration, the bounds containing the root decrease by a factor of two. If after n iterations the root is known to be within an interval of size ε_n, then after the next iteration it will be bracketed within an interval of size

$$\varepsilon_{n+1} = \varepsilon_n/2 \qquad \text{(D.27)}$$

Repeat the process until ε_n is less than a small number such as 1.0E-06. The corresponding value of x is the root of the function, i.e. the fracture length L_f.

For the problem at hand the function is $F(x)$ =LHS-RHS. To find the root, select L_f=X_1 which makes $F(x_1)$<0 while L_f=X_2 which makes $F(x_2)$>0. A root will be bracketed in the interval (X_1, X_2). In this study, the assumed data are X_1=0.6 and X_2=1.0E04.

147

REFERENCES

Abé, H., T. Mura, and Keer, L. 1976. Growth rate of a penny-shaped crack in hydraulic fracturing of rocks. *J. Geophys. Res. 81*, 5335–5340.

Atkinson, B.K.(editor): Fracture Mechanics of Rocks. *Academic Press*, 1989.

Barton N., 1976. The shear strength of rock and rock joints. *Int. J. Rock Mech. Min. Sci. & Geomech. Abstr.* v. 13, 255-279.

Biot, M.A., 1941. General Theory of Three-dimensional Consolidation. *Journal of Applied Physics*, vol. 12, pp. 155-164.

Brannon, H.D. and Starks, T.R. 2008. The Effects of Effective Fracture Area and Conductivity on Fracture Deliverability and Stimulation Value. *Paper presented at the SPE Annual Technical Conference and Exhibition*, Denver, Colorado, USA. Society of Petroleum Engineers 116057-MS.

Carslaw, S. H. and Jaeger, C. J. 1959. *Conduction of Heat in Solids*. Oxford University Press

Cheng, Y. 2009. Boundary Element Analysis of the Stress Distribution around Multiple Fractures: Implications for the Spacing of Perforation Clusters of Hydraulically Fractured Horizontal Wells. *Paper presented at the SPE Eastern Regional Meeting*, Charleston, West Virginia, USA. Society of Petroleum Engineers 125769-MS.

Cipolla, C.L., Warpinski, N.R., Mayerhofer, M.J. et al. 2008. The Relationship between Fracture Complexity, Reservoir Properties, and Fracture Treatment Design. *Paper presented at the SPE Annual Technical Conference and Exhibition*, Denver,

Colorado, USA.   Society of Petroleum Engineers 115.

Cipolla, C.L., Lolon, E., Erdle, J.C. et al. 2009. Reservoir Modeling in Shale-Gas Reservoirs. *Paper presented at the SPE Eastern Regional Meeting*, Charleston, West Virginia, USA.   Society of Petroleum Engineers 125530-MS.

Cipolla, C.L., Lolon, E., Erdle, J. et al. 2009. Modeling Well Performance in Shale-Gas Reservoirs. *Paper presented at the SPE/EAGE Reservoir Characterization and Simulation Conference*, Abu Dhabi, UAE.   Society of Petroleum Engineers 125532-MS.

Cleary, M. P., 1980, Comprehensive design formulae for hydraulic fracturing, SPE Paper No. 9259, *55th Annual Fall Technical Conference and Exhibition*, Dallas, 21–24 September.

Cramer, D.D. 2008. Stimulating Unconventional Reservoirs: Lessons Learned, Successful Practices, Areas for Improvement. *Paper presented at the SPE Unconventional Reservoirs Conference*, Keystone, Colorado, USA.   Society of Petroleum Engineers 114172.

Daneshy, A. A. On the Design of Vertical Hydraulic Fractures. *JPT* (January 1973) 83-93; T*rans.*, AIME, 255.

Detournay, E., Cheng, A. H. D., and Mclennan, J.D. 1990. A Poroelastic PKN Hydraulic Fracture Model Based on an Explicit Moving Mesh Algorithm. *J. Energy Res. Tech.Trans.* ASME 112 (4): 7.

Detournay, E. and Cheng, A. H. D. 1993. Fundamentals of Poroelasticity. *In Comprehensive Rock Engineering: Principles, Practice and Project*, ed. Fairhurst, C., Analysis and Design Method: Pergamon Press. II.

Economides, M.J. and K.G. Nolte. Reservoir stimulation, 3rd Edition, *John Wiley & Sons,LTD*, 2000.

Economides, M.J., Oligney, R.E., and Valkó, P.P. 2002. *Unified Fracture Design*. Houston: Orsa Press.

Franquet, J. A., et al., 2008. Critically-Stressed Fracture Analysis Contributes to Determining the Optimal Drilling Trajectory in Naturally Fractured Reservoirs. *International Petroleum Technology Conference.* Kuala Lumpur, Malaysia, 3-5 December 2008.

Gale, J. F. W., Reed, R. M., & Holder, J. (2007). Natural fractures in the Barnett Shale and their importance for hydraulic fracture treatments. *AAPG Bulletin, 91*(4), 603-622.

Gao, Q. and Ghassemi, A. 2017. Pore Pressure and Stress Distributions Around a Hydraulic Fracture in Heterogeneous Rock. *Rock Mechanics and Rock Engineering* 50 (12): 3157–3173.

Ge J., Ghassemi A. 2007. Pore Pressure and Stress Distributions around an Injection-Induced Fracture. *Geothermal Resources Council Transaction*, Vol. (31): 279-283.

Ge, J. and Ghassemi, A. 2008. Analysis of Failure Potential around a Hydraulic Fracture in Jointed Rock. Paper presented at *42th U.S. Rock Mechanics / Geomechanics Symposium*. San Francisco, California: American Rock Mechanics Association.

Ge, J., and Ghassemi, A. 2011. Permeability Enhancement in Shale Gas Reservoirs after Stimulation by Hydraulic Fracturing. Paper presented at *45th U.S. Rock Mechanics / Geomechanics Symposium*. San Francisco, California: American Rock Mechanics Association.

Ge J., Ghassemi A. 2012 Stimulated Reservoir Volume by Hydraulic Fracturing in Naturally Fractured Shale Gas Reservoirs**.** Paper presented at *46th U.S. Rock Mechanics / Geomechanics Symposium*, Chicago, Illinois: American Rock Mechanics Association.

Ge, J. and Ghassemi, A. 2014. Analytical Modeling on 3-D Stress Redistribution and Fault Reactivation During Hydraulic Fracturing Stimulation. *Paper presented at the 48th U.S. Rock Mechanics/Geomechanics Symposium,* Minneapolis, Minnesota. American Rock Mechanics Association.

Geertsma, J., 1957. The Effect of Fluid Pressure Decline on the Volumetric Changes of Porous Rocks. *Journal of Applied Mechanics*, vol. 24, pp. 594-601.

Geertsma, J. and de Klerk, F.A. 1969. Rapid Method of Predicting Width and Extent of Hydraulically Induced Fractures. *JPT* 21 (12): 1571-81. SPE-2458-PA DOI: 10.2118/2458-PA.

Ghassemi, A. 2017. 1 - Application of Rock Failure Simulation in Design Optimization of the Hydraulic Fracturing. *In Porous Rock Fracture Mechanics*: Woodhead Publishing. 3-23.

Ghassemi, A. and Roegiers, J.-C. (1996). A threedimensional poroelastic hydraulic fracture

simulator using the displacement discontinuity method, Proc. *2nd North American Rock Mech. Symposium*, Montreal, Ca, 1, 982-987

Ghassemi, A., Suresh Kumar, G. 2007. Variation of Fracture Aperture and Pressure Due to Combined Heat Extraction-Induced Thermal Stress and Silica Dissolution/Precipitation. *Geothermics*. 36, 115–140.

Ghassemi, A., Tarasovs, S., and Cheng, A. H.-D. 2007. A Three-Dimensional Study of the Effects of thermo-mechanical loads on fracture slip in enhanced geothermal reservoir. *Int. J. Rock Mechanics & Min Sci.*, Vol. 44 , pp. 1132–1148.

Ghassemi, A., Tarasovs, A. and Cheng, A.D.-H. 2005. Integral equation solution of heat extraction induced thermal stress in enhanced geothermal reservoirs. *Int. J. Num. & Anal. Methods in Geomechanics*, 29, 829-844.

Ghassemi, A. and Tao, Q. 2016. Thermo-Poroelastic Effects on Reservoir Seismicity and Permeability Change. *Geothermics* 63: 210-224.

Ghassemi, A., Zhang, Q. 2006. Poro-thermoelastic response of a stationary crack using the displacement discontinuity method. *ASCE J. Engineering Mechanics*, 132(1), 26-33.

Ghassemi, A., Zhou, X.X., and Rawal, C. 2010. 3d Poroelastic Analysis of Rock Failure around a Hydraulic Fracture. *Paper presented at the 44th U.S. Rock Mechanics Symposium and 5th U.S.-Canada Rock Mechanics Symposium*, Salt Lake City, Utah. American Rock Mechanics Association.

Gidley, J.L. 1989. *Recent advances in hydraulic fracturing*. United States.

Goodman, R.E. 1989. *Introduction to Rock Mechanics*. 2nd ed. Wiley.

Green, A.E. and Sneddon, I.N. 1950. The Distribution of Stress in the Neighborhood of a Flat Elliptic Crack in an Elastic Solid. *Proc. Camb. Phil. Soc*. (1950) 46, 159.

Jaeger J.C. and Cook N.G.W.: Fundamentals of Rock Mechanics. 1979.

Kassir, M.K. and Sih, G.C. 1966. Three-Dimensional Stress Distribution Around an Elliptical Crack Under Arbitrary Loadings, *Journal of Applied Mechanics*, (1966) September 601-611.

Koning, E.J.L. Fractured Water Injection Wells -Analytical Modeling of Fracture Propagation. Paper SPE 14684 presented at 1985.   SPE-14684 -MS DOI: 10.2118/14684 –MS.

Kurtoglu, B., *C.S.o.M.D.o.P. 2013*. Integrated Reservoir Characterization and Modeling in Support of Enhanced Oil Recovery for Bakken.

Legarth, B., Huenges, E., and Zimmermann, G. 2005. Hydraulic Fracturing in a Sedimentary geothermal Reservoir: Results and Implications. *International Journal of Rock Mechanics & Mining Sciences* 42(2005) 1028-1041.

Li, Y., Wang, Y., Cheng, X. et al. 2010. Case Study of Multistage Isolating Stimulation in High Temperature Deep Carbonate Horizontal Wells. *Paper presented at the SPE Oil and Gas India Conference and Exhibition*, Mumbai, India.   Society of Petroleum Engineers 125854-MS.

Maugis, D. Stresses and Displacements around Cracks and Elliptical Cavities: Exact Solutions. *Engineering Fracture Mechanics*, 1992.

Muskat, M.: The flow of homogeneous fluids through porous media, first edition, J.W. Edwards Inc., Ann Arbor, MI(1946).

Mayerhofer, M. J., E. Lolon, N. R. Warpinski, C. L. Cipolla, D. W. Walser, and C. M. Rightmire. 2010. What Is Stimulated Reservoir Volume? *SPE Production & Operations* (02).

Mildren, S.D., Hillis, R.R. & Kaldi, J. 2002. Calibrating predictions of fault seal reactivation in the Timor Sea. *Australian Petroleum Production and Exploration Association Journal*, 42, 187–202.

Mildren, S.D., Hillis, R.R. & Lyon, P.J. et al. 2002. FAST: A New Technique for Geomechanical Assessment of the Risk of Reactivation-related Breach of Fault Seals. *AAPG Hedberg Series*, No. 2, 73–85.

Nelson, E.J., et al., 2007. Using geological information to fracture optimize stimulation practices in the Cooper Basin, *Australia. Petroleum Geoscience*, Vol. 13. 2007, 3–16.

Murphy, H., 1983.Hot dry rock reservoir development and testing in the USA, *Mechanics of Elastic and Inelastic Solids 5, Hydraulic fracturing and geothermal energy*, edited by S. Namet-Nasser, H. Abé, and S. Hirakawa, Martinus Nijhoff Publishers, pp528.

Nordgren, R.P. 1972. Propagation of a Vertical Hydraulic Fracture. SPEJ 12 (8): 306-314; *Trans.*, AIME, 253, 1972.

Nygren, A. and Ghassemi, A. 2005. Poroelastic and Thermoelastic Effects of Injection into

a Geothermal Reservoir. *The 41st U.S. Symposium on Rock Mechanics*. June 17-21, 2006.

Palciauskas, V.V., and Domenico, P.A., 1982. Characterization of Drained and Undrained Response of Thermally Loaded Repository Rocks. *Water Resources Research*, vol.18, pp. 281-290.

Palisch, T.T., Vincent, M.C. and Handren, P.J., 2008. Slickwater Fracturing – Food for Thought. Paper SPE 115766 presented at the 2008 SPE Annual Technical Conference and Exhibition, Denver, Colorado, 21-24 September. SPE-10.2118/115766-MS DOI: 10.2118/115766-MS.

Palmer, I.D., Moschovidis, Z.A., and Cameron, J.R. 2005. Coal Failure and Consequences for Coalbed Methane Wells. Paper presented at *the SPE Annual Technical Conference and Exhibition*, Dallas, Texas. Society of Petroleum Engineers 96872-MS.

Palmer, I.D., 2007. Modeling Shear Failure and Stimulation of the Barnett Shale After Hydraulic Fracturing. 2007. Paper SPE 106113 presented at the 2007 SPE Hydraulic Fracturing Technology Conference held in College Station, Texas, U.S.A., 29–31 January 2007. SPE-10.2118/106113 -MS DOI: 10.2118/106113 – MS.

Palmer, I.D., Coalbed Methane Well Completions and Production: Field Data, Best Practices, New Aspects. 2007. Presymposium short course presented at the 2007 International Coalbed Methane Symposium, Tuscaloosa, Alabama, 22 May.

Perkins, T.K. and Kern, L.R., 1961. Width of Hydraulic Fractures. *JPT* 13 (9): 937-49; *Trans*., AIME 222.

Perkins, T.K., and Gonzalez, J.A., 1985. The Effect of Thermoelastic Stresses on Injection Well Fracturing, SPE 11332, 1985.

Pollard, D.D. and Segall, P., 1987, Theoretical displacement and stresses near fractures in rock: with applications to faults, joints, veins, dikes, and solution surfaces. In B.K. Atkinson, ed., Fracture Mechanics of Rock, Academic Press, Inc., pp. 277-349.

Rahman, M.M., Rahman, M.K., and Rahman, S.S., 2002. An Analytical Model for Production Estimation From Hydraulically Fractured Tight-Gas Reservoirs. 2002. Paper SPE 77901 presented at the 2002 SPE Asia Pacific Oil and Gas Conference and Exhibition, Melbourne, Australia, 8-10 October. SPE-77901-MS DOI: 10.2118/77901-MS.

Rebbins, R.E., Chen, S., and Lemp S.P. Design Consideration for Fracturing Job Sizing of Low-Permeability Gas Reservoirs of the Arkoma Basin. 1991. Paper SPE 21718 presented at the 1991 SPE Production Operations Symposium, Oklahoma City, Oklahoma, 7-9 April. 10.2118/21718-MS.

Rice, J.R., and Cleary, M.P., 1976. Some Basic Stress-diffusion Solutions for fluid Saturated Elastic Media with Compressible Constituents. *Reviews of Geophysics and Space Physics*, vol.14, pp. 227-241.

Safari, R. and Ghassemi, A. 2014. 3d Coupled Poroelastic Analysis of Multiple Hydraulic Fractures. *Paper presented at the 48th U.S. Rock Mechanics/Geomechanics*

Symposium, Minneapolis, Minnesota.   American Rock Mechanics Association.

Settari, A., 1980. Simulation of Hydraulic Fracturing Processes. Paper SPE 7693, presented at the 4th Numerical *Simulation*. Symposium of SPE, Denver, Colorado, December, 1980: 487-500.

Shin, K., K. Sugawara and S. Okubo, Application of Weibull's theory to estimating in situ maximum stress σ_H by hydrofracturing, *International Journal of Rock Mechanics & Mining Sciences*, 38, 423-420, 2001.

Sih, G.C. and Liebowitz, H. 1968. *Mathematical Theories of Brittle Fracture*, in *Fracture*, H. Liebowitz (ed.), Vol. II, Academic Press, New York City (1968) 137.

Sneddon, I. N., "The Distribution of Stress in the Neighborhood of a Crack in an Elastic Solid," Proceedings of the Royal Society, London, Series A, Vol. 187, 1946.

Sneddon, I. N., Lowengrub, M., 1969. *Crack Problems in the Classical Theory of Elasticity* John Wiley & Sons, Inc., New York,.

Tao, Q., Ghassemi, A., and Ehlig-Economides, C.A. 2011. A Fully Coupled Method to Model Fracture Permeability Change in Naturally Fractured Reservoirs. *International Journal of Rock Mechanics and Mining Sciences* 48 (2): 259-268.

Timoshenko, S., and Goodier, J.N., *Theory of Elasticity*, 2nd edition, McGraw-Hill, New York, 1951., 506p.

Valko, P. and Economides, M. 1995. *Hydraulic Fracture Mechanics*. Chichester UK: JohnWiley & Sons.

Vandamme, L., Detournay, E., and Cheng, A.H.-D., 1989. A Two-dimensional Poroelastic

Displacement Discontinuity Method for Hydraulic Fracture Simulation. *International Journal for Numerical and Analytical Methods in Geomechanics*, vol. 13, pp. 215-224.

Veatch, R.W., 1983. Overview of current hydraulic fracturing design and treatment technology- part 1, *Journal of Petroleum Technology*, 677-687, April 1983a.

Veatch, R.W., 1983. Overview of current hydraulic fracturing design and treatment technology- part 2, *Journal of Petroleum Technology*, 853-863, April 1983b.

Verde, A. and Ghassemi, A. 2015. Fast Multipole Displacement Discontinuity Method (Fm-Ddm) for Geomechanics Reservoir Simulations. *International Journal for Numerical and Analytical Methods in Geomechanics* 39 (18): 1953-1974.

Warpinski, N.R. and Branagan, P.T. 1989. *Altered-Stress Fracturing*. JPT 1989.

Warpinski, N.R., Mayerhofer, M.J., Vincent, M.C. et al. 2008. Stimulating Unconventional Reservoirs: Maximizing Network Growth While Optimizing Fracture Conductivity. *Paper presented at the SPE Unconventional Reservoirs Conference*, Keystone, Colorado, USA.   Society of Petroleum Engineers 11.

Warpinski, N.R., Sullivan, R.B., Uhl, J. et al. 2005. Improved Microseismic Fracture Mapping Using Perforation Timing Measurements for Velocity Calibration. *SPE Journal* 10 (1): pp. 14-23. 84488-PA

Warpinski, N.R. and Teufel, L.W. 1987. Influence of Geologic Discontinuities on Hydraulic Fracture Propagation (Includes Associated Papers 17011 and 17074). *SPE Journal of Petroleum Technology* 39 (2): 209-220. 13224-PA

Warpinski, N.R., Wolhart, S.L., and Wright, C.A. 2004. Analysis and Prediction of Microseismicity Induced by Hydraulic Fracturing. *SPE Journal* 9 (1): 24-33. 87673-PA

Xue, W. and Ghassemi, A. 2009. Poroelastic Analysis of Hydraulic Fracture Propagation. *Paper presented at the 43rd U.S. Rock Mechanics Symposium & 4th U.S. - Canada Rock Mechanics Symposium*, Asheville, North Carolina. American Rock Mechanics Association.

Yew, C.H., Mechanics of Hydraulic Fracturing, Gulf Publishing Company, Houston, Texas, 1997.

Zhang, Z., Li, X., He, J. et al. 2017. Numerical Study on the Propagation of Tensile and Shear Fracture Network in Naturally Fractured Shale Reservoirs. *Journal of Natural Gas Science and Engineering* 37: 1-14.

Zheltov, Y.P. and Khristianovitch, S.A. 1955. Hydraulic Fracture of an Oil-Bearing Bed. *Izvest. Akad. Nauk SSR, OTN* 5: 3-41.

NOMENCLATURE

a_0 and b_0 = major and and minor axis of water flood ellipse (L)

a and b = fracture half length and half height (L)

a1 and b1 = major and minor axis of water flood ellipse (L)

a_R and b_R = major and minor axis of the elliptical zone extending to the far-field (L)

A = drainage area (L^2) / fracture stress constant (L^3)

c = cohesion (psi)

C_f = formation compressibility

C_t = system compressibility at initial reservoir conditions,

D = formation depth, (L)

d_H, d_h, and d_v = direction cosines for a given plane to the direction of the three stresses

σ_H , σ_h and σ_v

E = Young's modulus

E( ) = is the complete elliptic integral of the second kind

G = shear modulus of rock formation

G_f = fluid pressure gradient

h_f = fracture height, (L)

H = pay zone thickness, (L)

H_f = half fracture height, (L)

i = time-step interval

$i_{pf} =$ the injection rate per zone

$J =$ linear coefficient of pore pressure expansion

$k =$ modulus

$k_{rw} =$ water relative permeability, (L^2)

$k_{ro} =$ oil relative permeability, (L^2)

$k_{rg} =$ gas relative permeability, (L^2)

$K =$ formation permeability, (L^2)

$k/\mu =$ permeability/viscosity ratio

$K =$ cohesion modulus

$K_c =$ critical stress-intensity factor

$L =$ length, (L)

$l, m,$ and $n =$ direction cosines for a given plane to the direction of the principal stresses

$L_f =$ optimal fracture half-length, (L)

$L_{(t)} =$ fracture half-length at time t, (L)

$p =$ pressure

$p_0 =$ pressure at the wellbore

$p_{ave} =$ reservoir average pressure

$p_f =$ fracture pressure (psi)

$p_f =$ fracture pressure

$p_i =$ initial pressure

$p(0,t) =$ pressure at the wellbore at time t

$p(X,t)$ =pressure at coordinate X at time t

Δp =pressure drop

Δp_1= difference in pressure between water flood and far-field boundaries

Δp_2= difference in pressure between cool front and water flood front

Δp_3= difference in pressure between fracture surface and cool front

Δp_f= difference in pressure between fracture surface and cool front

q =fracturing fluid flow rate

q_0 =injection rate

$q(0,t)$ =injection rate at the wellbore (x=0)   at time t

r_e =reservoir drainage radius, (L)

r_w =wellbore radius, (L)

S_w =water saturation

S_{wi} =initial water saturation

t =time point during a fracture treatment

T_f =fracture temperature, ºF

T_{pc} =pseudocritical fracture temperature, ºF

T_{pr} =reduced temperature, ºF

$T =$ temperature (ºF)

$\Delta T =$ temperature difference (ºF)

V =volume, ft^3

V_p =volume of proppant in pay, ft^3

V_{pf} =volume of propped fracture, ft^3

V_r =reservoir drainage volume, ft^3

w =fracture width, ft

$W_{(x,t)}$ =width in elliptical fracture at time t at location X, ft

X =coordinate along direction of fracture propagation

$\Delta\sigma$ =in-situ stress differential between the potential barrier and the payzone, psi

μ = viscosity, cp / ellipsoidal coordinate

μ_g = gas viscosity, cp

μ_o = oil viscosity, cp

μ_w = water viscosity, cp

μ_{cold} = water viscosity at low temperature, cp

μ_{hot} = water viscosity at high temperature, cp

ν =Poisson's ratio

ρ =density of the fracturing fluid

σ_h = in-situ horizontal rock stress perpendicular to fracture face (psi)

σ_H = in-situ horizontal rock stress parallel to fracture face (psi)

σ_V = in-situ vertical rock stress (psi)

σ_n = normal stress perpendicular to a face (psi)

$\sigma_1, \sigma_2, \sigma_3$ = principal stresses (psi)

τ = the shear stress (psi)

τ_s = the shear strength or cohesive strength (psi)

163

Φ = potential function

ϕ = porosity, %

φ' = friction angle

δ = the dip angle

φ = the dip direction angle

ξ, η = elliptical coordinates

ξ_i (i from 0 to 2) = elliptical coordinate at different zones

ζ = leakoff factor

$\lambda, \mu, \varepsilon$ = ellipsoidal coordinates

snu cnu and dnu = Jacobian elliptic functions as inverses of the incomplete elliptic integral

of the first kind